Decadal Trends in the Oceanic Storage of Anthropogenic Carbon from 1994 to 2014

Jens Daniel Müller[1], Nicolas Gruber[1], Brendan R. Carter[2], Richard A. Feely[3], Masao Ishii[4], Nico Lange[5], Siv K Lauvset[6], Akihiko M. Murata[7], Are Olsen[8], Fiz F. Pérez[9], Christopher L. Sabine[10], Toste Tanhua[11], Rik Wanninkhof[12], and Donghe Zhu[1]

[1]ETH Zürich
[2]University of Washington
[3]Pacific Marine Environmental Laboratory (NOAA)
[4]Meteorological Research Institute
[5]14GEOMAR Helmholtz Centre for Ocean Research Kiel
[6]NORCE Norwegian Research Centre
[7]Japan Agency for Marine-Earth Science and Technology
[8]Geophysical Institute
[9]Instituto de Investigaciones Marinas (CSIC)
[10]University of Hawaii Manoa
[11]GEOMAR Helmholz Centre for Ocean Research
[12]OCD/AOML/NOAA

February 1, 2023

Abstract

The oceanic storage of anthropogenic CO_2 (C_{ant}) that humans have emitted into the atmosphere has been pivotal for counteracting climate change. Yet multi-decadal trends in the ocean interior storage of C_{ant} have not been assessed at global scale. Here, we determine storage changes of C_{ant} by applying the eMLR(C*) regression method to ocean interior observations collected between 1989 and 2020. We find that the global ocean storage of C_{ant} grew by 29 ± 3 Pg C dec^{-1} and 27 ± 3 Pg C dec^{-1} ($\pm 1\sigma$) from 1994 to 2004 and 2004 to 2014, respectively. Although the two growth rates are not significantly different, they imply a reduction of the oceanic uptake fraction of the anthropogenic emissions from 36 ± 4 % to 27 ± 3 % from the first to the second decade. We attribute this reduction to a decrease of the ocean buffer capacity and changes in ocean circulation. In the Atlantic Ocean, the maximum storage rate shifted from the Northern to the Southern Hemisphere, plausibly caused by a weaker formation rate of North Atlantic Deep Waters and an intensified ventilation of mode and intermediate waters in the Southern Hemisphere. Between 1994 and 2004, the oceanic C_{ant} accumulation exceeded the net air-sea flux by 8 ± 4 Pg C dec^{-1}, suggesting a loss of natural carbon from the ocean during this decade. Our results reveal a substantial sensitivity of the ocean carbon sink to climate variability and change.

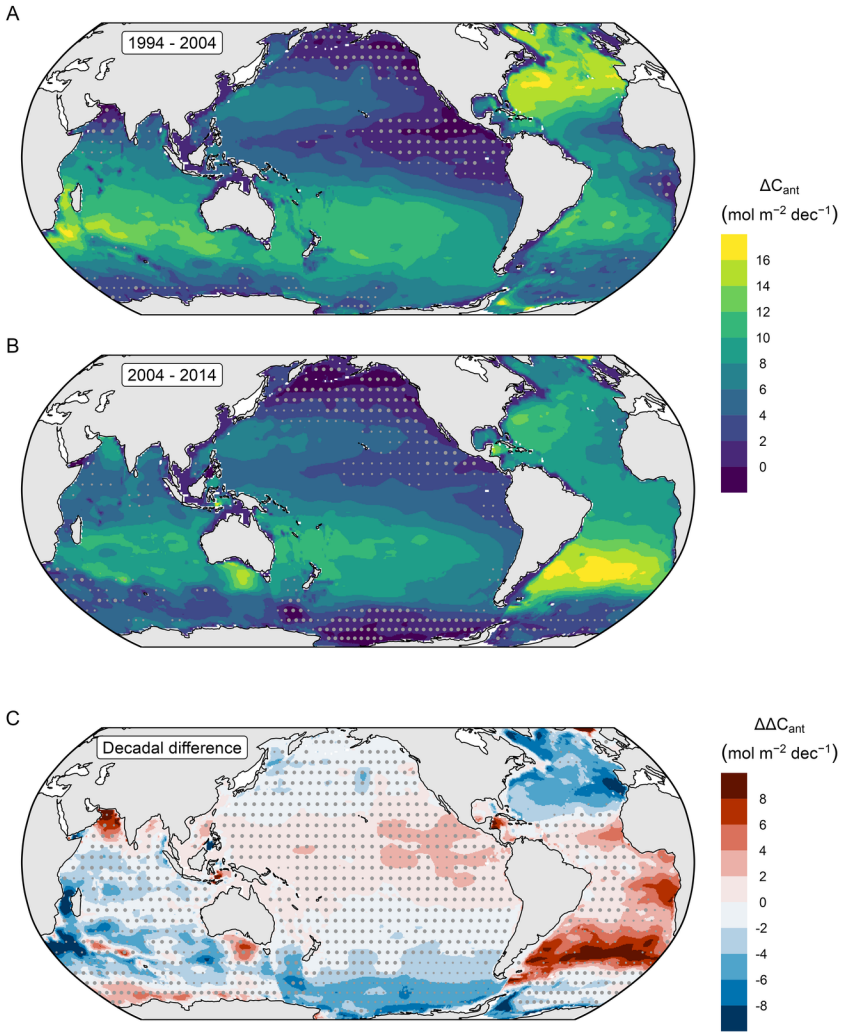

Decadal Trends in the Oceanic Storage of Anthropogenic Carbon from 1994 to 2014

Jens Daniel Müller[1] (0000-0003-3137-0883), N. Gruber[1] (0000-0002-2085-2310), B. Carter[2,3] (0000-0003-2445-0711), R. Feely[3] (0000-0003-3245-3568), M. Ishii[4] (0000-0002-7328-4599), N. Lange[5], S.K. Lauvset[6] (0000-0001-8498-4067), A. Murata[7] (0000-0002-5931-2784), A. Olsen[8] (0000-0003-1696-9142), F.F. Pérez[9,10] (0000-0003-4836-8974), C. Sabine[12] (0000-0001-6945-8552), T. Tanhua[5] 0000-0002-0313-2557, R. Wanninkhof[13] (0000-0003-1973-3514), D. Zhu[1] (0000-0002-6033-9079)

[1]Environmental Physics, Institute of Biogeochemistry and Pollutant Dynamics, ETH Zurich, Zurich, Switzerland.

[2]Cooperative Institute for Climate, Ocean, and Ecosystem Studies, University of Washington, Seattle, WA, 98105.

[3]Pacific Marine Environmental Laboratory, National Oceanic and Atmospheric Administration, Seattle, WA, 98115.

[4]Meteorological Research Institute, Japan Meteorological Agency, Tsukuba, Japan.

[5]GEOMAR Helmholtz Centre for Ocean Research Kiel, Kiel, Germany.

[6]NORCE Norwegian Research Centre, Bjerknes Centre for Climate Research, Bergen, Norway.

[7]Japan Agency for Marine-Earth Science and Technology, Yokosuka, Kanagawa, 237-0061, Japan.

[8]Geophysical Institute, University of Bergen and Bjerknes Centre for Climate Research, Bergen, Norway.

[9]Instituto de Investigaciones Marinas (IIM), CSIC, Vigo, Spain.

[10]Oceans Department, Stanford University, Stanford, CA 94305, USA.

[12]University of Hawaii at Manoa, Honolulu, HI, 96822.

[13]Atlantic Oceanographic and Meteorological Laboratory, National Oceanographic and Atmospheric Administration, Miami, USA.

[2,3,13]authors with this affiliation are provisionally included on this submission until pending routine institutional review is completed

Corresponding author: Jens Daniel Müller (jensdaniel.mueller@usys.ethz.ch)

Key Points:

- The global ocean storage of anthropogenic carbon grew by 29 ± 3 and 27 ± 3 Pg C dec^{-1} from 1994 to 2004 and 2004 to 2014, respectively
- The fraction of anthropogenic emissions taken up by the ocean decreased from 36 ± 4 to 27 ± 3 % from the first to the second decade
- This reduction is attributed to a decrease of the ocean buffer capacity and changes in ocean circulation

Abstract

The oceanic storage of anthropogenic CO_2 (C_{ant}) that humans have emitted into the atmosphere has been pivotal for counteracting climate change. Yet multi-decadal trends in the ocean interior storage of C_{ant} have not been assessed at global scale. Here, we determine storage changes of C_{ant} by applying the eMLR(C*) regression method to ocean interior observations collected between 1989 and 2020. We find that the global ocean storage of C_{ant} grew by 29 ± 3 Pg C dec^{-1} and 27 ± 3 Pg C dec^{-1} (±1σ) from 1994 to 2004 and 2004 to 2014, respectively. Although the two growth rates are not significantly different, they imply a reduction of the oceanic uptake fraction of the anthropogenic emissions from 36 ± 4 % to 27 ± 3 % from the first to the second decade. We attribute this reduction to a decrease of the ocean buffer capacity and changes in ocean circulation. In the Atlantic Ocean, the maximum storage rate shifted from the Northern to the Southern Hemisphere, plausibly caused by a weaker formation rate of North Atlantic Deep Waters and an intensified ventilation of mode and intermediate waters in the Southern Hemisphere. Between 1994 and 2004, the oceanic C_{ant} accumulation exceeded the net air-sea flux by 8 ± 4 Pg C dec^{-1}, suggesting a loss of natural carbon from the ocean during this decade. Our results reveal a substantial sensitivity of the ocean carbon sink to climate variability and change.

Plain language summary

The ocean takes up about 30% of the CO_2 that is emitted to the atmosphere by human (anthropogenic) activities. The removal of this anthropogenic CO_2 from the atmosphere counteracts climate change. The rate at which the ocean takes up anthropogenic CO_2 is controlled by its transport from the surface to the depth of the ocean, where most of it accumulates. Thus, we can quantify and understand the oceanic uptake by keeping track of the accumulation of anthropogenic CO_2 in the ocean interior. In this study, we use a global

collection of measurements of CO_2 in seawater to infer the temporal evolution of this accumulation between 1994 and 2014. We find that the ocean continued to act as a strong sink for CO_2 over this period. However, the sink efficiency, which is the uptake per anthropogenic emissions of CO_2, decreased from the first (1994-2004) to the second decade (2004-2014) of our study. Our findings suggest that the ocean sink for CO_2 might further reduce as climate change progresses.

1 Introduction

As a consequence of climate change, the ocean is warming, acidifying, becoming more stratified, and experiencing increasing winds and an intensified hydrological cycle (Cheng et al., 2022; Jiang et al., 2019; Li et al., 2020; Young and Ribal, 2019; IPCC, 2019). While the ocean itself has been vital to mitigate climate change over the past two centuries through its removal of CO_2 from the atmosphere (Gruber et al., in press), a key concern is whether the ocean carbon sink will maintain its function in a changing climate. Models and observation-based estimates agree that since the beginning of the industrial period, the ocean has taken up roughly 30% of the total human CO_2 emissions due to fossil fuel combustion, cement production, and land use change (Friedlingstein et al., 2022; Sabine et al., 2004; Gruber et al., 2019; Khatiwala et al., 2013, 2009). The observations from the first global survey of CO_2 in the ocean interior during the 1980s and 1990s (Wallace, 1995; Key et al., 2004) provided an important pillar for this consensus, demonstrating that between ~1800 and 1994, the ocean had taken up 118 ± 19 petagrams (10^{15}g) of anthropogenic carbon from the atmosphere (Sabine et al., 2004). Anthropogenic carbon (C_{ant}) refers to the additional inorganic carbon present in the ocean-atmosphere system due to human CO_2 emissions to the atmosphere (Gruber et al., in press). We denote temporal changes in the ocean interior content of C_{ant} as ΔC_{ant}.

Another pillar supporting the consensus about the strength of the oceanic C_{ant} sink was established when the observational data were extended with the ocean interior measurements gathered during the second cycle of the repeat hydrography program in the framework of GO-SHIP, the Global Ocean Ship-based Hydrographic Investigations Program (Talley et al., 2016). Applying a modified version of the extended Multiple Linear Regression method (eMLR(C*)) to the data available until the early 2010s, Gruber et al. (2019) demonstrated that the ocean took up an additional 34 ± 4 Pg C of C_{ant} from 1994 to 2007 corresponding to a mean decadal storage rate of 26 ± 3 Pg C dec^{-1}. This globally integrated storage rate is indistinguishable from the growth that one would predict from the total C_{ant} storage in 1994 and assuming an increase of this inventory proportional with the rise in atmospheric CO_2. Hence, this finding suggested that up to 2007, the globally integrated oceanic C_{ant} sink had been responding in near steady-state fashion to the anthropogenic perturbation, without showing any discernible impact of climate change.

However, a first indication of a deviation from this proportional steady-state accumulation emerged in the spatial patterns of the reconstructed changes in C_{ant} storage between 1994 and 2007 (Gruber et al., 2019). By comparing these changes with those expected on the basis of the reconstructed storage of C_{ant} for 1994 (Sabine et al., 2004), Gruber et al (2019) found a roughly 20% decrease of the storage rate in the North Atlantic compensated by an increased storage rate in the South Atlantic. However, the robustness of these shifts remains unclear, because they were derived from the comparison of results from two different methodological approaches, both with poorly characterised uncertainties at the regional scale.

A second indication of a deviation from the proportional steady-state uptake emerged from the analysis of the difference between the ocean interior storage changes of C_{ant} and the net air-sea fluxes of CO_2 determined based on sea surface observations of pCO_2 (Landschützer et al., 2016). These surface flux estimates include the transfer of both anthropogenic CO_2 and natural CO_2 across the air-sea interface, with the latter referring to the carbon that was already present in the Earth System in preindustrial times (Gruber et al., in press). The difference between storage and net fluxes amounted to 5 ± 3 Pg C over the 1994–2007 period and was interpreted as a non-steady state (i.e., climate-driven) outgassing of natural CO_2 from the ocean.

While some studies suggested that the outgassing of natural CO_2 may contribute to a long-term saturation of the oceanic carbon sink (Le Quéré et al., 2007), recent surface flux estimates actually suggest that the net global ocean carbon sink increased strongly over the past decade (Friedlingstein et al., 2022; Fay et al., 2021). But for reasons not yet fully understood, Global Ocean Biogeochemical Models (GOBMs) tend to suggest a smaller increase in uptake since around 2002 compared to the estimates based on the surface ocean pCO_2 observations (Hauck et al., 2019, Friedlingstein et al., 2022). Hence, the discrepancy between these two methods increased over the 2010s, culminating in the surface flux products estimating a 0.6 Pg C yr^{-1} stronger sink than the GOBMs for the 2010s (Friedlingstein et al., 2022). This discrepancy forces the authors of the Global Carbon Budget (GCB) to assign only a medium confidence level to the ocean sink estimate, as it represents the mean of these models and surface flux products (Friedlingstein et al., 2022). Thus, independent information about the oceanic uptake of CO_2 by extending the knowledge about the oceanic accumulation of C_{ant} beyond 2007 would be very useful to help resolving this

discrepancy and to better understand the drivers for the changes in the strength of the ocean carbon sink.

Some independent information about the evolution of the ocean sink beyond 2007 is already available from regional analyses of the accumulation of C_{ant} over the last few decades. In the Pacific Ocean the C_{ant} inventory change was found to have increased from 8.8 ± 1.1 Pg C dec^{-1} between 1995 and 2005 to 11.7 ± 1.1 Pg C dec^{-1} between 2005 and 2015 (Carter et al., 2019). Even more pronounced increases were reported for the North Atlantic Ocean with an intensification of the C_{ant} storage from 1.9 ± 0.4 Pg C dec^{-1} for the 1989–2003 period to 4.4 ± 0.9 Pg C dec^{-1} from 2003 to 2014 (Woosley et al., 2016; Wanninkhof et al., 2010). While Woosley et al. (2016) reported a rather steady uptake behaviour in the South Atlantic, Gao et al. (2022) found that the rates of C_{ant} storage accelerated from the 1990s to the 2000s. In all regional studies, the temporal variability of the C_{ant} storage was attributed to changing ventilation patterns of the upper ocean. However, differences in time periods and statistical methods applied in the regional studies limit their synoptic assessment and prevent combining them into a global reconstruction of the oceanic increase in C_{ant} storage since 2007.

Such an extension of the reconstruction of the global increase in C_{ant} storage beyond 2007 is the key aim of this study. Our work profits from including ~100,000 additional observations of dissolved inorganic carbon (DIC) and related biogeochemical variables collected over the 2010s, which were compiled, quality-controlled, and made available by GLODAP, the Global Ocean Data Analysis Project (Lauvset et al., 2021). By consistently determining the storage increase between 1994 and 2004, and between 2004 and 2014, and benefitting from the reconstructed storage of C_{ant} for 1994, we can investigate for the first time the temporal evolution of the global increase in the oceanic storage of C_{ant}. This permits us to address whether the ocean has maintained its vital sink function in a changing climate. Our global-scale reconstruction of the oceanic storage of C_{ant} further serves as an important independent reference point for the ocean carbon sink estimates established by other means, especially in the context of the GCB (Friedlingstein et al., 2022) and the Intergovernmental Panel on Climate Change (IPCC) (Canadell et al., 2021).

2 Material and Methods

2.1 Overview of the Approach

Our global-scale analysis of the changes in the content of C_{ant} (ΔC_{ant}) is based on measurements of the dissolved inorganic carbon (DIC) content and related hydrographical and biogeochemical properties gathered from 1989–2020 and synthesised in the data product GLODAPv2.2021 (Olsen et al., 2016; Lauvset et al., 2021). This data product includes high-quality measurements from reoccupied sections for the purposes of diagnosing long term climate signals such as the accumulation of C_{ant}. The majority of the data used in this study stem from the JGOFS/WOCE global CO_2 survey conducted in the 1980s and 1990s (Wallace, 1995; Key et al., 2004), the repeat hydrography program GO-SHIP that began in 2003 and is now completing its second cycle (Talley et al., 2016; Sloyan et al., 2019), as well as a number of additional programs, including INDIGO, SAVE, TTO, JOIS, and GEOSECS (Key et al., 2004, and references therein). In addition to DIC, our analysis requires observations of salinity (S), temperature (T), total alkalinity (TA), oxygen (O_2), the apparent oxygen utilisation (AOU), silicate ($Si(OH)_4$), nitrate (NO_3^-), and phosphate (PO_4^{3-}). To extract the ΔC_{ant} signal from these data, we use the eMLR(C*) method (Gruber et al., 2019; Clement and Gruber, 2018) with a few modifications (see details below and in supplement S2).

Our application of the eMLR(C*) method employs the following steps:

1. The semi-conservative tracer C* (Gruber et al., 1996) is calculated from DIC as $C^* = DIC - 117\times[PO_4^{3-}] - 0.5\times(TA + 16\times[PO_4^{3-}])$.
2. The observations are clustered in neutral density slabs and ocean regions (Fig. S1), and assigned to one of the three sampling periods 1989–1999, 2000–2009, or 2010–2020 (Fig. 1).
3. Within each sampling period, the observed C* is adjusted to the respective reference year (t_{ref}) 1994, 2004, or 2014 assuming a transient steady state increase of C_{ant} (Gammon et al., 1982).
4. Within each neutral density slab and ocean region, a set of multiple linear regression (MLR) models are fitted with $C^*(t_{ref})$ as target variable and all possible combinations of at least 2 out of the 7 considered predictor variables S, T, O_2, AOU, $Si(OH)_4$, NO_3^-, PO_4^{3-}.
5. The 10 best common MLR models for two compared sampling periods are selected

within each density slab and ocean region based on the summed root mean squared error (RMSE), after excluding MLRs with strong multicollinearity between the predictors (see supplement S2.2).

6. The decadal change in anthropogenic carbon is computed as the difference between the average C* distribution for each sampling period, i.e. $\Delta C_{ant} = C^*(t_{ref,n+1},) - C^*(t_{ref,n})$, where the C* distributions are predicted ("mapped") for each t_{ref} by applying the selected MLRs to a common set of predictor climatologies.
7. In surface waters, ΔC_{ant} is predicted based on an transient equilibrium approach (McNeil et al., 2003), which assumes that the increase of the surface ocean pCO_2 follows that of the atmosphere closely. This approach aims to avoid biases introduced by the seasonal and interannual variability of C* and the predictor variables.

The most important differences we introduced relative to the methods described by Clement and Gruber (2018) and Gruber et al. (2019) are detailed in section 2.3 and include a more thorough selection of the predictor variables and MLR models, a more robust and standardised quantification of uncertainties, and an assessment of structural reconstruction uncertainties through tests with synthetic data, which were performed in parallel to the analysis of the real-world observations. Our reconstruction of ΔC_{ant} with the eMLR(C*) method involves a number of choices regarding the configuration of the method. In sections 2.2 and 2.3 we describe the standard configuration that we use to derive the results we report as our best informed estimates. In section 2.4, we describe a number of reasonable alternative configurations. We use the offsets between results obtained with these plausible alternatives and the standard configuration as a basis for determining the uncertainty.

2.2 Data

This study relies on ocean interior observations of DIC, TA, S, T, O_2, $Si(OH)_4$, NO_3^-, and PO_4^{3-} collected in the global ocean from 1989 through 2020 (Fig. 1) and provided through GLODAPv2.2021 (Olsen et al., 2016; Lauvset et al., 2021). The apparent oxygen utilisation was calculated from oxygen, salinity, and conservative temperature (Graham and McDougall, 2013) according to the solubility from Weiss (1970) and used as an additional predictor variable. Observations were filtered based on the GLODAP flagging scheme, using only highest-quality data identified as those with a f-flag value of 2, which indicates acceptable, measured data according to a simplified version of the WOCE flagging scheme, and a qc-flag

value of 1, which indicates adjusted or unadjusted data that have undergone GLODAP's full secondary quality control. With a few exceptions, only samples were included for which all required variables fulfil the strictest quality criteria. We deviated from this only for cases where our tests of the eMLR(C*) method with synthetic data (see supplement S4) revealed that omitting observations because of only one missing variable increased the biases of the ΔC_{ant} reconstructions. In these cases either data that did not fulfil the strictest quality criteria were included (7609 samples, 3.7% of all samples), or missing data were filled (7305 samples, 3.5%) using CANYON-B (Bittig et al., 2018) predictions (see supplement S1.3). In total, we used 206'836 samples for our standard case reconstruction.

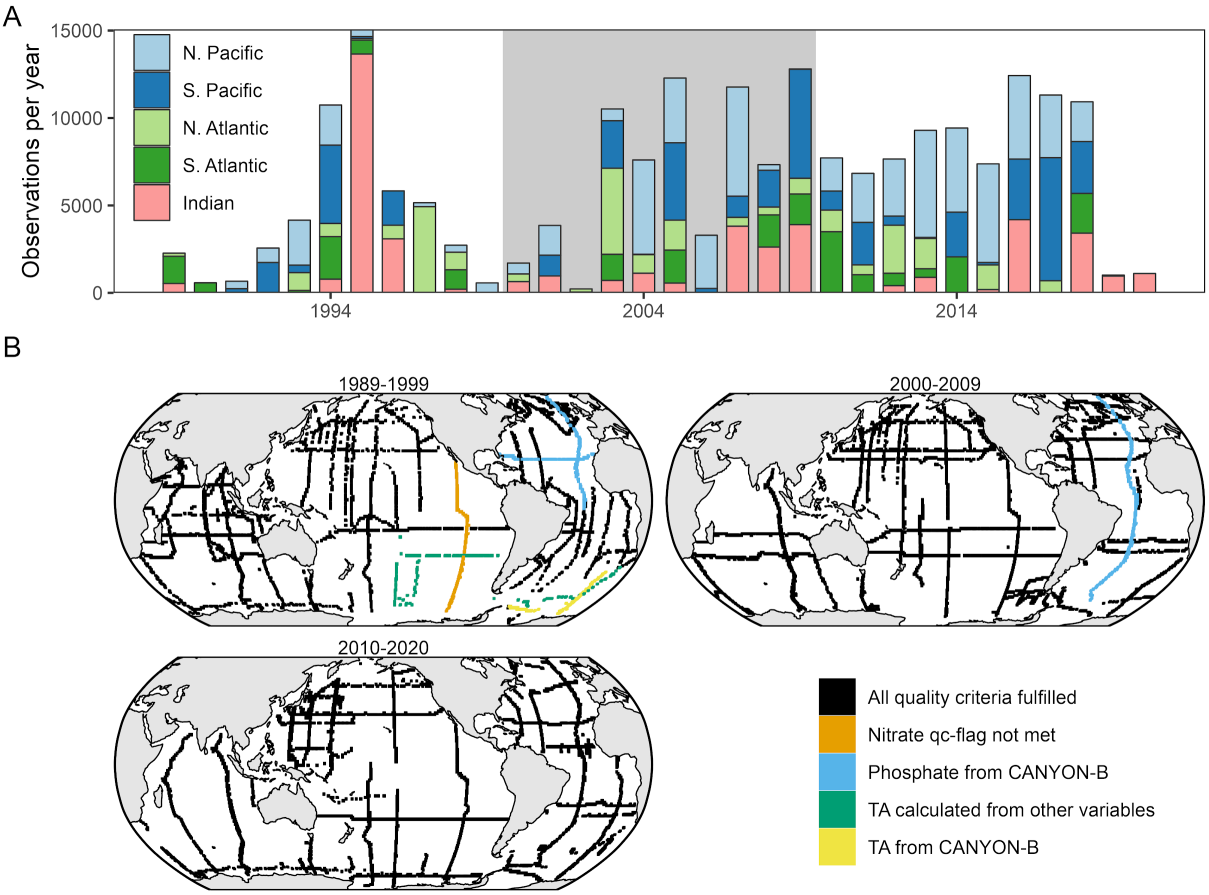

Fig. 1: Spatio-temporal coverage of observations from 1989–2020 as provided through GLODAPv2.2021 and after applying our flagging criteria. (A) Number of observations per year, where colours distinguish sampling regions according to the basin mask definition "5" in Fig. S1. The shaded background indicates the assigned sampling periods 1989–1999 ($t_{ref,1}$ = 1994), 2000–2009 ($t_{ref,2}$ = 2004), and 2010–2020 ($t_{ref,3}$ = 2014). (B) Map of observations as used in our standard case for the three sampling periods. Cruises that fulfilled all flagging criteria are displayed in black, while cruises for which one parameter did not fulfil all criteria but were still included (see also Table S1) are highlighted in colour.

Although the GLODAP data have already undergone a secondary quality control and are — if required — adjusted to improve their internal consistency, we applied a number of additional adjustments to the DIC, TA, and phosphate observations, based either on our decade-by-decade reanalysis of deep water crossovers originally determined by GLODAP, or on previously unaccounted offsets in the measurements of certified reference materials (CRM) for DIC and TA (see supplement S1.2 for details). This affected the majority of the DIC and TA measurements from the Indian Ocean in the 1990s (12843 samples, 6.2% of all samples), and the DIC, TA, and phosphate measurements in the North Pacific from the 2010s (35395 samples, 17.2% of all samples). Our adjustments of the Indian Ocean data have been formally accepted by GLODAP and were applied in the release of GLODAPv2.2022 (Lauvset et al., 2022). The magnitude of these additional adjustments are generally small (<2 µmol kg^{-1} for DIC, <4 µmol kg^{-1} for TA, and <1% for phosphate) and below the adjustment limits normally considered by GLODAP. Still, these adjustments proved to be critical in our work, since an offset of 1 µmol kg^{-1} in DIC integrated over 3000 m amounts to a column inventory offset of ~3 mol m^{-2}, which is of similar magnitude as some of the decadal changes we are aiming to detect.

For the purpose of predicting the C* distributions, we used the objectively analysed climatology for the 1981 – 2010 period for salinity and temperature from the World Ocean Atlas 2018 (Zweng et al., 2019; Locarnini et al., 2019), in combination with phosphate, nitrate, silicate and oxygen from the global interior ocean mapped climatology based on GLODAPv2 (Lauvset et al., 2016). The climatological distribution of AOU was calculated in accordance with the observational data.

2.3 Standard configuration of the eMLR(C*) method

In the following, we describe the main changes of the eMLR(C*) method in comparison to the previous analysis by Gruber et al. (2019). Further minor configuration changes are presented in supplement S2.

2.3.1 Temporal clustering and C* adjustment to reference year

For the temporal clustering of the data, we assigned each observation to one of the following three sampling periods (start and end years included):

1989–1999 ($t_{ref,1}$ = 1994)
2000–2009 ($t_{ref,2}$ = 2004)
2010–2020 ($t_{ref,3}$ = 2014)

with the assigned reference years (t_{ref}) given in parenthesis.

Based on these three sampling periods, we estimated the C_{ant} storage changes between the reference years 1994–2004 and 2004–2014 (Fig. 1). The ΔC_{ant} estimates represent the changes over exactly ten years, from mid-year of the first to mid-year of the second reference year. In addition, we determined ΔC_{ant} directly for the twenty year period 1994–2014.

The adjustment of C* from the time of sample collection (t) to the reference year (t_{ref}) was calculated as $C^*(t_{ref}) = C^*(t) - \delta(t) * C_{ant}(t_{ref})$, with $\delta(t) = \Delta CO_{2,atm}(t-t_{ref}) / \Delta CO_{2,atm}(t_{ref}-t_{pi})$, where t_{pi} indicates preindustrial times (~1800). We estimated the C_{ant} content in the reference year ($C_{ant}(t_{ref})$), by adding a proportional fraction of the reconstructed increase in C_{ant} over 13 years between 1994–2007 (ΔC_{ant}(1994–2007), Gruber et al., 2019) to the reconstructed C_{ant} in 1994 (C_{ant}(1994)), i.e., $\Delta C_{ant}(1994–t_{ref}) = (t_{ref}-1994) * \Delta C_{ant}(1994–2007) / 13$ years.

2.3.2 Spatial clustering and subsetting

For the fitting of the MLR models and mapping of ΔC_{ant} in the standard configuration, we clustered the observations and predictor climatologies horizontally into the Atlantic, Pacific and Indian Ocean, according to mask “3” of our basin mask definitions (Fig. S1). To assess the contribution of the impact of this choice on the uncertainty of the reconstructed changes in C_{ant}, we investigated five other basin configurations (Fig. S1). For clustering in the vertical dimension, we used the same neutral density levels as employed by Gruber et al. (2019). Surface water samples collected shallower than 100 m were excluded from the MLR fitting to avoid seasonally biased observations.

2.3.3 Mapping C* and ΔC_{ant}

The spatial distribution of C* was mapped by using the best MLR models of each reference year with climatological distributions of the predictor variables. For this purpose, the ten best MLR models within each spatial cluster were selected as those with the lowest summed RMSE for the two paired sampling periods following Clement and Gruber (2018). The ten individually mapped C* distributions were then averaged and subtracted to derive the mean

ΔC_{ant} distribution. In contrast to prior applications of the method, we included negative mapped ΔC_{ant} values, since (i) ΔC_{ant} can regionally be negative when water with low C_{ant} displaces water with high C_{ant}, (ii) setting negative values to zero could lead to positively biased ΔC_{ant} inventories, and (iii) our tests with synthetic data revealed a tendency to lower biases when negative values were retained.

2.3.4 Surface equilibrium ΔC_{ant}

In the standard configuration, the equilibrium ΔC_{ant} distribution at the sea surface was computed based on a rearranged definition of the Revelle factor, γ, as $\Delta C_{ant,eq}(t_{ref,n}–t_{ref,n+1}) = 1/\gamma \times DIC/pCO_2 \times \Delta pCO_{2,atm}(t_{ref,n+1}-t_{ref,n})$, where DIC, pCO_2 and γ are the climatological surface values (Lauvset et al., 2016) adjusted to the mean $pCO_{2,atm}$ of each analysis period. This adjustment of the climatological surface CO_2-system parameters to the mean $pCO_{2,atm}$ was achieved by calculating as a first step the surface pCO_2 in 2002 based on the climatological values for temperature, salinity, DIC and TA, which are normalised to the same year (Lauvset et al., 2016). In a second step, the surface ocean pCO_2 was shifted according to the change in $pCO_{2,atm}$, and DIC and γ were recalculated based on the new surface pCO_2. Thus, our surface equilibrium approach takes changes in the surface ocean buffer capacity into consideration. All CO_2-system calculations were done with the R-package seacarb (Gattuso et al., 2021) using the CO_2 dissociation constants from Lueker et al. (2000), the fluoride association constant from Perez and Fraga (1987) or Dickson & Riley (1979) at temperatures below 9°C and the acidity constant of hydrogen sulphide from Dickson (1990). To assess the uncertainties associated with this equilibrium ΔC_{ant} estimate, we also used an independent observation-based estimate of the increase in surface DIC (Gregor and Gruber, 2021).

While previous studies defined a distinct depth and neutral density threshold to separate water masses for which the surface equilibrium or eMLR(C*) reconstructions are used to determine ΔC_{ant}, we blend both estimates smoothly over the top 200 m. For this purpose, the equilibrium ΔC_{ant} is calculated at the sea surface only, while the eMLR-based ΔC_{ant} is initially mapped across the entire water column. In a post processing step, the surface- and eMLR-based ΔC_{ant} estimates are averaged proportionally according to the water depth across the upper 200 m (e.g., 75% surface-based and 25% eMLR(C*)-based estimate at 50 m water depth).

2.4 Computation of global ΔC_{ant} inventories

Column inventories and inventories of ΔC_{ant} in this study represent integrals across the upper 3000 m of the water column. ΔC_{ant} reconstructions below 3000 m are not included in integrals to avoid the imprint of ΔC_{ant} uncertainties that are small in terms of amount content but considerable in terms of integrated inventory changes. Instead, we follow previous studies and account for C_{ant} storage changes below 3000 m by adding 2% to our global ΔC_{ant} inventories. This deep ocean scaling represents the fraction of the total C_{ant} inventory in 1994 beneath 3000 m according to Sabine et al. (2004). We further scale our global inventories for the storage of C_{ant} in unmapped regions according to previously determined fractions of the global C_{ant} storage that occurs in these regions, namely 2% in the Arctic Ocean (Tanhua et al., 2009), 1.5% in the Mediterranean Sea (Palmiéri et al., 2015), 1% in the Nordic Seas (Olsen et al., 2010), and 0.3% in the Sea of Japan (Park et al., 2006). In sum, the upscaling amounts to 7% of our directly mapped global ΔC_{ant} inventory. Regional inventories refer to the integral of directly mapped ΔC_{ant} distributions and no areal scaling was applied, e.g., the regional inventory of the Atlantic Ocean does not account for storage in the Mediterranean Sea. Thus, our global inventory differs from the sum of the regional inventories by 7%.

2.5 Determination of uncertainty and method testing

The primary sources of uncertainty in the eMLR(C*) reconstructions of ΔC_{ant} are structural in nature and involve choices associated with the configuration of the method (Clement and Gruber, 2018, Gruber et al., 2019). According to our assessment, this involves primarily six configuration choices about (1) the regional clustering of the data, (2) the approach to perform data adjustments, (3) the nutrient used to compute the target variable C*, (4) the approach to estimate surface ocean ΔC_{ant}, (5) the gap-filling of flagged data, and (6) the choice of predictor climatologies. In addition, we consider (7) an uncertainty contribution in our global ΔC_{ant} inventories arising from the scaling to account for C_{ant} storage changes in unmapped waters.

To assess the impact of these choices and to obtain an estimate of uncertainty of our reconstructions, we have reconstructed a set of total 10 alternative estimates of ΔC_{ant} using modified choices for each of the six configurations listed above. These modifications of the eMLR(C*) configuration are described in detail in supplement S4. We base our estimate of uncertainty on the ΔC_{ant} offsets between the standard case and the reconstructions obtained

with the configuration changes. The individual offsets are considered as independent uncertainty contributions and combined as the square root of the sum of the squares (RSS) to derive the standard uncertainty ($\pm 1\sigma$) of our reconstructions, which we consider as a 68% confidence interval. Throughout the results and discussion, we report all results together with this $\pm 1\sigma$ uncertainty. In figures, we display also the expanded $\pm 2\sigma$ uncertainty representing a confidence interval of 95%. For each variable that is derived from a primary ΔC_{ant} estimate (e.g., the decadal difference between two ΔC_{ant} estimates, the ocean-borne fraction, etc.) we combine individual uncertainties through standard error propagation.

In order to independently assess the quality of our ΔC_{ant} reconstructions against a known truth, we use synthetic data generated from the global ocean biogeochemical model (GOBM) CESM-ETHZ (Doney et al., 2009; Hauck et al., 2020). The GOBM is a hindcast model forced with reanalysed atmospheric data and the observed atmospheric CO_2 trajectory. The synthetic data set is generated by subsetting the model output in space and time according to availability of real-world observations. The eMLR(C*) approach is then applied to the synthetic data set to reconstruct ΔC_{ant}. The comparison of the reconstructed ΔC_{ant} to the known model truth allows us to determine the biases of the reconstruction in terms of global or regional inventories, column inventory maps, or zonal mean sections. Details and results of this assessment are given in the supplement S5.

In order to assess the sensitivity of our reconstructions to other sources of uncertainty, such as the limited sampling of the spatio-temporal variability of the changes in DIC, we performed additional eMLR(C*) analyses, wherein we pushed the configurations beyond the limits of what we consider a reasonable modification. For example, we limited the observations to those from repeatedly occupied sections, used other DIC variants than C* as target variable and omitted any data adjustments (see section 4.2).

3 Results

3.1 Column inventories

The storage changes in anthropogenic carbon (ΔC_{ant}) integrated over the upper 3000 m (referred to as column inventories) reveal strong similarities during both decades of our analysis, i.e., between 1994 and 2004, and between 2004 and 2014 (Fig. 2A,B). The ΔC_{ant}

column inventories vary markedly with latitude. The highest mean decadal C_{ant} storage changes of about 10 mol m^{-2} dec^{-1} located near the centre of the subtropical gyres (30–40° N/S) are about twice as high as those in the equatorial regions (10° N/S) and in the Southern Ocean south of 60°S. In the Southern Hemisphere, the consistently high ΔC_{ant} column inventories in all subtropical gyres form a circumpolar band, while in the Northern Hemisphere the storage changes per unit area in the Atlantic exceed those in the Pacific roughly by a factor of two. The general patterns of our ΔC_{ant} reconstructions are reminiscent of those reconstructed for the pre-industrial to 1994 period (Sabine et al., 2004) and for the 1994 to 2007 period (Gruber et al., 2019), supporting in first approximation the expectation of a steady-state increase in the oceanic storage of C_{ant}. We also note that our ΔC_{ant} column inventory reconstructions for the 1994–2007 period (Fig. S6) confirm those reported by Gruber et al. (2019) for the same period, supporting the consistency of our approaches and estimates despite the modifications of the eMLR(C*) method and our use of an updated database.

While the general pattern of the increases in the C_{ant} column inventories are similar in the two decades, there are distinct differences (Fig. 2C). These decadal differences are most pronounced in the Atlantic Ocean, where we find a shift of the highest ΔC_{ant} column inventories from the Northern to the Southern Hemisphere. In the subtropical latitudes (20–50 °N) of the North Atlantic, the mean, area-weighted ΔC_{ant} column inventory in the second decade is 3.7 ± 0.8 mol m^{-2} dec^{-1} lower compared to the first one (1994–2004: 12.1 ± 0.5; 2004–2014: 8.4 ± 0.6 mol m^{-2} dec^{-1}; ± 1σ uncertainty). In contrast, the mean ΔC_{ant} column inventory in the subtropical latitudes of the South Atlantic (20–50 °S) is 4.7 ± 2.2 mol m^{-2} dec^{-1} higher in the second decade (1994–2004: 8.5 ± 0.9; 2004–2014: 13.2 ± 1.9 mol m^{-2} dec^{-1}). In other regions of the ocean, the decadal differences are within or close to the bounds of the uncertainty inferred from the alternative reconstructions. We thus refrain from further analysis. The spatial patterns in the decadal difference of our ΔC_{ant} column inventories are reminiscent of the anomaly structure that Gruber et al. (2019) derived from a comparison of their ΔC_{ant} column inventories to the steady-state projection of the total C_{ant} inventory in 1994 from Sabine et al. (2004).

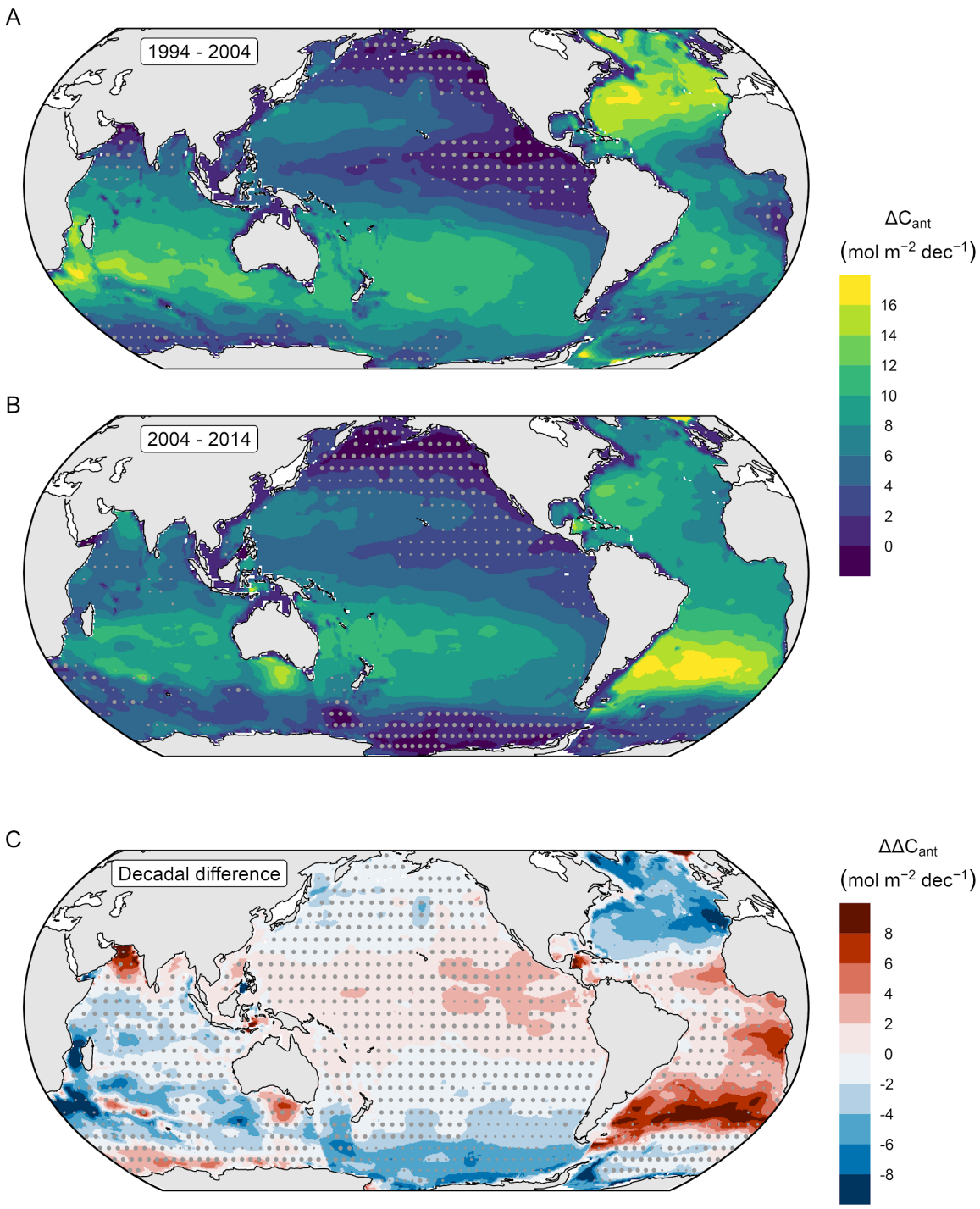

Fig. 2: Column inventory maps of the storage change of anthropogenic carbon (ΔC_{ant} in mol m^{-2} dec^{-1}) integrated over the upper 3000m of the ocean for (A) 1994–2004 and (B) 2004–2014. Decadal differences in the storage changes ($\Delta\Delta C_{ant}$) are shown in (C). Plotted here are the results from the standard configuration. Stippling with small or large dots on a 5°x5° grid indicates regions in which the ΔC_{ant} and $\Delta\Delta C_{ant}$ column inventories are lower than the 2σ- or 1σ-uncertainty, respectively.

3.2 Vertical distribution

The high column inventories of ΔC_{ant} in the centres of the subtropical gyres seen in Figure 2A,B are due to a deeper penetration of ΔC_{ant} in these regions. This is illustrated by plotting ΔC_{ant} along a global section (Fig. 3A,B) that connects the zonal mean sections of the Atlantic and Pacific Ocean with a meridional mean section crossing the Indian Ocean sector of the Southern Ocean. Within the subtropical gyres, ΔC_{ant} exceeding 5 µmol kg^{-1} dec^{-1} reaches at least 300 m deeper than in the equatorial regions. This is primarily a consequence of the passive tracer transport of C_{ant} along isopycnal surfaces (depicted in Fig. 3C), which brings C_{ant} more rapidly into the ocean's interior in regions of downward sloping isopycnals (Bopp et al., 2015; DeVries and Primeau, 2011). In the South Pacific, the ΔC_{ant} signal reaches deeper into the water column compared to the North Pacific, which is a persistent pattern for both decades and attributed to the formation of Subantarctic Mode and Antarctic Intermediate Water (SAMW and AAIW). In contrast, in the Atlantic Ocean we identify a shift of the deepest penetration of the ΔC_{ant} level of 5 µmol kg^{-1} dec^{-1} from the Northern to Southern Hemisphere (Fig. 3C).

These changes in the downward extensions of ΔC_{ant} cause the decadal differences identified in the column inventories of ΔC_{ant} in the Atlantic Ocean (Fig. 2C). The decrease of the mean ΔC_{ant} column inventory in the North Atlantic is a consequence of the weaker C_{ant} storage increase in the North Atlantic Deep Water (NADW), evident in the zonal mean section as negative decadal differences (-2 to -5 µmol kg^{-1} dec^{-1}) at neutral densities >27.5 kg m^{-3} (Fig. 3C). In contrast, the decadal increase of the ΔC_{ant} column inventory in the South Atlantic can be attributed to an intensified rate of C_{ant} storage in the Subantarctic Mode Waters (SAMW) and Antarctic Intermediate Waters (AAIW). Here, positive ΔC_{ant} differences in the zonal mean sections are well confined to the neutral density slabs ranging from 26.5 to 27.5 kg m^{-3} (Fig. 3C). The decadal ΔC_{ant} differences in the NADW and the AAIW are larger than the uncertainty of our reconstructions, while in most other water masses, the decadal differences are not significant (stippled regions in Fig. 3C).

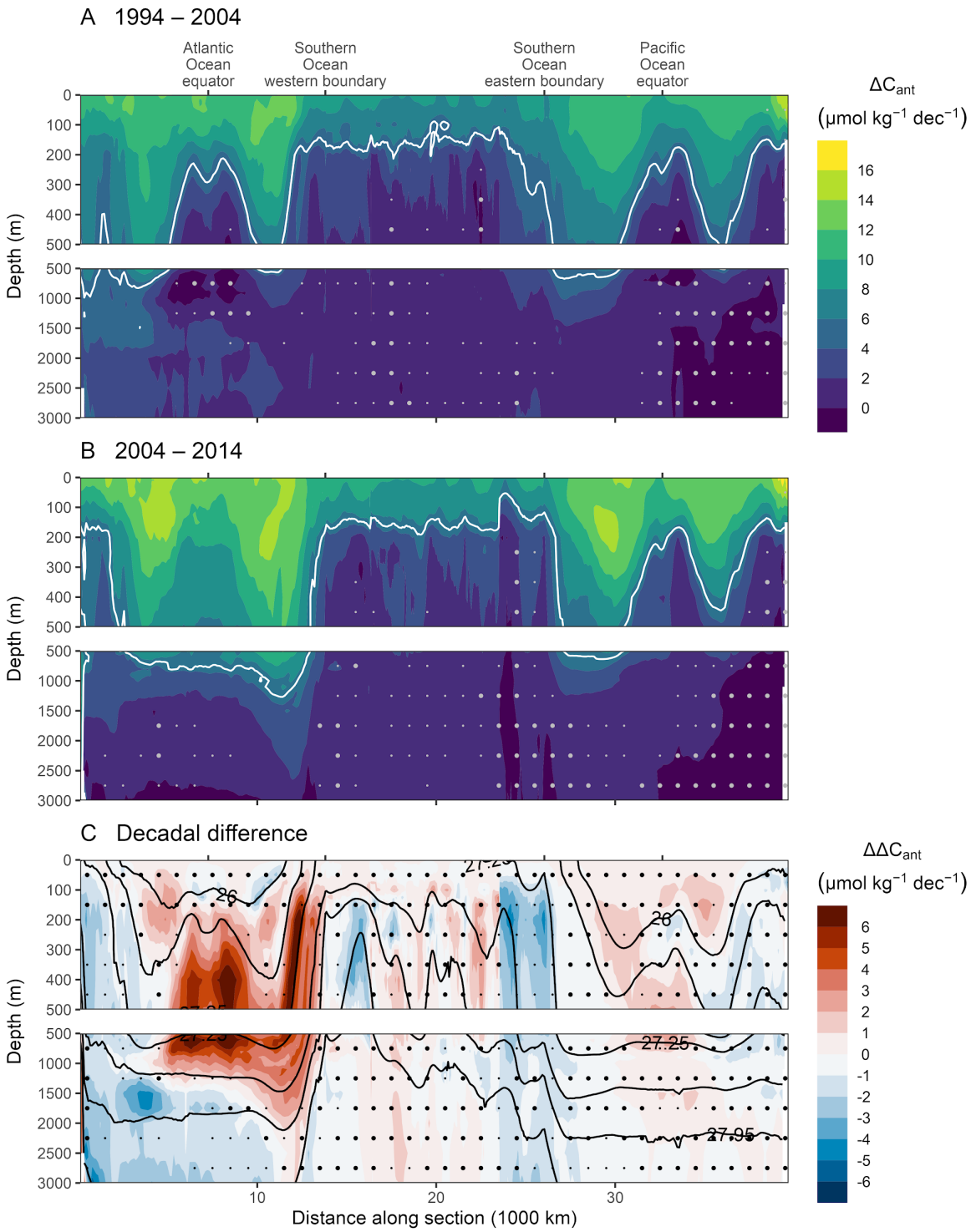

Fig. 3: Global sections of changes in the anthropogenic carbon content from north to south in the Atlantic Ocean, west to east in the Southern Ocean and south to north in the Pacific Ocean. The standard case reconstruction of ΔCant (in μmol kg^{-1} dec^{-1}) is shown for the decades (A) 1994–2004 and (B) 2004–2014. The white contour lines highlight the ΔC_{ant} level of 5 μmol kg^{-1} dec^{-1}. (C) Decadal differences between the storage changes ($\Delta\Delta C_{ant}$) shown in (A) and (B). Black contour lines in (C) indicate isoneutral density levels. The selected contours represent every second density slab used to cluster the data in the vertical dimension. Stippling with small or large dots indicates regions in which

the ΔC_{ant} and $\Delta\Delta C_{ant}$ column inventories are lower than the 2σ- or 1σ-uncertainty, respectively. The North-South sections through the Atlantic and Pacific Ocean show zonal mean values across the entire basins, while the Southern Ocean sector is represented by a meridional mean section ranging from 55 to 65°S.

Examining the vertical distribution of the reconstructed ΔC_{ant} in terms of area-weighted mean content profiles (Fig. 4A), we find that globally C_{ant} in the upper 50 m of the ocean increased on average by 10 – 11 µmol kg^{-1} dec^{-1} in both periods. As the storage change near the surface is determined based on an assumed equilibrium with the atmospheric pCO_2, it shows latitudinal patterns that reflect gradients in the surface ocean buffer capacity (Fig. 3AB). However, regional differences of the surface ΔC_{ant} averaged over hemispheric ocean basins are small (Fig. 4A). Furthermore, the almost identical surface ΔC_{ant} for both decades is due to a compensation of the higher atmospheric pCO_2 growth rate and the reduced surface ocean buffer capacity in the second decade of our analysis. The global mean penetration depth of ΔC_{ant}, which we define as the mean column inventory (Fig. 2) divided by the mean surface content (Fig. 4A), is similar for both decades and extends to 640 ± 45 m and 560 ± 45 m for the 1994–2004 and 2004–2014 periods, respectively. However, this penetration depth varies remarkably across the individual ocean basins. In the North Pacific, the mean penetration depth of ΔC_{ant} does not exceed 300m, while in the Southern Hemisphere, the penetration depth exceeds 600 m in all ocean basins and decades. In the South Atlantic, we find a pronounced deepening of the penetration depth from 630 ± 80 m in the first decade to 870 ± 100 m in the second decade. In the North Atlantic the penetration depth changes in the opposite direction and decreases from 830 ± 30 m to 670 ± 50 m.

The decadal differences in the penetration depth are directly related to patterns in the mean ΔC_{ant} profiles. In the North Atlantic, ΔC_{ant} below 1000m is about 3 µmol kg^{-1} dec^{-1} lower during the second decade (Fig. 4A), while the mean ΔC_{ant} signal in the South Atlantic was significantly higher by about 3 µmol kg^{-1} dec^{-1} between 500 and 1500m during the second decade.

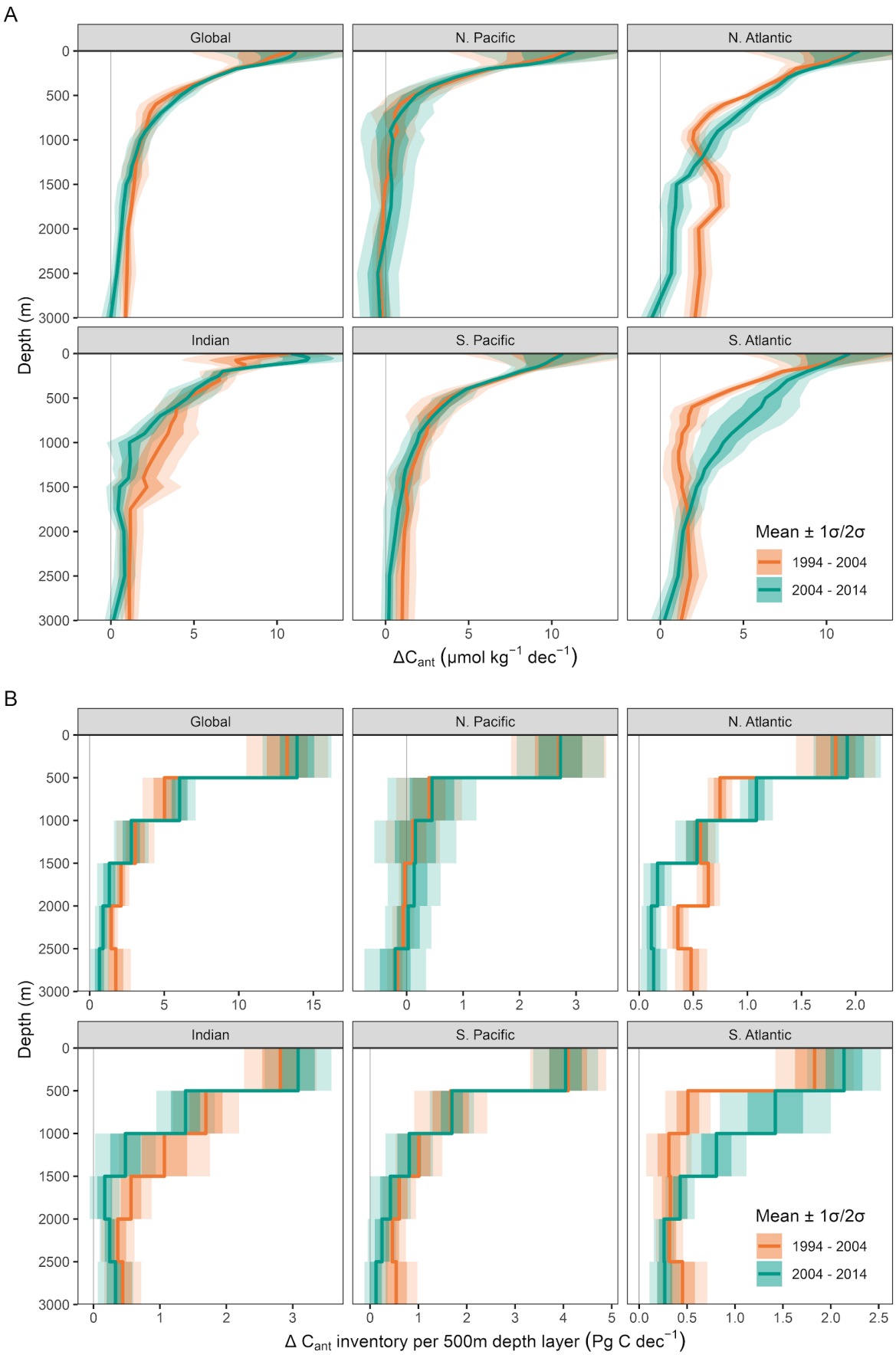

Fig. 4: Mean vertical distribution of the decadal changes in anthropogenic carbon (ΔC_{ant}) for the

global ocean and both hemispheres of the main ocean basins. (A) Mean profiles and (B) 500m-depth layer inventories of ΔC_{ant}. Colours distinguish the decades 1994–2004 and 2004–2014. Thick lines represent the standard case reconstruction of ΔC_{ant} and ribbons indicate the 1σ- and 2σ-uncertainty ranges.

3.3 Regional and global inventories

Reflecting the rapid decrease of ΔC_{ant} with depth (Fig 4A), almost 50% of the global C_{ant} storage change occurs in the upper 500 m of the water column (Fig. 4B). Over the upper 1000 m, this share increases to around 75%, except in the North Pacific, where the entire inventory increase is fully confined to the top 1000 m. In all other ocean regions depicted in Figure 4B, a significant fraction of the C_{ant} storage change occurs below 1000 m (~25% on a global basis) as a result of the more rapid water mass transport and mixing between the surface and ocean interior in these regions. The decadal differences in the ΔC_{ant} inventories for 500 m depth layers reflect the profiles of the amount content and were found to be significant only in the three depth layers below 1500m of the North Atlantic, as well as between 500 and 1500 m in the South Atlantic (Fig. 4B).

Once integrated over the top 3000 m of entire ocean basins, (Fig. 5 and Table 1), the South Pacific stands out as the region with the highest increase of C_{ant} storage for both decades (1994–2004: 8.6 ± 1.2 Pg C dec^{-1} and 2004–2014: 7.4 ± 1.0 Pg C dec^{-1}), followed by the Indian Ocean (7.2 ± 0.9 and 5.7 ± 0.6 Pg C dec^{-1}). In contrast, the North Pacific accounts for the smallest contribution to the increase in the oceanic storage of C_{ant} in both decades (2.9 ± 0.8 and 3.2 ± 1.8 Pg C dec^{-1}). The decadal differences in the increases in C_{ant} storage are not significant at the 2σ-uncertainty level in any of these three regions. This is different for the North Atlantic (Fig. 5, Table 1), which represented the third largest sink region during the 1994–2004 decade (4.8 ± 0.2 Pg C dec^{-1}), but experienced a C_{ant} accumulation rate that was significantly reduced by 0.9 ± 0.4 Pg C dec^{-1} during the 2004–2014 period (3.9 ± 0.4 Pg C dec^{-1}). In contrast, the storage rate in the South Atlantic increased by 1.5 ± 0.8 Pg C dec^{-1} from the first (3.9 ± 0.5 PgC dec^{-1}) to the second decade (5.4 ± 0.6 Pg C dec^{-1}) of our analysis. As a consequence, the South Atlantic represents the third largest contributor to the global accumulation of C_{ant} from 2004 to 2014. The ranking of the ocean basins in terms of their contribution to the global ocean C_{ant} sink reflects primarily the differences in surface area of the basins.

In terms of the storage efficiency normalised to the surface area, i.e. $\beta = \Delta C_{ant} / \Delta pCO_{2,atm}$

(mol m^{-2} µatm^{-1}), the ranking of the regions changes markedly (Table 1 and Fig. S5). The North Atlantic reveals the highest regional storage efficiency (25–40% larger than the global mean), and the North Pacific the lowest one (about 45–55% lower than the global mean). This largely reflects the differences in intermediate, mode, and deep water formations between the different basins, and will be further discussed in section 4.1.

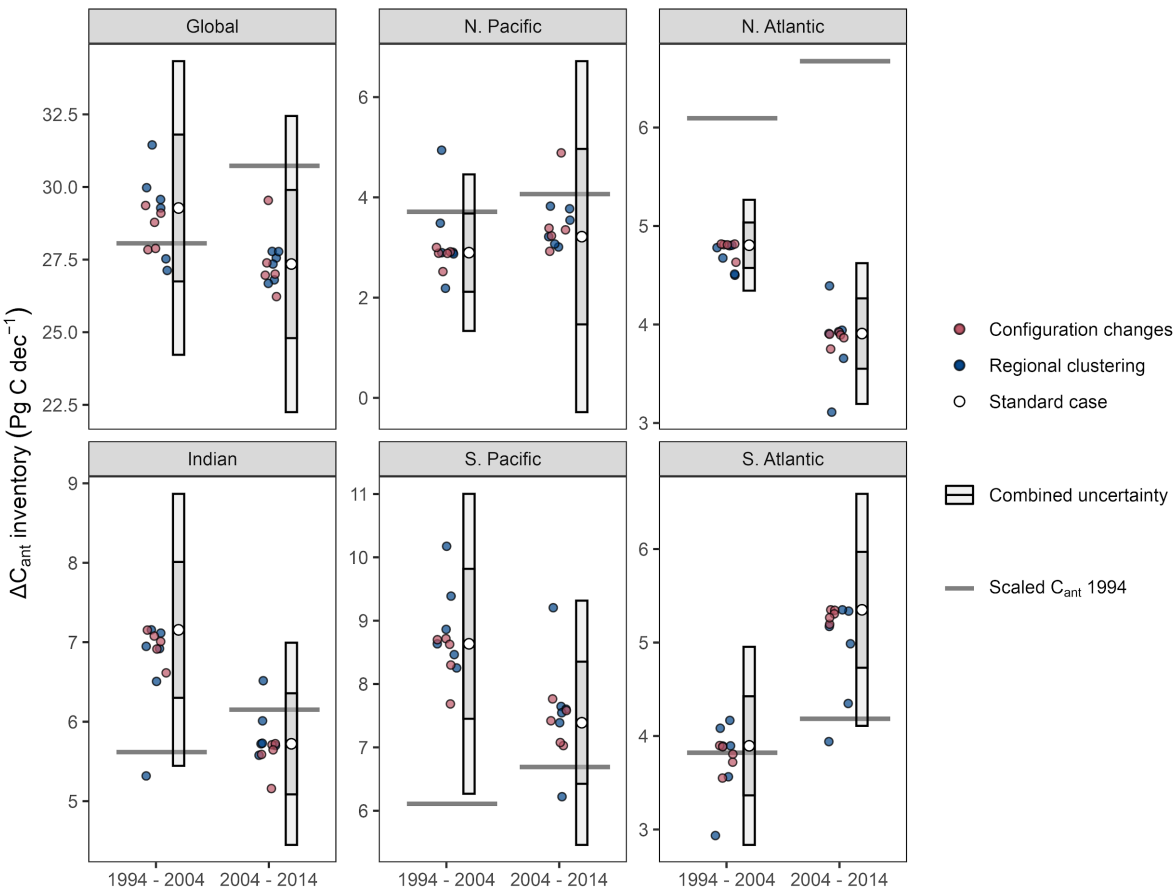

Fig. 5: Inventories of the change in the anthropogenic carbon storage (ΔC_{ant} in Pg C dec^{-1}) for each hemisphere of the main ocean basins and the global ocean, and the decades 1994–2004 and 2004–2014. White symbols represent the standard case of our ΔC_{ant} reconstructions and error bars the 1σ- and 2σ-uncertainty range. Horizontal lines indicate projected inventories based on the total C_{ant} storage in 1994 (Sabine et al., 2004) and assuming proportional growth with atmospheric CO_2. Coloured points represent ΔC_{ant} reconstructions considered in the uncertainty assessment (red: configuration changes of the eMLR(C*) method; blue: regional clustering) and are arbitrarily spaced in the horizontal direction for visibility.

When integrating ΔC_{ant} globally and scaling it for unmapped regions and deep water storage, we determine an ocean sink for anthropogenic CO_2 that amounts to 29.3 ± 2.5 and 27.3 ± 2.5 Pg C dec^{-1} for the 1994–2004 and the 2004–2014 decade, respectively (Fig. 5, Table 1).

These inventory changes of C_{ant} are indistinguishable for both decades with a difference of -1.9 ± 3.6 Pg C dec^{-1}, indicating that the global ocean continued to act as a strong sink for anthropogenic CO_2 in the recent past. The efficiency β of the global C_{ant} sink decreased markedly and significantly, however, from 0.37 ± 0.03 mol m^{-2} μatm^{-1} for the decade 1994–2004 to 0.31 ± 0.03 mol m^{-2} μatm^{-1} during the second decade 2004–2014 (Table 1). For the 20-year period from 1994–2014, the directly estimated global ΔC_{ant} inventory is identical to the sum of the estimates from the individual decades (56.7 ± 3.5 Pg C dec^{-1}).

Table 1: Inventories of the change in anthropogenic carbon storage (ΔC_{ant} in Pg C dec^{-1}) and the corresponding sink efficiency ($\beta = \Delta C_{ant} / \Delta pCO_{2,atm}$ in mol m^{-2} μatm^{-1}) for the first (1994–2004) and second (2004–2014) decade of our analysis. Inventories are integrated separately across both hemispheres of the main ocean basins and the global ocean. All values refer to the standard cases of our ΔC_{ant} reconstruction and the 1σ-uncertainty ranges. Decadal inventory differences are tagged with ** or * when they exceed the combined 2σ- or 1σ-uncertainty of both decades, respectively.

Region	**Estimate**	**1994–2004**	**2004–2014**	**Decadal difference**
Global	**ΔC_{ant}**	29 ± 2.5	27 ± 2.5	-1.9 ± 3.6
	β	0.37 ± 0.03	0.31 ± 0.03	-0.05 ± 0.04 *
Indian	**ΔC_{ant}**	7.2 ± 0.9	5.7 ± 0.6	-1.4 ± 1.1 *
	β	0.44 ± 0.05	0.32 ± 0.04	-0.12 ± 0.06 *
N. Pacific	**ΔC_{ant}**	2.9 ± 0.8	3.2 ± 1.8	0.3 ± 1.9
	β	0.17 ± 0.05	0.17 ± 0.09	0.002 ± 0.1
S. Pacific	**ΔC_{ant}**	8.6 ± 1.2	7.4 ± 1.0	-1.2 ± 1.5
	β	0.40 ± 0.06	0.31 ± 0.04	-0.09 ± 0.07 *
N. Atlantic	**ΔC_{ant}**	4.8 ± 0.2	3.9 ± 0.4	-0.9 ± 0.4 **
	β	0.53 ± 0.03	0.39 ± 0.04	-0.14 ± 0.04 **
S. Atlantic	**ΔC_{ant}**	3.9 ± 0.5	5.4 ± 0.6	1.5 ± 0.8 *
	β	0.39 ± 0.05	0.49 ± 0.06	0.1 ± 0.08 *

3.4 Uncertainty assessment

Nearly all identified main configuration choices of the eMRL(C*) method matter for the reconstruction of the decadal increases in C_{ant} and contribute to the uncertainties of the global inventory changes of about ±10% (Table 1, Figs. 6 and S9). The smallest uncertainty contributions stem from alternative definitions of C* and from uncertainties associated with

the predictor climatologies used for mapping (Fig. 6). All other configuration choices matter more, although differently for the two decades, largely reflecting differences in the data distribution and data consistency.

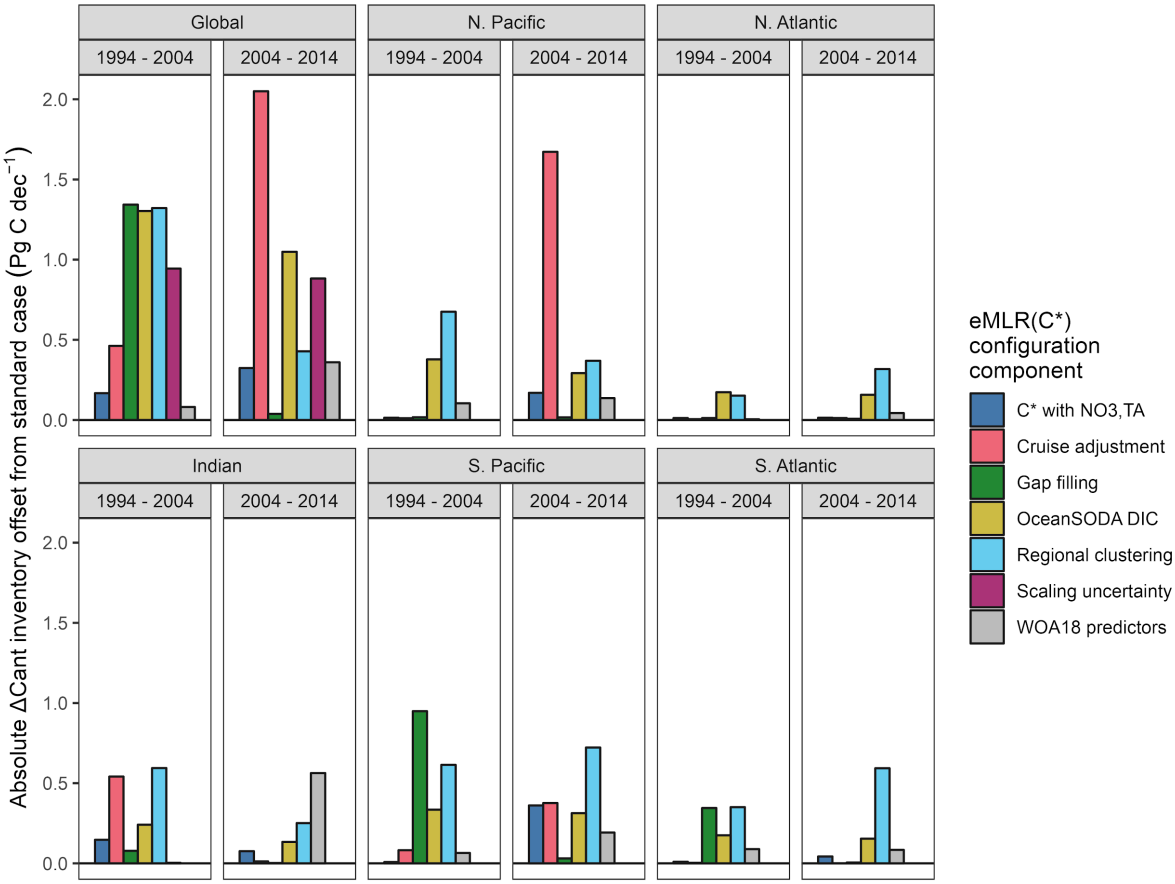

Fig. 6: Inventory uncertainty contributions at the 1σ-uncertainty level determined as offsets between our standard case reconstruction and six configuration choices of the eMLR(C*) method (colours) for each ocean region and both decades (panels). All offsets are shown as absolute values. The uncertainty contribution that accounts for our upscaling for unmapped water masses is shown for the global inventory.

The single largest contribution to the global inventory uncertainty comes from the way we applied the adjustments to the DIC, TA and PO_4^{3-} measurements in order to ensure the highest level of data consistency. If the adjustments were determined and applied separately for each cruise instead of in a bulk manner as done in the standard configuration, the global ΔC_{ant} inventories change by ~-0.5 Pg C dec^{-1} during the 2004-2014 period, and by ~+1.5 Pg C dec^{-1} for the 2004-2014 period. Nearly all of the changes during the earlier decade originate at the Indian Ocean, while those for the second period originate at the North Pacific (Figs. 6 and

S9), as expected given that these were the regions where we applied these adjustments.

The second most important uncertainty contribution comes from the regional clustering of the observations with uncertainty contributions to the regional inventories ranging from 0.2 to 0.8 Pg C dec^{-1} (Figs. 6 and S9). However, for the global ΔC_{ant} inventories, the uncertainties arising from the regional clustering partially cancel out, such that the global uncertainty contribution is lower than the sum of the uncertainties in the individual basins (<1.5 Pg C dec^{-1} for both decades, Fig. 6).

Among the other choices, the approach for the surface ΔC_{ant} reconstruction contributes about 1 Pg C dec^{-1} to the uncertainty of the global ΔC_{ant} inventory, determined by comparing our estimate based on the assumption of surface ocean equilibrium of C_{ant} with a reconstruction based on observation-based surface changes of DIC (Gregor and Gruber, 2021). Choices associated with the gap filling also contribute about 1 Pg C dec^{-1} to the global uncertainty, but this error source is limited largely to the first decade and the South Pacific (Fig. S9), where we had to include a substantial number of cruises that took place in the 1990s and provided only calculated TA data (Fig. 1). Finally, our scaling of the ΔC_{ant} inventories for unmapped regions and the deep ocean introduces an additional uncertainty contribution of about 1 Pg C dec^{-1}, however, confined to the global ΔC_{ant} inventories and of very similar magnitude for both decades.

In addition to investigating the contribution of the configuration choices to the uncertainty of our standard configuration, we also determined the sensitivity of our results to a set of additional decisions we had to take for our reconstructions (see section S4.2). We did not add these results to our formal uncertainty estimate since we consider our choices as well justified, and the alternatives as clearly inferior choices. Analogous to our finding above for the contribution to the assessed uncertainty, we find that the biggest sensitivity of the results is associated with the data adjustments. Reconstructions of ΔC_{ant} based on the unadjusted data reveal biases (Fig. S11 and S12) that are more than a factor of two larger than our estimated adjustment uncertainty. Furthermore, we tested the sensitivity of our results to data coverage by reconstructing ΔC_{ant} with observations only from cruise sections that were reoccupied during both sampling periods. This reoccupation filter has generally a low impact on the reconstructed column inventories and basin inventories (Fig. S11 and S12), suggesting an overall sufficient data coverage. An exception to this are the ΔC_{ant} reconstructions in the

Indian Ocean, which are more sensitive to the reoccupation filter (Fig. S11) due to the lack of data from the Arabian Sea during the central sampling period, i.e., the 2000s (Fig. 1B).

Our observation-based uncertainty and sensitivity findings are corroborated by our tests with synthetic data generated from an ocean hindcast model (supplement S5), following the approach developed by Clement and Gruber (2018). Comparing the biases of our reconstructed model inventories to the estimated uncertainty based on the configuration choices, we find that the bias of 7 (11) out of 12 reconstructed ΔC_{ant} inventories is within the 1σ- (2σ-) uncertainty range (Fig. S18), which meets the expectation of a 68% (95%) confidence interval. Our uncertainty ranges and confidence intervals are thus considered suitable criteria to evaluate the significance of our ΔC_{ant} reconstructions. Furthermore, the eMLR(C*) method proves capable of reconstructing the global ΔC_{ant} patterns (Fig. S13). The reconstruction biases of the ΔC_{ant} column inventories are below 2 mol m^{-2} dec^{-1} for 87% of the total ocean surface area, within 2 – 4 mol m^{-2} dec^{-1} for 13%, and only exceed the latter threshold for <0.5% of the surface area. In contrast, the true ΔC_{ant} column inventories in our model are larger than these thresholds of 2 and 4 mol m^{-2} dec^{-1} over more than 90 and 55% of the surface area of the ocean, respectively (Fig. S13A). In agreement with this assessment based on synthetic data, the observation-based ΔC_{ant} column inventories exceed the 1σ- and 2σ-uncertainty level over more than 90 and 75% of the total ocean surface area (Fig. 2A). ΔC_{ant} column inventories that are lower than the local uncertainty are confined to regions with low ΔC_{ant} column inventories, primarily in the North Pacific (Fig. 2A). We conclude that the global distribution patterns of ΔC_{ant} are robustly reconstructed, which is in line with previous assessments of the method (Clement and Gruber, 2018) despite the shorter sampling periods applied in this study.

While the tests with synthetic data demonstrate the ability of the eMLR(C*) method to reconstruct spatial patterns in ΔC_{ant}, the low decadal variability of the current generation of ocean hindcast models (Hauck et al., 2020) impedes the assessment of the method's ability to detect decadal differences in the C_{ant} storage rates ($\Delta\Delta C_{ant}$). As a consequence of the model's low decadal variability, the spatial patterns in the column inventory biases show a strong correlation with the reconstructed $\Delta\Delta C_{ant}$ (Fig. S14 and S15). However, the observation-based $\Delta\Delta C_{ant}$ column inventories in the Atlantic Ocean (Fig. 2B) are higher than the $\Delta\Delta C_{ant}$ biases in the tests with synthetic data by about a factor of two (Fig. S15), suggesting that the observation-based $\Delta\Delta C_{ant}$ patterns carry, at least in part, a true signal.

3.5 Comparison with regional estimates

As a final component to assess the robustness of our estimates, we compare our ΔC_{ant} reconstructions to previous regional estimates that — same as our study — resolve changes for at least two periods and apply an MLR approach to ocean interior observations (see supplement S6 for details). Regional studies that fulfil these criteria are available for the North and South Atlantic (Woosley et al., 2016; Wanninkhof et al., 2010; Gao et al., 2022), as well as the North and South Pacific (Carter et al., 2019). We conclude from this comparison that the magnitude, patterns and trends in our ΔC_{ant} reconstructions agree with those determined in regional studies, and that differences can — where they exist — be attributed to differences in the chosen integration depth, differences in the definition of the target variable C*, and sometimes also to the uncertainty associated with the computation of a whole basin inventory from a single reoccupied transect (Woosley et al., 2016; Gao et al., 2022).

The most pronounced difference to a regional estimate exists in the South Pacific, where Carter et al. (2019) determined a change of the C_{ant} inventory of 5.4 ± 0.6 Pg C dec^{-1} from 1995 to 2005, whereas we determine a substantially higher inventory change of 8.6 ± 1.2 Pg C dec^{-1} for almost the same period (1994 – 2004). A main difference between these studies is the calculation of C* without (Carter et al., 2019) or with (this study) a TA contribution. Our sensitivity reconstruction of ΔC_{ant} in the South Pacific without considering the contribution of TA for the calculation of C* indeed reveals an inventory change that is about 3 Pg C dec^{-1} lower than our standard case reconstruction. Carter et al. (2019) relied on a synthetic data sensitivity test that included synthetic measurement uncertainties to conclude that the eMLR results are more robust for their implementation when the TA adjustment is omitted from the C* calculation. However, methodological differences between the methods used in that and our study limit the applicability of their sensitivity tests for our approach. We further contend that the additional attention paid to TA quality control results in better TA consistency between cruises than is assumed by Carter et al. (2019) and that the possibility of DIC changes driven by the calcium carbonate cycle (that are neither well represented in the synthetic data nor sufficiently correlated with nutrient and oxygen changes that they would be removed by following the eMLR approach) should not be neglected.

The second largest difference from a regional ΔC_{ant} inventory exists in the North Atlantic Ocean, where Wanninkhof et al. (2010) determined a C_{ant} storage rate of only 1.9 ± 0.4 Pg C dec^{-1} for the 1989–2003 period based on a single reoccupied cruise section. Their estimate is drastically lower than ours for the 1994–2004 decade (4.8 ± 0.2 Pg C dec^{-1}). Our tests of the eMLR(C*) method reveal that the uncertainty of our estimates can only explain a minor part of this offset. We conclude that the offset is primarily due to differences in the integration depth, structural uncertainties in the regional estimate (Wanninkhof et al., 2010) and extrapolation errors from a single reoccupied cruise section to a whole basin inventory. In fact, Woosley et al. (2016) found that the whole basin inventories of the North Atlantic differ by ~30% when comparing estimates obtained from a single section to those obtained from three sections.

In general, the individual differences between our regional ΔC_{ant} inventories and those obtained in the previous regional studies are within the uncertainty range of our global inventory. Therefore, we do not assume that offsets at the regional scale challenge the robustness and interpretation of our global inventories.

4 Discussion

4.1 Decadal trends or *the ocean at a time of change*

In this study we found that the rates of the increases of the global oceanic storage of anthropogenic carbon for the two consecutive decades since 1994 are indistinguishable, i.e., 29.3 ± 2.5 Pg C dec^{-1} and 27.3 ± 2.5 Pg C dec^{-1} for the 1994–2004 and the 2004–2014 decade, respectively (Fig. 5, Table 1). Putting this continued accumulation of anthropogenic carbon into the context of the total oceanic C_{ant} storage for 1994 (118 ± 19 Pg C), we identify an almost perfect linear correlation with the increase in atmospheric pCO_2 (Fig. 7, see also Gruber et al., in press). For a more detailed and quantitative discussion of the recent decadal trends in the ocean carbon sink, it is thus informative to relate the storage changes in C_{ant} to the increase in atmospheric pCO_2, i.e. in terms of the efficiency β (see section 3.3).

At the global scale, we find that the ocean's efficiency to accumulate anthropogenic carbon shows first signs of a weakening, i.e., β decreased significantly by 15% from 0.37 ± 0.03 mol

m^{-2} μatm^{-1} during the 1994–2004 decade to 0.31 ± 0.03 mol m^{-2} μatm^{-1} during the 2004 to 2014 decade (Table 1, Figs. 7 and 8). In contrast, the reduction of the accumulation of C_{ant} from the first to the second decade by 1.9 ± 3.6 Pg C dec^{-1} represents only a 7% decrease and is not significant. The fact that the decadal decline in β is more robust than that of the ΔC_{ant} inventory itself is due to the ~10% higher growth rate in atmospheric pCO_2 from 2004 to 2014 ($\Delta pCO_{2,atm}$ = 20.4 µatm dec^{-1}) compared to that during the previous decade from 1994 to 2004 (18.6 µatm dec^{-1}).

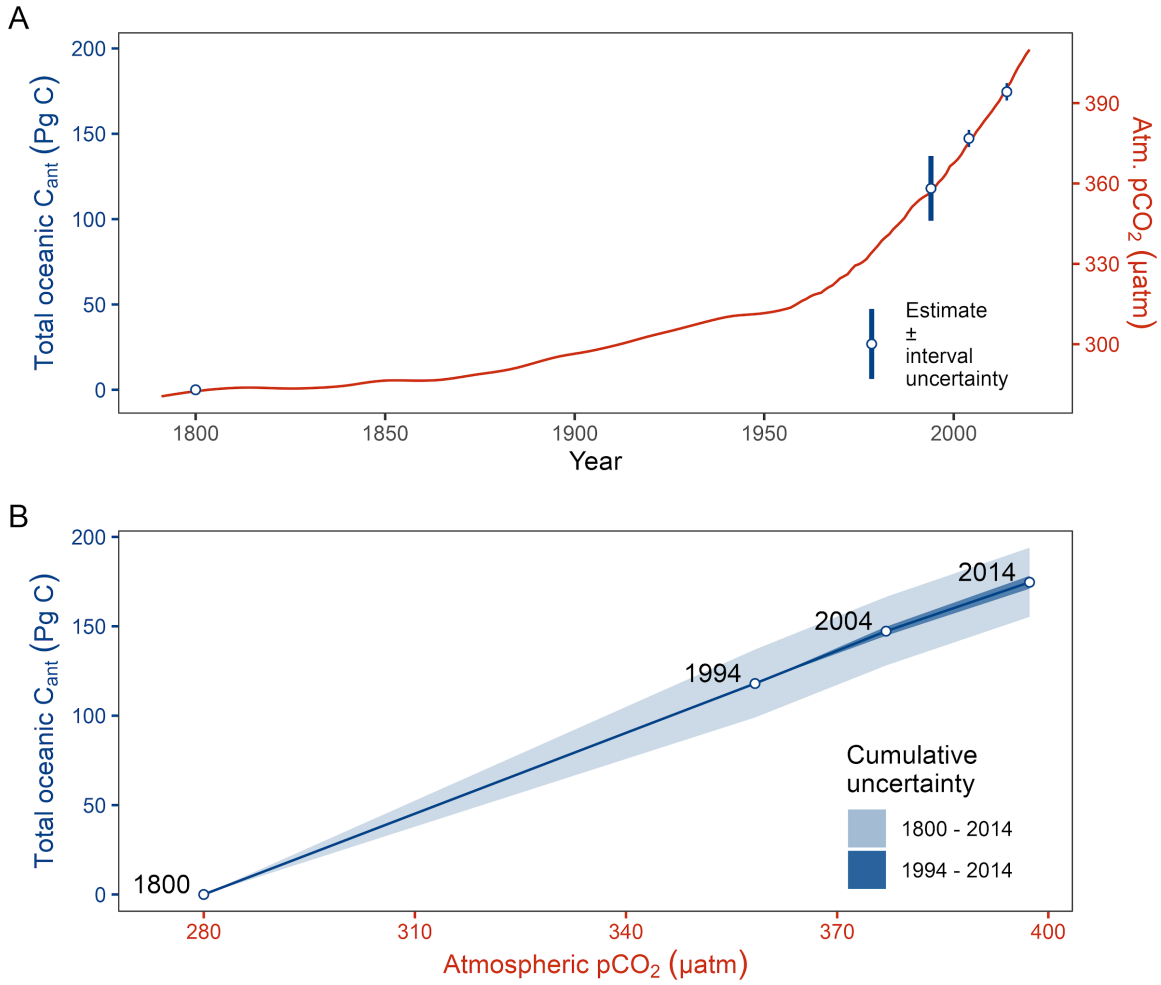

Fig. 7: Total C_{ant} accumulation in the ocean interior from 1800–2014, shown in blue as a function of (A) time and (B) atmospheric pCO_2. Total C_{ant} was estimated by adding our global ΔC_{ant} inventories (Table 1) to the total C_{ant} inventory in 1994 (118 ± 19 Pg C) according to Sabine et al. (2004). The red line in (A) shows the time history of atmospheric pCO_2. The cumulative uncertainty in (B) for the 1994–2014 period (dark blue ribbon) assumes zero uncertainty in 1994.

As the ocean acidifies in response to taking up CO_2, a decrease of the ocean sink efficiency is expected due to the decrease of the ocean buffer capacity (Jiang et al., 2019). Over the past 40 years, seawater that followed the same pCO_2 increase as the atmosphere would have experienced a ~6% reduction of the DIC increase per change in pCO_2 roughly every ten years according to fundamental marine CO_2-system considerations. This 6% decadal weakening of the ability of the surface ocean carbonate chemistry to buffer the increase in pCO_2 would explain about half of the observed decrease in the sink efficiency. The other half is most likely attributable to changes in the ocean's circulation and upper ocean stratification (Sallée et al., 2021) that appears to have led to a less efficient downward transport of C_{ant}, which we discuss further in the following.

Roughly half of the decrease of the global ocean carbon sink stems from the reduced decadal storage changes in the North Atlantic (-0.9 ± 0.4 Pg C dec^{-1}). Here, we find a significant weakening of the sink efficiency β (-0.14 ± 0.04 mol m^{-2} μatm^{-1}) when comparing the first (1994–2004) to the second decade (2004–2014) of our analysis (Table 1, Figs. S4,S5). Furthermore, our β estimates for both decades are well below that obtained for the 1800–1994 period (Sabine et al., 2004), indicating a progressive weakening of the sink efficiency in the North Atlantic. The most plausible explanation for this progressive weakening is a tendency of the Atlantic Meridional Overturning Circulation (AMOC) to weaken since the 1980s (Latif et al., 2022; Jackson et al., 2022, 2019). Attributing the decadal ΔC_{ant} differences to changes in AMOC strength is supported by the localization of the negative $\Delta\Delta C_{ant}$ signal in the North Atlantic Deep Water (Fig. 3C). This view is also in line with two previous sets of regional studies: (i) (Pérez et al., 2010, 2013) found that the C_{ant} storage rates in the North Atlantic subpolar gyre during the phase of a low North Atlantic Oscillation (NAO) from 1997–2006 were ∼48% lower than those during the first half of the 1990s, when a high NAO phase was dominant, although the mechanistic processes linking the NAO, subpolar convection strength, gyre circulation and the AMOC are not yet fully understood. (ii) Raimondi et al. (2021) reconstructed C_{ant} column inventories in the Central Labrador Sea based on CFC-12 observations and identified a period of near zero C_{ant} increases between 2003 and 2012.

However, an important caveat regarding our finding of a progressively weakening North Atlantic C_{ant} sink is the fact that the available ocean interior observations in the North Atlantic stem mostly from the first half of our last sampling period, the 2010s. However, past

2013 the NAO switched to a strong positive phase (Holliday et al., 2020) and in line with this the C_{ant} column inventories in the Central Labrador Sea rapidly increased (Raimondi et al., 2021). Likewise, a deep convection event in the Irminger Sea in winter 2014/15 injected anthropogenic carbon into the ocean interior and almost tripled the storage rates compared to those determined from previous hydrographic sections (Fröb et al., 2016). It is thus possible that our reconstructions do not capture a very recent reinvigoration of the North Atlantic C_{ant} sink, due to the temporal distribution of observations.

The decadal difference of the South Atlantic C_{ant} sink is significant on the 1σ-uncertainty level (+1.5 ± 0.8 Pg C dec^{-1}) and slightly exceeds the increase expected from the growth in atmospheric pCO_2 alone, expressed in an increase of the sink efficiency (+0.1 ± 0.08 mol m^{-2} μatm^{-1}). In contrast to the North Atlantic, the decadal change in the South Atlantic is not of progressive nature when putting it into context of the total C_{ant} storage until 1994 (Fig. 5), i.e. only the second decade reveals a tendency towards an elevated storage efficiency. Due to the strong spatial coherence between the positive $\Delta\Delta C_{ant}$ signal and the Subantarctic Mode and Antarctic Intermediate Waters (Fig. 3C), we attribute the decadal differences found in the South Atlantic to increased ventilation rates of these water masses (Patara et al., 2021; DeVries et al., 2017; Shi et al., 2021).

Although the decadal inventory changes in the Indian Ocean and South Pacific are much less robust than those in the Atlantic, they represent in sum a contribution of about 2.6 ± 1.9 Pg C dec^{-1} to the decline of the global inventory. As the negative $\Delta\Delta C_{ant}$ signals in these regions are associated primarily with the location of Antarctic Bottom Water and Lower Circumpolar Deep Waters (Fig. S7), the decadal differences in the C_{ant} storage changes are likely a consequence of circulation changes as well, albeit determined with lower uncertainty than in other regions.

An additional, and globally perhaps more uniform, contribution to the decrease may stem from the observed increase in upper ocean stratification (Sallée et al., 2021). Sallée et al. found that the density contrast across the base of the mixed layer had increased by about 9% per decade between 1970 and 2018. Although their estimate pertains only to the summer, such an increase in stratification is bound to decrease the transport of C_{ant} from the surface to depth, i.e., the most important bottleneck for the uptake of C_{ant} from the atmosphere.

We conclude that in addition to the decrease of the ocean buffer capacity, ocean circulation changes and the increase in stratification are the primary reason for the decrease in the efficiency of the oceanic sink for anthropogenic carbon.

4.2 Comparison with observation-based surface flux estimates: Implications for changes in natural CO_2

In the following, we compare our estimates of the ocean carbon sink to an ensemble of independent observation-based constraints, namely the surface CO_2 flux products assembled by the Global Carbon Budget (Friedlingstein et al., 2022). During the 1994–2004 decade, the ocean interior accumulation of anthropogenic carbon (29.3 ± 2.5 Pg C dec^{-1}) exceeds the time-integrated net air-sea flux of CO_2 of 21.4 ± 2.8 Pg C dec^{-1} (Fig. 8 and Table 2). For this comparison, we adjusted the observation-based air-sea fluxes for a preindustrial steady-state outgassing of riverine CO_2 of 6.1 Pg C dec^{-1} (Jacobson et al., 2007; Resplandy et al., 2018) without considering the uncertainty contribution from this adjustment. We further excluded the estimates provided by Watson et al. (2020) when calculating the ensemble mean and standard deviation of the flux products. Analogous to Gruber et al. (2019), the difference between the ocean interior estimates and the surface fluxes of 7.9 ± 3.8 Pg C dec^{-1} can plausibly be interpreted as a loss of natural carbon from the ocean to the atmosphere (Table 2). Such natural carbon fluxes are captured by the surface flux products, but are not included in the eMLR(C*) based estimates of the accumulation of C_{ant} in the ocean's interior (Clement and Gruber, 2018). The 1σ-uncertainty of this residual term is almost half as large as the signal itself, suggesting that the determined flux is significant, but its magnitude not well constrained. However, postulating a loss of natural carbon for the first decade of our analysis is qualitatively in line with previous studies, which concluded that the stagnation of the ocean carbon sink during the 1990s is due to an anomalously strong outgassing of natural carbon primarily in the Southern Ocean (Landschützer et al., 2015; Lovenduski et al., 2008; Le Quéré et al., 2007).

For the 2004–2014 decade, there is no significant difference between the cumulative surface CO_2 fluxes (26.5 ± 1.3 Pg C dec^{-1}) and our ocean interior ΔC_{ant} inventory (27.3 ± 2.5 Pg C dec^{-1}), suggesting only a minor global net flux of natural CO_2 across the air-sea interface (0.9 ± 2.9 Pg C dec^{-1}). The fact that during the second decade the gain of anthropogenic and the loss of natural carbon weakened simultaneously can plausibly be explained by a weakened

ventilation of the ocean interior, induced by changes in circulation and/or stratification (Sallée et al., 2021), which results in lower upward transport rates of natural carbon to the surface and, vice versa, reduced downward transport of C_{ant} into the ocean interior. This coupling was already hypothesised in previous studies that identified a synchronised reduction of both carbon flux components during periods of a weak upper-ocean overturning circulation (DeVries et al., 2017; Lovenduski et al., 2008). Specifically, DeVries et al. (2017) suggested a more vigorous global overturning in the 1990s that drove an increased outgassing of natural CO_2 and uptake of anthropogenic CO_2, whereas a weaker overturning in the 2000s was found to have the opposite effect. Although the periods of our and their study do not fully overlap, the tendencies toward a weaker anthropogenic carbon uptake agree.

The synchronisation of the uptake of anthropogenic and the outgassing of natural carbon was also observed at a regional scale in the Irminger Sea, where Fröb et al. (2018) detected a sharp increase of the C_{ant} inventory from 2012 to 2015, accompanied by a decline in the natural carbon inventory. This was attributed to a deep convection event during 2015 (Fröb et al., 2016), and underlines that variability at regional scale can superimpose upon the postulated global trend towards a declining anthropogenic carbon uptake.

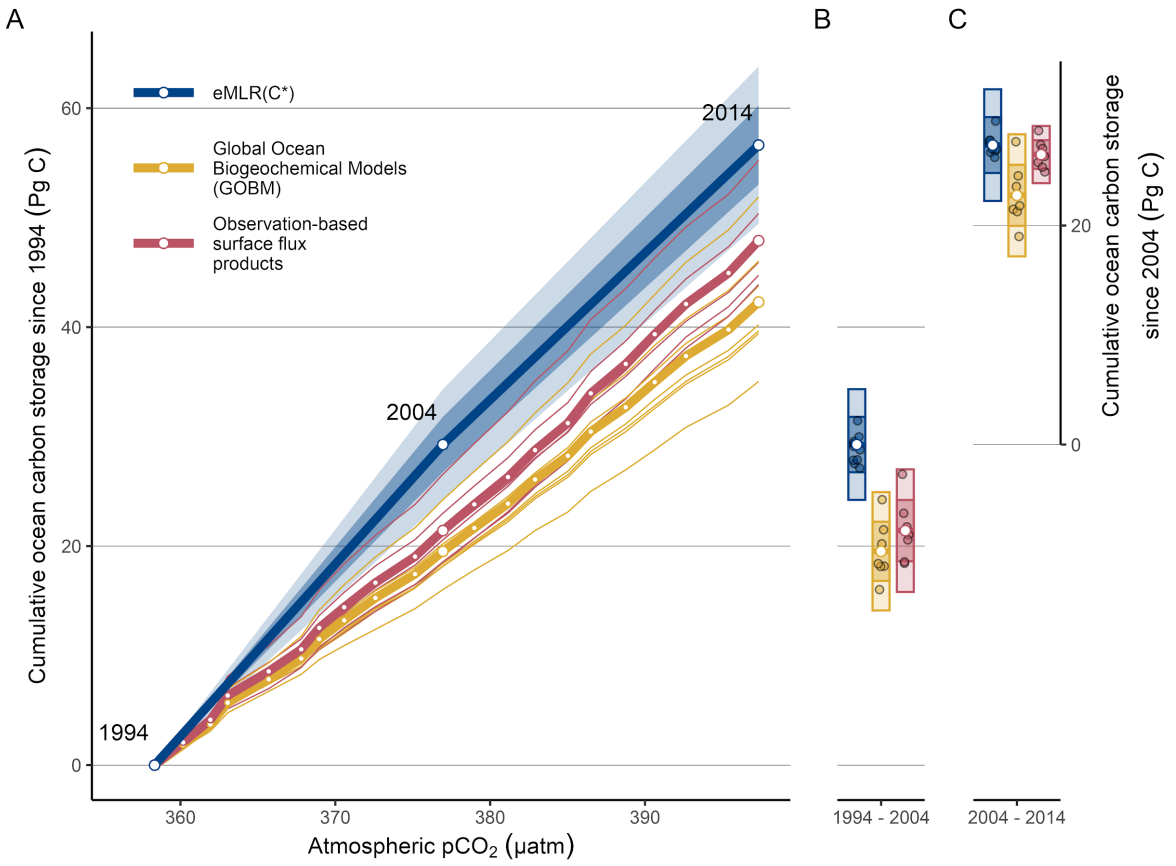

Fig. 8: Ocean carbon storage from 1994 to 2014 according to the eMLR(C*) estimates from this study (blue), in comparison to the cumulative fluxes from surface pCO_2 observation-based air-sea CO_2 flux products (red) and Global Ocean Biogeochemical Models (yellow) from the Global Carbon Budget. The ocean carbon storage is displayed in (A) as a function of atmospheric pCO_2 and in (B and C) as separate temporal integrals across the two decades of our study. All cumulative estimates for the 2004–2014 period in (C) use the eMLR(C*) estimate for 2004 as the zero point. White points represent the ensemble mean for the GCB estimates and the standard case for the eMLR(C*) estimates. Bars in (B and C) indicate 1σ- and 2σ-uncertainty ranges. Note: The eMLR(C*) estimates represent storage changes of anthropogenic carbon only, while the GCB estimates include fluxes of natural and anthropogenic CO_2 (see detailed discussion in the main text).

4.3 Implications for the Global Carbon Budget and climate change

During the first decade of our study (1994–2004), the flux estimates of the GOBMs (19.5 ± 2.7 Pg C dec^{-1}) and the observation-based flux products (21.4 ± 2.8 Pg C dec^{-1}) are significantly lower than the eMLR(C*)-based estimate (29.3 ± 2.5 Pg C dec^{-1}). In the previous section, we proposed climate-driven outgassing of natural CO_2 from the ocean as a plausible explanation for the discrepancy to the surface flux products. The same argument

would apply to the GOBMs, as their flux estimate includes the natural CO_2 flux component. For the 2004–2014 period, the difference between the cumulative observation-based surface fluxes and the ocean interior storage change of C_{ant} disappears, suggesting only a minor global net outgassing of natural CO_2. However, the GOBMs (22.8 ± 2.7 Pg C dec^{-1}, Fig. 8) still diagnose a 17 % weaker ocean carbon sink during the second decade compared to our ocean interior estimates. The most likely explanation for this discrepancy lies in a combination of three challenges that the majority of the current generation of GOBMs are facing: (i) the surface to deep ocean transport of C_{ant} is rather sluggish, as these models tends to underestimate the ventilation rates of the ocean interior (Terhaar et al., 2022; Fu et al., 2022), (ii) the GOBMs reveal a generally lower decadal variability of the CO_2 fluxes compared to observation-based estimates (Hauck et al., 2020), and (iii) the non steady-state fluxes of natural CO_2 (i.e., the fluxes that are caused by climate variability) appear to be low in the GOBMs. For example in the CESM-ETHZ model used in this study, the cumulative flux of natural CO_2 over the 1994–2004 period amounts only to a net uptake of 0.1 Pg C dec^{-1}, and ranges in terms of annual fluxes from an outgassing of 0.2 Pg C yr^{-1} and an uptake of 0.4 Pg C yr^{-1}, which is substantially lower than the observation-based estimate determined in this study.

Considering these three challenges of the GOBMs, the decadal offsets compared to both observation-based estimates (surface and interior) could be explained as follows: During the first decade, the GOBMs simulate a low anthropogenic CO_2 uptake and a low outgassing of natural CO_2. The compensation of these two biases leads to an apparent agreement with the surface-flux and ocean interior estimates. For the second decade, the anthropogenic CO_2 uptake in the GOBMs remains low, but this bias is no longer compensated for by the bias in the outgassing of natural CO_2. While this interpretation of the decadal differences between the three groups of estimates is internally consistent, we emphasise that most of the evaluated offsets are of similar magnitude as their uncertainties. A more bottom-up assessment requires the comparison of the different carbon flux components for the ensemble of GOBMs reported in the GCB, an effort that is currently underway in the framework of phase 2 of the REgional Carbon Cycle Assessment and Processes (RECCAP2) project (Poulter et al., 2022).

To put our ocean carbon sink estimates over the last two decades further into the context of the global carbon cycle, we compare them with the evolution of anthropogenic carbon emissions, as well as with the land and the atmospheric carbon sink extracted from the Global

Carbon Budget 2021 (Friedlingstein et al., 2022) for the same periods (Table 2). From this comparison we derive the airborne, ocean-borne and land-borne fraction of the total emissions (Table 2). Our total emission estimates comprise emissions due to the combustion of fossil fuels (including the cement carbonation sink) and land use change. An important aspect for the contextualisation of our ocean sink estimates is the increase of the total emissions by about 25% from the first to the second decade of our analysis. In contrast, the growth of the atmospheric sink for CO_2 was only about 10% higher during the second decade, which is reflected in a decrease of the airborne fraction from 48 ± 4 % to 44 ± 4 %. Because the emissions grew more rapidly than the atmospheric CO_2, the ocean-borne fraction of C_{ant} (Table 2) decreases even more pronouncedly than the global ocean's uptake efficiency β (Table 1), namely from 36 ± 4 % to 27 ± 4 % for the 1994–2004 and 2004–2014 decade, respectively, which corresponds to a reduction of the uptake fraction of -9 ± 6% (or ~25% in relative terms). In contrast, the land sink evolved very consistently with the total emissions over the two decades, such that the land-borne fraction remained at a stable level (31 ± 6 % and 30 ± 6 %). Due to the identified oceanic outgassing of natural carbon during the first but not the second decade of our analysis, the net ocean sink for anthropogenic and natural carbon increases in a remarkably stable manner with the total emissions. Accordingly, the ocean-borne fraction of the total emissions in terms of the net oceanic CO_2 uptake remained unchanged at a level of 26 ± 4 % and 26 ± 3 %. According to our assessment, the sum of all three sink estimates exceeds the total emissions by about 5% during the 1994–2004 period, whereas the sources and sinks of CO_2 during the 2004–2014 period match almost perfectly.

Although we do not identify a change in the net ocean-borne fraction of the total emissions between 1994 and 2014, it is not for granted that the ocean carbon sink will remain constant for the decades to come (Ridge and McKinley, 2021). DeVries et al. (2017) hypothesised that a trend towards a more stratified ocean is likely to strengthen the CO_2 sink in the near future by trapping natural CO_2 in the deep ocean, but further concluded that this process may ultimately limit the net oceanic carbon sink, when the reduced uptake of anthropogenic CO_2 that continues to accumulate in the atmosphere outweighs the reduced outgassing of natural carbon. Our findings demonstrate that these compensating processes are in progress and we deem it of utmost importance to continue the monitoring of the ocean interior accumulation of carbon to keep track of them.

Table 2: Main sources and sinks of CO_2 for the periods 1994–2004 and 2004–2014 in Pg C dec^{-1}. Estimates of emissions, and the atmospheric, land and net ocean sink are based on the Global Carbon Budget 2021 (Friedlingstein et al., 2022). The net ocean sink estimates represent the cumulative surface fluxes based on surface-pCO_2 observations, adjusted for the outgassing of riverine carbon. The oceanic sink estimates of C_{ant} are from this study, and the oceanic outgassing of natural carbon was determined as the residual between the C_{ant} and the net ocean sink. The uncertainties of the oceanic sink estimates follow the approach of this study, and for all other estimates apply the relative uncertainties for the 2000s according to Table 6 in the GCB. Numbers in parentheses indicate the airborne, land-borne, and ocean-borne fractions in % of the total emissions, with propagated uncertainties from the total emissions and the sink terms.

CO_2 sources sinks	**1994–2004 (Pg C yr^{-1})**	**2004–2014 (Pg C yr^{-1})**
Total emissions	81.8 ± 7.3	100.3 ± 8.9
Fossil emissions	68.3 ± 3.5	88.2 ± 4.6
Land-use change emissions	13.5 ± 7.9	12 ± 7
Atmospheric sink (Airborne fraction)	39.3 ± 0.2 (48 ± 4 %)	44 ± 0.2 (44 ± 4 %)
Land sink (Land-borne fraction)	25 ± 4.8 (31 ± 6 %)	29.8 ± 5.7 (30 ± 6 %)
Ocean sink of C_{ant} (Ocean-borne fraction of C_{ant})	29.3 ± 2.5 (36 ± 4 %)	27.3 ± 2.5 (27 ± 4 %)
Inferred outgassing of natural carbon	7.9 ± 3.8	0.9 ± 2.9
Net ocean sink (Net ocean-borne fraction)	21.4 ± 2.8 (26 ± 4 %)	26.5 ± 1.3 (26 ± 3 %)

4.4 Caveats and Recommendations

Building on the quantitative uncertainty assessment of our ΔC_{ant} reconstructions (section 3.4, supplement S4 and S5), we highlight in the following some caveats of our study and provide recommendations on how to overcome them in future studies.

While all sampling periods assigned for this study are relatively well covered with observations, the large changes we reconstruct in the North Atlantic between the first and second period need to be viewed with caution since the number of data records that provide all required variables for the eMLR(C*) analysis is very limited after ~2015. During this

period, a reinvigoration of the anthropogenic carbon accumulation has been reported in regional studies (Raimondi et al., 2021; Fröb et al., 2018), albeit only for small subregions of the whole North Atlantic. The inclusion of North Atlantic observations collected since 2015 into an eMLR(C*)-based ΔC_{ant} reconstruction will contribute to further improve our understanding of the basin-wide C_{ant} storage changes in this highly dynamic region.

We further expect substantially new and improved insights from the completion of another cycle of the repeat hydrography programme over the 2020s. In contrast to our two decadal ΔC_{ant} reconstructions, which both build on the same data for the central sampling period (2000s) and are thus not fully independent, reconstructing ocean interior trends with yet another decade of observations would resolve this issue. Furthermore, future investigations based on more recent data will profit from the improved data quality, in particular when becoming independent from the observations of the 1990s, which tend to be less consistent than the more recent measurements (Lauvset et al., 2021).

The continued tracking of the oceanic C_{ant} storage, e.g., by providing a global ΔC_{ant} reconstruction for the 2014–2024 period, would also shed light on the very recent divergence of GOBMs and surface-flux products which increased to more than 1 Pg C yr^{-1} in 2020 (Friedlingstein et al., 2022; Hauck et al., 2020). A burning question in this regard is whether the high uptake determined by the surface flux products around 2020 can be confirmed by ocean interior estimates. Scaling our C_{ant} accumulation estimates from the 2004–2014 period to the 2010s according to the atmospheric CO_2 increase, we would indeed project an uptake of ~32 Pg C dec^{-1}, which is very similar to the mean observation-based net surface flux over the same period.

Another recommendation emerges from the high sensitivity of our results to the adjustments we applied to a subset of the observations provided through GLODAPv2.2021. This pronounced sensitivity highlights the importance of data quality and consistency for the ocean interior observing system. Continued efforts to maintain and improve the quality of seawater biogeochemical measurements, such as through the continued use of reference materials and undertaking inter-laboratory comparisons (Bockmon and Dickson, 2015), are indispensable. Furthermore, the timely submission, compilation, and harmonisation of data through GLODAP appears crucial. The release of version 3 of GLODAP including a complete revision of the data adjustments is anticipated in 2024. Based on our findings, we

suggest a critical revision of the observation from the Pacific with a particular focus on the TA measurements.

Tightly linked to the observational data consistency is the accuracy of deep ocean ΔC_{ant} reconstructions. Small biases in ΔC_{ant} can indeed exert a strong impact on the basin inventory changes due to the large volume of the deep ocean. Below 1000 m, the mean ΔC_{ant} reconstructed in this study is lower than 5 µmol kg^{-1} dec^{-1} across all ocean basins (Fig. 4a). Despite the low ΔC_{ant} rates compared to surface waters, the ocean below 1000 m represents a potentially significant contribution to the global C_{ant} inventory as it accounts for roughly 75% of the total ocean volume. On a global average the content and inventory changes between 1000 and 3000 m carry a significant positive signal and contribute about 25% to the total inventory integrated over the top 3000 m. To derive our global inventories, we have chosen to account for the storage change below 3000 m (~30% of the total ocean volume) by scaling the inventory with +2% according to the total C_{ant} accumulation at depth in 1994 (Sabine et al., 2004). This approach is consistent with previous studies (Gruber et al., 2019) and represents a compromise between neglecting deep water storage changes and potentially introducing biases from integrating small and highly uncertain ΔC_{ant} below 3000m. It is important to note that the general decadal trends reported in this study for the regional inventories are maintained when integrating the reconstructed ΔC_{ant} across the full water column, i.e., without the deep ocean scaling (data not shown). Nevertheless, we deem it important that future observation-based studies explicitly include also the accumulation of anthropogenic carbon in the deep ocean below 3000 m water depth, taking advantage, for example, of measurements of transient tracers, such as SF_6 and CFCs.

Finally, our study revealed that fluxes of natural carbon are key to understanding the oceanic response to a changing climate. The comparison of our estimates of the ocean interior accumulation of anthropogenic carbon with the net surface fluxes of CO_2 allowed us to distinguish a decade with presumably strong net outgassing of natural carbon (1994–2004) from a decade with low net fluxes of natural carbon (2004–2014). However, our quantification of the natural carbon flux as a residual quantity between two entirely independent estimates remains prone to uncertainties that are in the same order of magnitude as the flux itself (McNeil and Matear, 2013). As natural carbon fluxes are expected to vary substantially at sub-decadal time scales, a reoccupation of selected repeat hydrography sections with increased frequency or the extension of the BGC Argo programme to global

coverage could provide an important observational basis for future studies. Furthermore, progress in the development of statistical methods to separate storage changes of natural and anthropogenic carbon based on a consistent interpretation of ocean interior observations alone could provide new valuable insight. The application of neural networks to reconstruct ocean interior dynamics of DIC are a meaningful first step in this direction (Keppler et al., 2020; Broullón et al., 2020, 2019).

5 Conclusion and Outlook

This study provides the first global reconstruction of the decadal evolution of the ocean interior storage changes of anthropogenic carbon covering the decades 1994 to 2004 and 2004 to 2014. We provide uncertainty estimates for all reported estimates, including regional inventories and spatial distributions of ΔC_{ant}, and decompose the uncertainties into contributions from various configuration choices associated with the eMLR(C*) method.

We find that the oceanic sink for anthropogenic carbon remained strong during both decades (29 ± 3 PgC dec^{-1} and 27 ± 3 PgC dec^{-1}, respectively). But the sink efficiency and the uptake fraction of anthropogenic emissions weakened from the first to the second decade by about 15 and 25%, respectively. We attribute these changes to a decrease of the ocean buffer capacity and a reduction in the surface ocean to deep transport, induced by changes in ocean circulation (most apparent in the Atlantic) and an increase in upper ocean stratification. In contrast to our findings for the accumulation of C_{ant}, observation-based estimates of the surface fluxes of CO_2 indicate that the net ocean sink for anthropogenic and natural carbon increased proportionally with the anthropogenic emissions. This implies that the net ocean uptake fraction remained stable throughout both decades. We attribute the difference between the anthropogenic and the net carbon sink to an intense (weak) outgassing of natural carbon during the first (second) decades of our analysis.

Our results can serve as new reference points for the annual ocean sink estimates published in the Global Carbon Budget and provide guidance to further develop and assess global ocean biogeochemical models, which most likely underestimate the anthropogenic carbon sink. Furthermore, our reconstructions of the continuing accumulation of C_{ant} can be used to infer acidification trends in the ocean interior at global scale.

Future studies of the ocean interior storage of C_{ant} may allow us to address questions arising from our analysis, including the drivers for the very recent increase in the net uptake flux as determined based on surface pCO_2-observations and the question whether compensating processes of the ocean carbon cycle remain effective, such as the regional shift of the anthropogenic carbon storage from the North to the South Atlantic and the apparent coupling between the fluxes of natural and anthropogenic carbon. Mandatory requirements to address these topics are (i) the continued and extended collection of biogeochemical ocean interior observations, i.e. the completion of a fourth cycle of the repeat hydrography programme and the expansion of the biogeochemical Argo programme to global coverage, (ii) the continued compilation of the observations into a harmonised and quality-controlled data product, and (iii) the continued improvement and further development of statistical methods, for example to separate the storage changes of anthropogenic and natural carbon.

Acknowledgments

The authors thank all colleagues that supported and contributed to the collection and harmonisation of high-quality ocean interior observations made available through GLODAP. JDM and NG acknowledge support from the European Union's Horizon 2020 research and innovation programme under grant agreements no. 821003 (project 4C) and no. 821001 (SO-CHIC). FFP was supported by the BOCATS2 (PID2019-104279GB-C21) project funded by MCIN/AEI/10.13039/501100011033 and contributed to WATER:iOS CSIC PTI. AO and SKL were supported by the project N-ICOS-2 (Research Council of Norway grant no 296012). SKL also acknowledges internal funding support from NORCE. MI was supported by JPMEERF21S20810. RW, RAF, and BC were supported by the Office of Ocean and Atmospheric Research (OAR) of NOAA, including the Global Observation and Monitoring Program (GOMO), FundRef 100018302. BC and RAF contributions are PMEL contribution 5454 and CICOES contribution 2022-1244. TT acknowledges support by EU Horizon 2020 through the EuroSea action (grant agreement 862626).

Open Research

The anthropogenic carbon estimates reconstructed in this study are available through the Research Collection of ETH Zurich under the Creative Commons licence Attribution 4.0 International (CC BY 4.0) via the digital object identifier:
https://doi.org/10.3929/ethz-b-000590910
Upon acceptance of this manuscript for publication, a copy of this data set will be made available through NCEI's Ocean Carbon and Acidification Data System (OCADS), which is accessible under:
https://www.ncei.noaa.gov/products/ocean-carbon-acidification-data-system

All observational data sets underlying our analysis are publicly available.
The merged master file of GLODAPv2.2021 as well as the mapped climatology based on GLODAPv2 were accessed through:
www.glodap.info
The World Ocean Atlas 2018 climatology data and basin masks were accessed through:
https://www.ncei.noaa.gov/products/world-ocean-atlas
The global gridded data set of the surface ocean carbonate system (OceanSODA-ETHZ) is

available under:
https://doi.org/10.25921/m5wx-ja34

For review purposes, the code used to preprocess the data sets, apply the eMLR(C*) method and analyse the generated output is available in these three github repositories:
https://github.com/jens-daniel-mueller/emlr_obs_preprocessing
https://github.com/jens-daniel-mueller/emlr_obs_v_XXX
https://github.com/jens-daniel-mueller/emlr_obs_analysis
The final version of the code will be made available through Zenodo via a digital object identifier upon acceptance of this manuscript for publication

References

Bittig, H. C., Steinhoff, T., Claustre, H., Fiedler, B., Williams, N. L., Sauzède, R., Körtzinger, A., and Gattuso, J.-P.: An Alternative to Static Climatologies: Robust Estimation of Open Ocean CO2 Variables and Nutrient Concentrations From T, S, and O2 Data Using Bayesian Neural Networks, Front. Mar. Sci., 5, https://doi.org/10.3389/fmars.2018.00328, 2018.

Bockmon, E. E. and Dickson, A. G.: An inter-laboratory comparison assessing the quality of seawater carbon dioxide measurements, Mar. Chem., 171, 36–43, https://doi.org/10.1016/j.marchem.2015.02.002, 2015.

Bopp, L., Lévy, M., Resplandy, L., and Sallée, J. B.: Pathways of anthropogenic carbon subduction in the global ocean, Geophys. Res. Lett., 42, 6416–6423, https://doi.org/10.1002/2015GL065073, 2015.

Broullón, D., Pérez, F. F., Velo, A., Hoppema, M., Olsen, A., Takahashi, T., Key, R. M., Tanhua, T., González-Dávila, M., Jeansson, E., Kozyr, A., and van Heuven, S. M. A. C.: A global monthly climatology of total alkalinity: a neural network approach, Earth Syst. Sci. Data, 11, 1109–1127, https://doi.org/10.5194/essd-11-1109-2019, 2019.

Broullón, D., Pérez, F. F., Velo, A., Hoppema, M., Olsen, A., Takahashi, T., Key, R. M., Tanhua, T., Santana-Casiano, J. M., and Kozyr, A.: A global monthly climatology of oceanic total dissolved inorganic carbon: a neural network approach, Earth Syst. Sci. Data, 12, 1725–1743, https://doi.org/10.5194/essd-12-1725-2020, 2020.

Carter, B. R., Feely, R. A., Wanninkhof, R., Kouketsu, S., Sonnerup, R. E., Pardo, P. C., Sabine, C. L., Johnson, G. C., Sloyan, B. M., Murata, A., Mecking, S., Tilbrook, B., Speer, K., Talley, L. D., Millero, F. J., Wijffels, S. E., Macdonald, A. M., Gruber, N., and Bullister, J. L.: Pacific Anthropogenic Carbon Between 1991 and 2017, Glob. Biogeochem. Cycles, 2018GB006154, https://doi.org/10.1029/2018GB006154, 2019.

Cheng, L., Foster, G., Hausfather, Z., Trenberth, K. E., and Abraham, J.: Improved Quantification of the Rate of Ocean Warming, J. Clim., 35, 4827–4840, https://doi.org/10.1175/JCLI-D-21-0895.1, 2022.

Clement, D. and Gruber, N.: The eMLR(C*) Method to Determine Decadal Changes in the Global Ocean Storage of Anthropogenic CO_2, Glob. Biogeochem. Cycles, 32, 654–679, https://doi.org/10.1002/2017GB005819, 2018.

DeVries, T. and Primeau, F.: Dynamically and Observationally Constrained Estimates of Water-Mass Distributions and Ages in the Global Ocean, J. Phys. Oceanogr., 41, 2381–2401, https://doi.org/10.1175/JPO-D-10-05011.1, 2011.

DeVries, T., Holzer, M., and Primeau, F.: Recent increase in oceanic carbon uptake driven by weaker upper-ocean overturning, Nature, 542, 215–218, https://doi.org/10.1038/nature21068, 2017.

Dickson, A. G.: Standard potential of the reaction: AgCl(s) + 12H2(g) = Ag(s) + HCl(aq), and and the standard acidity constant of the ion HSO4− in synthetic sea water from 273.15 to 318.15 K, J. Chem. Thermodyn., 22, 113–127, https://doi.org/10.1016/0021-9614(90)90074-Z, 1990.

Dickson, A. G. and Riley, J. P.: The estimation of acid dissociation constants in seawater media from potentionmetric titrations with strong base. I. The ionic product of water — Kw, Mar. Chem., 7, 89–99, https://doi.org/10.1016/0304-4203(79)90001-X, 1979.

Doney, S. C., Lima, I., Feely, R. A., Glover, D. M., Lindsay, K., Mahowald, N., Moore, J. K., and Wanninkhof, R.: Mechanisms governing interannual variability in upper-ocean inorganic carbon system and air–sea CO2 fluxes: Physical climate and atmospheric dust, Deep Sea Res. Part II Top. Stud. Oceanogr., 56, 640–655, https://doi.org/10.1016/j.dsr2.2008.12.006, 2009.

Fay, A. R., Gregor, L., Landschützer, P., McKinley, G. A., Gruber, N., Gehlen, M., Iida, Y., Laruelle, G. G., Rödenbeck, C., Roobaert, A., and Zeng, J.: SeaFlux: harmonization of air–sea CO_2 fluxes from surface pCO_2 data products using a standardized approach, Earth Syst. Sci. Data, 13, 4693–4710, https://doi.org/10.5194/essd-13-4693-2021, 2021.

Friedlingstein, P., Jones, M. W., O'Sullivan, M., Andrew, R. M., Bakker, D. C. E., Hauck, J., Le Quéré, C., Peters, G. P., Peters, W., Pongratz, J., Sitch, S., Canadell, J. G., Ciais, P., Jackson, R. B., Alin, S. R., Anthoni, P., Bates, N. R., Becker, M., Bellouin, N., Bopp, L., Chau, T. T. T., Chevallier, F., Chini, L. P., Cronin, M., Currie, K. I., Decharme, B., Djeutchouang, L. M., Dou, X., Evans, W., Feely, R. A., Feng, L., Gasser, T., Gilfillan, D., Gkritzalis, T., Grassi, G., Gregor, L., Gruber, N., Gürses, Ö., Harris, I., Houghton, R. A., Hurtt, G. C., Iida, Y., Ilyina, T., Luijkx, I. T., Jain, A., Jones, S. D., Kato, E., Kennedy, D., Klein Goldewijk, K., Knauer, J., Korsbakken, J. I., Körtzinger, A., Landschützer, P., Lauvset, S. K., Lefèvre, N., Lienert, S., Liu, J., Marland, G., McGuire, P. C., Melton, J. R., Munro, D. R., Nabel, J. E. M. S., Nakaoka, S.-I., Niwa, Y., Ono, T., Pierrot, D., Poulter, B., Rehder, G., Resplandy, L., Robertson, E., Rödenbeck, C., Rosan, T. M., Schwinger, J., Schwingshackl, C., Séférian, R., Sutton, A. J., Sweeney, C., Tanhua, T., Tans, P. P., Tian, H., Tilbrook, B., Tubiello, F., van der Werf, G. R., Vuichard, N., Wada, C., Wanninkhof, R., Watson, A. J., Willis, D., Wiltshire, A. J., Yuan, W., Yue, C., Yue, X., Zaehle, S., and Zeng, J.: Global Carbon Budget 2021, Earth Syst. Sci. Data, 14, 1917–2005, https://doi.org/10.5194/essd-14-1917-2022, 2022.

Fröb, F., Olsen, A., Våge, K., Moore, G. W. K., Yashayaev, I., Jeansson, E., and Rajasakaren, B.: Irminger Sea deep convection injects oxygen and anthropogenic carbon to the ocean interior, Nat. Commun., 7, 13244, https://doi.org/10.1038/ncomms13244, 2016.

Fröb, F., Olsen, A., Pérez, F. F., García-Ibáñez, M. I., Jeansson, E., Omar, A., and Lauvset, S. K.: Inorganic carbon and water masses in the Irminger Sea since 1991, Biogeosciences, 15, 51–72, https://doi.org/10.5194/bg-15-51-2018, 2018.

Fu, W., Moore, J. K., Primeau, F., Collier, N., Ogunro, O. O., Hoffman, F. M., and Randerson, J. T.: Evaluation of ocean biogeochemistry and carbon cycling in CMIP earth system models with the International Ocean Model Benchmarking (IOMB) software system, J. Geophys. Res. Oceans, n/a, e2022JC018965, https://doi.org/10.1029/2022JC018965, 2022.

Gammon, R. H., Cline, J., and Wisegarver, D.: Chlorofluoromethanes in the northeast Pacific Ocean: Measured vertical distributions and application as transient tracers of upper ocean mixing, J. Geophys. Res. Oceans, 87, 9441–9454, https://doi.org/10.1029/JC087iC12p09441, 1982.

Gao, H., Cai, W.-J., Jin, M., Dong, C., and Timmerman, A. H. V.: Ocean Ventilation Controls the Contrasting Anthropogenic CO2 Uptake Rates Between the Western and Eastern South Atlantic Ocean Basins, Glob. Biogeochem. Cycles, 36, e2021GB007265, https://doi.org/10.1029/2021GB007265, 2022.

Gattuso, J.-P., Epitalon, J.-M., Lavigne, H., and Orr, J.: seacarb: Seawater Carbonate Chemistry, 2021.

Graham, F. S. and McDougall, T. J.: Quantifying the Nonconservative Production of Conservative Temperature, Potential Temperature, and Entropy, J. Phys. Oceanogr., 43, 838–862, https://doi.org/10.1175/JPO-D-11-0188.1, 2013.

Gregor, L. and Gruber, N.: OceanSODA-ETHZ: a global gridded data set of the surface ocean carbonate system for seasonal to decadal studies of ocean acidification, Earth Syst. Sci. Data, 13, 777–808, https://doi.org/10.5194/essd-13-777-2021, 2021.

Gruber, N., Sarmiento, J. L., and Stocker, T. F.: An improved method for detecting anthropogenic CO2 in the oceans, Glob. Biogeochem. Cycles, 10, 809–837, https://doi.org/10.1029/96GB01608, 1996.

Gruber, N., Clement, D., Carter, B. R., Feely, R. A., van Heuven, S., Hoppema, M., Ishii, M., Key, R. M., Kozyr, A., Lauvset, S. K., Lo Monaco, C., Mathis, J. T., Murata, A., Olsen, A., Perez, F. F., Sabine, C. L., Tanhua, T., and Wanninkhof, R.: The oceanic sink for anthropogenic CO2 from 1994 to 2007, Science, 363, 1193–1199, https://doi.org/10.1126/science.aau5153, 2019.

Hauck, J., Zeising, M., Le Quéré, C., Gruber, N., Bakker, D. C. E., Bopp, L., Chau, T. T. T., Gürses, Ö., Ilyina, T., Landschützer, P., Lenton, A., Resplandy, L., Rödenbeck, C., Schwinger, J., and Séférian, R.: Consistency and Challenges in the Ocean Carbon Sink Estimate for the Global Carbon Budget, Front. Mar. Sci., 7, https://doi.org/10.3389/fmars.2020.571720, 2020.

Holliday, N. P., Bersch, M., Berx, B., Chafik, L., Cunningham, S., Florindo-López, C., Hátún, H., Johns, W., Josey, S. A., Larsen, K. M. H., Mulet, S., Oltmanns, M., Reverdin, G., Rossby, T., Thierry, V., Valdimarsson, H., and Yashayaev, I.: Ocean circulation causes the largest freshening event for 120 years in eastern subpolar North Atlantic, Nat. Commun., 11, 585, https://doi.org/10.1038/s41467-020-14474-y, 2020.

IPCC: IPCC Special Report on the Ocean and Cryosphere in a Changing Climate [H.-O. Pörtner, D.C. Roberts, V. Masson-Delmotte, P. Zhai, M. Tignor, E. Poloczanska, K. Mintenbeck, A. Alegría, M. Nicolai, A. Okem, J. Petzold, B. Rama, N.M. Weyer (eds.)], Cambridge University Press, https://doi.org/10.1017/9781009157964, 2019.

Jackson, L. C., Dubois, C., Forget, G., Haines, K., Harrison, M., Iovino, D., Köhl, A., Mignac, D., Masina, S., Peterson, K. A., Piecuch, C. G., Roberts, C. D., Robson, J., Storto, A., Toyoda, T., Valdivieso, M., Wilson, C., Wang, Y., and Zuo, H.: The Mean State and Variability of the North Atlantic Circulation: A Perspective From Ocean Reanalyses, J. Geophys. Res. Oceans, 124, 9141–9170, https://doi.org/10.1029/2019JC015210, 2019.

Jackson, L. C., Biastoch, A., Buckley, M. W., Desbruyères, D. G., Frajka-Williams, E., Moat, B., and Robson, J.: The evolution of the North Atlantic Meridional Overturning Circulation since 1980, Nat. Rev. Earth Environ., 1–14, https://doi.org/10.1038/s43017-022-00263-2, 2022.

Jacobson, A. R., Fletcher, S. E. M., Gruber, N., Sarmiento, J. L., and Gloor, M.: A joint atmosphere-ocean inversion for surface fluxes of carbon dioxide: 2. Regional results, Glob. Biogeochem. Cycles, 21, https://doi.org/10.1029/2006GB002703, 2007.

Jiang, L.-Q., Carter, B. R., Feely, R. A., Lauvset, S. K., and Olsen, A.: Surface ocean pH and buffer capacity: past, present and future, Sci. Rep., 9, 18624, https://doi.org/10.1038/s41598-019-55039-4, 2019.

Keppler, L., Landschützer, P., Gruber, N., Lauvset, S. K., and Stemmler, I.: Seasonal Carbon Dynamics in the Near-Global Ocean, Glob. Biogeochem. Cycles, 34, e2020GB006571, https://doi.org/10.1029/2020GB006571, 2020.

Key, R. M., Kozyr, A., Sabine, C. L., Lee, K., Wanninkhof, R., Bullister, J. L., Feely, R. A., Millero, F. J., Mordy, C., and Peng, T.-H.: A global ocean carbon climatology: Results from Global Data Analysis Project (GLODAP), Glob. Biogeochem. Cycles, 18, https://doi.org/10.1029/2004GB002247, 2004.

Khatiwala, S., Primeau, F., and Hall, T.: Reconstruction of the history of anthropogenic CO 2 concentrations in the ocean, Nature, 462, 346–349, https://doi.org/10.1038/nature08526, 2009.

Khatiwala, S., Tanhua, T., Mikaloff Fletcher, S., Gerber, M., Doney, S. C., Graven, H. D., Gruber, N., McKinley, G. A., Murata, A., Ríos, A. F., and Sabine, C. L.: Global ocean storage of anthropogenic carbon, Biogeosciences, 10, 2169–2191, https://doi.org/10.5194/bg-10-2169-2013, 2013.

Landschützer, P., Gruber, N., Haumann, F. A., Rödenbeck, C., Bakker, D. C. E., van Heuven, S., Hoppema, M., Metzl, N., Sweeney, C., Takahashi, T., Tilbrook, B., and Wanninkhof, R.: The reinvigoration of the Southern Ocean carbon sink, Science, 349, 1221–1224, https://doi.org/10.1126/science.aab2620, 2015.

Landschützer, P., Gruber, N., and Bakker, D. C. E.: Decadal variations and trends of the global ocean carbon sink, Glob. Biogeochem. Cycles, 30, 1396–1417, https://doi.org/10.1002/2015GB005359, 2016.

Latif, M., Sun, J., Visbeck, M., and Hadi Bordbar, M.: Natural variability has dominated Atlantic Meridional Overturning Circulation since 1900, Nat. Clim. Change, 1–6, https://doi.org/10.1038/s41558-022-01342-4, 2022.

Lauvset, S. K., Key, R. M., Olsen, A., van Heuven, S., Velo, A., Lin, X., Schirnick, C., Kozyr, A., Tanhua, T., Hoppema, M., Jutterström, S., Steinfeldt, R., Jeansson, E., Ishii, M., Perez, F. F., Suzuki, T., and Watelet, S.: A new global interior ocean mapped climatology: the 1◦ × 1◦ GLODAP version 2, 16, 2016.

Lauvset, S. K., Lange, N., Tanhua, T., Bittig, H. C., Olsen, A., Kozyr, A., Álvarez, M., Becker, S., Brown, P. J., Carter, B. R., Cotrim da Cunha, L., Feely, R. A., van Heuven, S., Hoppema, M., Ishii, M., Jeansson, E., Jutterström, S., Jones, S. D., Karlsen, M. K., Lo Monaco, C., Michaelis, P., Murata, A., Pérez, F. F., Pfeil, B., Schirnick, C., Steinfeldt, R., Suzuki, T., Tilbrook, B., Velo, A., Wanninkhof, R., Woosley, R. J., and Key, R. M.: An updated version of the global interior ocean biogeochemical data product, GLODAPv2.2021, Earth Syst. Sci. Data, 13, 5565–5589, https://doi.org/10.5194/essd-13-5565-2021, 2021.

Lauvset, S. K., Lange, N., Tanhua, T., Bittig, H. C., Olsen, A., Kozyr, A., Alin, S., Álvarez, M., Azetsu-Scott, K., Barbero, L., Becker, S., Brown, P. J., Carter, B. R., da Cunha, L. C., Feely, R. A., Hoppema, M., Humphreys, M. P., Ishii, M., Jeansson, E., Jiang, L.-Q., Jones, S. D., Lo Monaco, C., Murata, A., Müller, J. D., Pérez, F. F., Pfeil, B., Schirnick, C., Steinfeldt, R., Suzuki, T., Tilbrook, B., Ulfsbo, A., Velo, A., Woosley, R.

J., and Key, R. M.: GLODAPv2.2022: the latest version of the global interior ocean biogeochemical data product, Earth Syst. Sci. Data, 14, 5543–5572, https://doi.org/10.5194/essd-14-5543-2022, 2022.

Le Quéré, C., Rödenbeck, C., Buitenhuis, E. T., Conway, T. J., Langenfelds, R., Gomez, A., Labuschagne, C., Ramonet, M., Nakazawa, T., Metzl, N., Gillett, N., and Heimann, M.: Saturation of the Southern Ocean CO2 Sink Due to Recent Climate Change, Science, 316, 1735–1738, https://doi.org/10.1126/science.1136188, 2007.

Li, G., Cheng, L., Zhu, J., Trenberth, K. E., Mann, M. E., and Abraham, J. P.: Increasing ocean stratification over the past half-century, Nat. Clim. Change, 1–8, https://doi.org/10.1038/s41558-020-00918-2, 2020.

Locarnini, R., Mishonov, A., Baranova, O., Boyer, T., Zweng, M., Garcia, H., Reagan, J., Seidov, D., Weathers, K., Paver, C., Smolyar, I., and Locarnini, R.: World Ocean Atlas 2018, Volume 1: Temperature, 2019.

Lovenduski, N. S., Gruber, N., and Doney, S. C.: Toward a mechanistic understanding of the decadal trends in the Southern Ocean carbon sink, Glob. Biogeochem. Cycles, 22, https://doi.org/10.1029/2007GB003139, 2008.

Lueker, T. J., Dickson, A. G., and Keeling, C. D.: Ocean pCO2 calculated from dissolved inorganic carbon, alkalinity, and equations for K1 and K2: validation based on laboratory measurements of CO2 in gas and seawater at equilibrium, Mar. Chem., 70, 105–119, https://doi.org/10.1016/S0304-4203(00)00022-0, 2000.

McNeil, B. I. and Matear, R. J.: The non-steady state oceanic CO_2 signal: its importance, magnitude and a novel way to detect it, Biogeosciences, 10, 2219–2228, https://doi.org/10.5194/bg-10-2219-2013, 2013.

McNeil, B. I., Matear, R. J., Key, R. M., Bullister, J. L., and Sarmiento, J. L.: Anthropogenic CO2 Uptake by the Ocean Based on the Global Chlorofluorocarbon Data Set, Science, 299, 235–239, https://doi.org/10.1126/science.1077429, 2003.

Olsen, A., Omar, A. M., Jeansson, E., Anderson, L. G., and Bellerby, R. G. J.: Nordic seas transit time distributions and anthropogenic CO2, J. Geophys. Res. Oceans, 115, https://doi.org/10.1029/2009JC005488, 2010.

Olsen, A., Key, R. M., van Heuven, S., Lauvset, S. K., Velo, A., Lin, X., Schirnick, C., Kozyr, A., Tanhua, T., Hoppema, M., Jutterström, S., Steinfeldt, R., Jeansson, E., Ishii, M., Pérez, F. F., and Suzuki, T.: The Global Ocean Data Analysis Project version 2 (GLODAPv2) – an internallyconsistent data product for the world ocean, Earth Syst. Sci. Data, 8, 297–323, https://doi.org/10.5194/essd-8-297-2016, 2016.

Palmiéri, J., Orr, J. C., Dutay, J.-C., Béranger, K., Schneider, A., Beuvier, J., and Somot, S.: Simulated anthropogenic CO_2 storage and acidification of the Mediterranean Sea, Biogeosciences, 12, 781–802, https://doi.org/10.5194/bg-12-781-2015, 2015.

Park, G.-H., Lee, K., Tishchenko, P., Min, D.-H., Warner, M. J., Talley, L. D., Kang, D.-J., and Kim, K.-R.: Large accumulation of anthropogenic CO2 in the East (Japan) Sea and its significant impact on carbonate chemistry, Glob. Biogeochem. Cycles, 20, https://doi.org/10.1029/2005GB002676, 2006.

Patara, L., Böning, C. W., and Tanhua, T.: Multidecadal Changes in Southern Ocean Ventilation since the 1960s Driven by Wind and Buoyancy Forcing, J. Clim., 34, 1485–1502, https://doi.org/10.1175/JCLI-D-19-0947.1, 2021.

Perez, F. F. and Fraga, F.: Association constant of fluoride and hydrogen ions in seawater, Mar. Chem., 21, 161–168, https://doi.org/10.1016/0304-4203(87)90036-3, 1987.

Pérez, F. F., Vázquez-Rodríguez, M., Mercier, H., Velo, A., Lherminier, P., and Ríos, A. F.: Trends of anthropogenic CO_2 storage in North Atlantic water masses, Biogeosciences, 7, 1789–1807, https://doi.org/10.5194/bg-7-1789-2010, 2010.

Pérez, F. F., Mercier, H., Vázquez-Rodríguez, M., Lherminier, P., Velo, A., Pardo, P. C., Rosón, G., and Ríos, A. F.: Atlantic Ocean CO2 uptake reduced by weakening of the meridional overturning circulation, Nat. Geosci., 6, 146–152, https://doi.org/10.1038/ngeo1680, 2013.

Poulter, B., Bastos, A., Canadell, J., Ciais, P., Gruber, N., Hauck, J., Jackson, R., Ishii, M., Müller, Jens Daniel, J., Patra, P., and Tian, H.: Inventorying Earth's Land and Ocean Greenhouse Gases, Eos, 103, https://doi.org/10.1029/2022eo179084, 2022.

Raimondi, L., Tanhua, T., Azetsu-Scott, K., Yashayaev, I., and Wallace, D. w. r.: A 30 -Year Time Series of Transient Tracer-Based Estimates of Anthropogenic Carbon in the Central Labrador Sea, J. Geophys. Res. Oceans, 126, e2020JC017092, https://doi.org/10.1029/2020JC017092, 2021.

Resplandy, L., Keeling, R. F., Rödenbeck, C., Stephens, B. B., Khatiwala, S., Rodgers, K. B., Long, M. C., Bopp, L., and Tans, P. P.: Revision of global carbon fluxes based on a reassessment of oceanic and riverine carbon transport, Nat. Geosci., 11, 504–509, https://doi.org/10.1038/s41561-018-0151-3, 2018.

Ridge, S. M. and McKinley, G. A.: Ocean carbon uptake under aggressive emission mitigation, Biogeosciences, 18, 2711–2725, https://doi.org/10.5194/bg-18-2711-2021, 2021.

Sabine, C. L., Feely, R. A., Gruber, N., Key, R. M., Lee, K., Bullister, J. L., Wanninkhof, R., Wong, C. S., Wallace, D. W. R., Tilbrook, B., Millero, F. J., Peng, T.-H., Kozyr, A., Ono, T., and Rios, A. F.: The Oceanic Sink for Anthropogenic CO2, Science, 305, 367–371, https://doi.org/10.1126/science.1097403, 2004.

Sallée, J.-B., Pellichero, V., Akhoudas, C., Pauthenet, E., Vignes, L., Schmidtko, S., Garabato, A. N., Sutherland, P., and Kuusela, M.: Summertime increases in upper-ocean stratification and mixed-layer depth, Nature, 591, 592–598, https://doi.org/10.1038/s41586-021-03303-x, 2021.

Shi, J.-R., Talley, L. D., Xie, S.-P., Peng, Q., and Liu, W.: Ocean warming and accelerating Southern Ocean zonal flow, Nat. Clim. Change, 1–8, https://doi.org/10.1038/s41558-021-01212-5, 2021.

Sloyan, B. M., Wanninkhof, R., Kramp, M., Johnson, G. C., Talley, L. D., Tanhua, T., McDonagh, E., Cusack, C., O'Rourke, E., McGovern, E., Katsumata, K., Diggs, S., Hummon, J., Ishii, M., Azetsu-Scott, K., Boss, E., Ansorge, I., Perez, F. F., Mercier, H., Williams, M. J. M., Anderson, L., Lee, J. H., Murata, A., Kouketsu, S., Jeansson, E., Hoppema, M., and Campos, E.: The Global Ocean Ship-Based Hydrographic Investigations Program (GO-SHIP): A Platform for Integrated Multidisciplinary Ocean Science, Front. Mar. Sci., 6, https://doi.org/10.3389/fmars.2019.00445, 2019.

Talley, L. d., Feely, R. a., Sloyan, B. m., Wanninkhof, R., Baringer, M. o., Bullister, J. l., Carlson, C. a., Doney, S. c., Fine, R. a., Firing, E., Gruber, N., Hansell, D. a., Ishii, M., Johnson, G. c., Katsumata, K., Key, R. m., Kramp, M., Langdon, C., Macdonald, A. m., Mathis, J. t., McDonagh, E. l., Mecking, S., Millero, F. j., Mordy, C. w., Nakano, T., Sabine, C. l., Smethie, W. m., Swift, J. h., Tanhua, T., Thurnherr, A. m., Warner, M. j., and Zhang, J.-Z.: Changes in Ocean Heat, Carbon Content, and Ventilation: A Review of the First Decade of GO-SHIP Global Repeat Hydrography, Annu. Rev. Mar. Sci., 8, 185–215, https://doi.org/10.1146/annurev-marine-052915-100829, 2016.

Tanhua, T., Jones, E. P., Jeansson, E., Jutterström, S., Smethie, W. M., Wallace, D. W. R., and Anderson, L. G.: Ventilation of the Arctic Ocean: Mean ages and inventories of anthropogenic CO2 and CFC-11, J. Geophys. Res. Oceans, 114, https://doi.org/10.1029/2008JC004868, 2009.

Terhaar, J., Frölicher, T. L., and Joos, F.: Observation-constrained estimates of the global ocean carbon sink from Earth system models, Biogeosciences, 19, 4431–4457, https://doi.org/10.5194/bg-19-4431-2022, 2022.

Wallace, D. W. R.: Monitoring Global Ocean Carbon Inventories, 1995.

Wanninkhof, R., Doney, S. C., Bullister, J. L., Levine, N. M., Warner, M., and Gruber, N.: Detecting anthropogenic CO2 changes in the interior Atlantic Ocean between 1989 and 2005, J. Geophys. Res. Oceans, 115, https://doi.org/10.1029/2010JC006251, 2010.

Watson, A. J., Schuster, U., Shutler, J. D., Holding, T., Ashton, I. G. C., Landschützer, P., Woolf, D. K., and Goddijn-Murphy, L.: Revised estimates of ocean-atmosphere CO2 flux are consistent with ocean carbon inventory, Nat. Commun., 11, 4422, https://doi.org/10.1038/s41467-020-18203-3, 2020.

Weiss, R. F.: The solubility of nitrogen, oxygen and argon in water and seawater, Deep Sea Res. Oceanogr. Abstr., 17, 721–735, https://doi.org/10.1016/0011-7471(70)90037-9, 1970.

Woosley, R. J., Millero, F. J., and Wanninkhof, R.: Rapid anthropogenic changes in CO2 and pH in the Atlantic Ocean: 2003–2014, Glob. Biogeochem. Cycles, 30, 70–90, https://doi.org/10.1002/2015GB005248, 2016.

Young, I. R. and Ribal, A.: Multiplatform evaluation of global trends in wind speed and wave height, Science, 364, 548–552, https://doi.org/10.1126/science.aav9527, 2019.

Zweng, M. M., Reagan, J., Seidov, D., Boyer, T., Locarnini, R., Garcia, H., Mishonov, A., Baranova, O. K., Paver, C., and Smolyar, I.: WORLD OCEAN ATLAS 2018 Volume 2: Salinity, 2019.

AGU Advances

Supporting Information for

Decadal Trends in the Oceanic Storage of Anthropogenic Carbon from 1994 to 2014

Jens Daniel Müller[1], N. Gruber[1], B. Carter[2,3], R. Feely[3], M. Ishii[4], N. Lange[5], S.K. Lauvset[6], A. Murata[7], A. Olsen[8], F.F. Pérez[9,10], C. Sabine[12], T. Tanhua[5], R. Wanninkhof[13], D. Zhu[1]

[1]Environmental Physics, Institute of Biogeochemistry and Pollutant Dynamics, ETH Zurich, Zurich, Switzerland.
[2]Cooperative Institute for Climate, Ocean, and Ecosystem Studies, University of Washington, Seattle, WA, 98105.
[3]Pacific Marine Environmental Laboratory, National Oceanic and Atmospheric Administration, Seattle, WA, 98115.
[4]Meteorological Research Institute, Japan Meteorological Agency, Tsukuba, Japan.
[5]GEOMAR Helmholtz Centre for Ocean Research Kiel, Kiel, Germany.
[6]NORCE Norwegian Research Centre, Bjerknes Centre for Climate Research, Bergen, Norway.
[7]Japan Agency for Marine-Earth Science and Technology, Yokosuka, Kanagawa, 237-0061, Japan.
[8]Geophysical Institute, University of Bergen and Bjerknes Centre for Climate Research, Bergen, Norway.
[9]Instituto de Investigaciones Marinas (IIM), CSIC, Vigo, Spain.
[10]Oceans Department, Stanford University, Stanford, CA 94305, USA.
[12]University of Hawaii at Manoa, Honolulu, HI, 96822.
[13]Atlantic Oceanographic and Meteorological Laboratory, National Oceanographic and Atmospheric Administration, Miami, USA.

Contents of this file

Introduction

In this supplement we provide supporting information about the observational data base underlying our results (S1), with a particular focus on adjustments that we applied to improve the data consistency (S1.2). We provide information about the exact configuration of our statistical method, discussing also aspects of the configuration that we tested during this study, but that revealed to be of secondary relevance (S2). We provide additional observation-based results to extend the information given in the main text (S3). In section S4, a detailed description of our uncertainty and sensitivity assessment is given, including also a decomposition of the uncertainty into its components. We extend this uncertainty assessment in section S5 through reporting the results of our tests of the eMLR(C*) method with synthetic data from a Global Ocean Biogeochemical Model (GOBM). Finally, we provide a detailed comparison of our results to those obtained from previous regional studies (S6).

S1 Observational data base

S1.1 Basin mask for regional clustering

Based on the basin mask provided by the World Ocean Atlas 2018 (Garcia et al., 2019), we derived six different definitions (Fig. S1) of the main ocean basins that we used to cluster the data in the horizontal dimensions for the eMLR(C*) analysis.

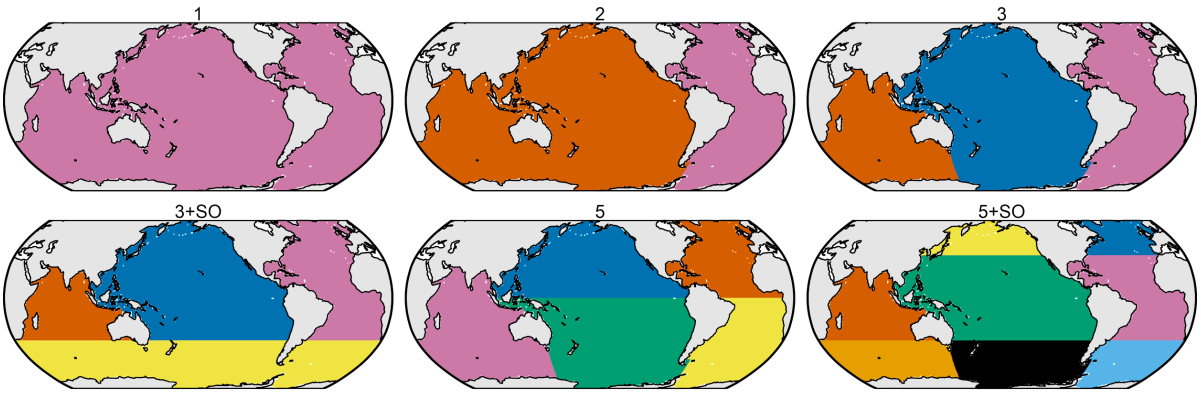

Fig. S1: The six basin mask definitions used to cluster observations for the fitting of MLR models and the subsequent mapping of ΔC_{ant}. Basin mask "3" was used for our standard case reconstructions of ΔC_{ant}. Basin mask "5" was also used to integrate ΔC_{ant} inventories for individual ocean basins.

S1.2 Data adjustments for the Indian Ocean and North Pacific

A prerequisite for the accurate reconstruction of ΔC_{ant} is the consistency of the underlying measurements. In this regard, the eMRL(C*) method profits from the incorporation of all available cruise data from one sampling period in a single model fitting step, which reduces the sensitivity to measurement biases, which are often attributed to different instrumental set-ups, procedures or staff on individual cruises. Furthermore, GLODAP performs a comprehensive data quality assessment and reduces remaining biases when compiling observations into a harmonised database. This is achieved through data adjustments based on crossover comparisons of deep water measurements. The ambitious aim of GLODAP is to provide an overall consistent data set comprising observations collected over more than five decades (Lauvset et al., 2021; Olsen et al., 2016).

Despite these efforts, applying the eMLR(C*) method to observations as published in GLODAPv2.2021, leads to an evenly distributed ΔC_{ant} signal below 1500m that is in the order of +3 µmol kg^{-1} in the Indian Ocean for the 1994–2004 period and in the order of +2 µmol kg^{-1} in the North Pacific Ocean for the 2004–2014 period (Fig. S2). This deep water ΔC_{ant} accumulation causes substantially (regionally up to 10 mol m^{-2} dec^{-1}) elevated column inventory changes in the two hemispheric basins (Fig. S11). Such a strong accumulation of ΔC_{ant} in the deep waters of these basins cannot be reasonably explained based on oceanographic knowledge and is further in disagreement with the close-to-zero levels of pCFC-12 (Key et al., 2004) and total C_{ant} (Sabine et al., 2004) estimated for these water masses in 1994. Likewise, we do not find a similar deep water ΔC_{ant} increase in the respective other decade, i.e. the 2004–2014 period for the Indian and the 1994–2004 period

for the Pacific Ocean. Extensive configuration changes and tests of the eMLR(C*) method (including the separate analysis of 20° latitude or longitude bands, the removal of individual predictors, the use of DIC as target variable, and using reoccupied cruises only) indicate that the elevated deep water ΔC_{ant} signal in these two regions is not causes by a methodological artefact.

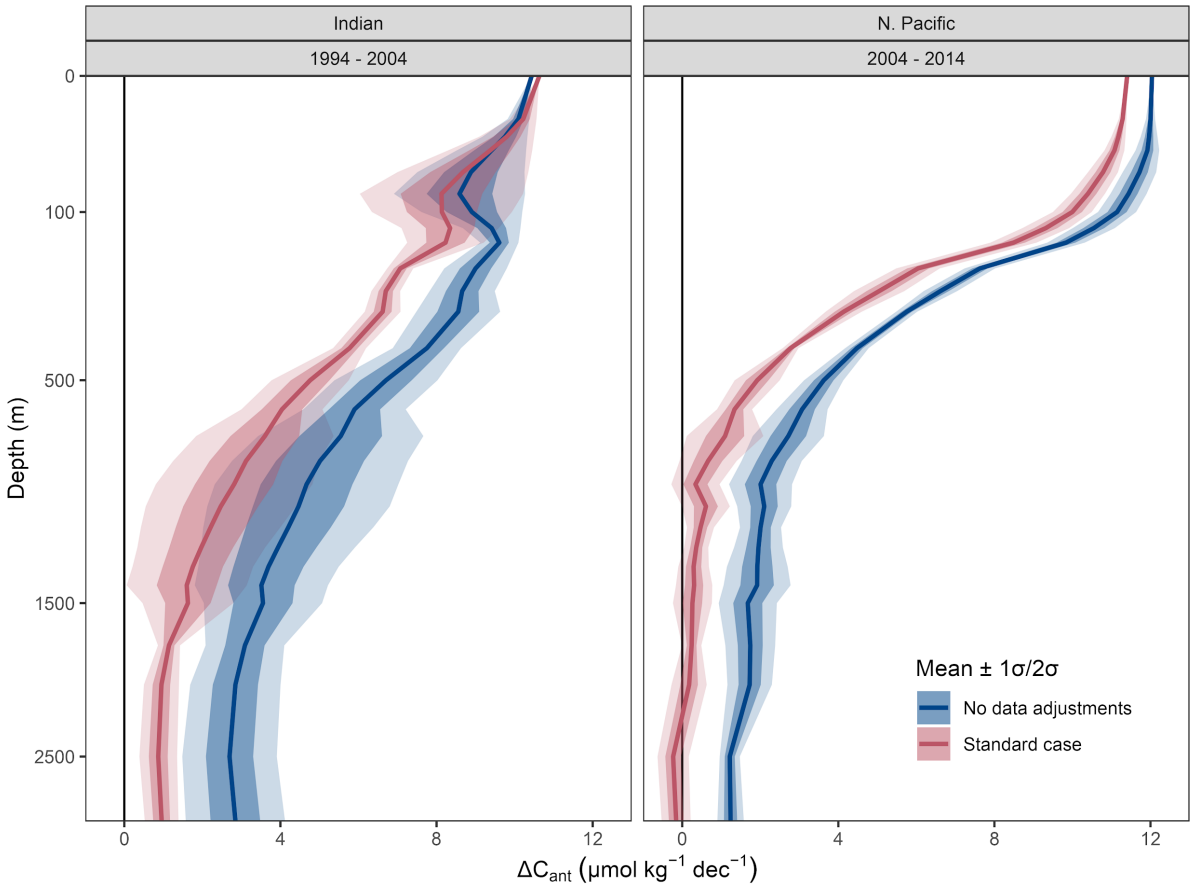

Fig. S2: ΔC_{ant} profiles determined with the eMLR(C*) method applied to adjusted (blue) and unadjusted (red) data, for 1994–2004 in the Indian Ocean (left) and for 2004–2014 in the North Pacific (right). The solid lines refer to the reconstructions based on the standard basin clustering scheme "3", while the ribbons indicate 1 and 2 standard deviations across the reconstructions of all 6 basin clustering options displayed in Fig. S1.

In contrast, several lines of arguments suggest a bias in the underlying observations. An evaluation of the GLODAP crossover results (Olsen et al., 2016 and subsequent GLODAP updates) revealed remaining mean decade-to-decade offsets expressed in C* units in the adjusted GLODAP products of around +5 μmol kg^{-1} when comparing the RV Knorr Indian Ocean cruises from the 2000s and the 1990s, and of around +3 μmol kg^{-1} when comparing all North Pacific Ocean cruises from the 2010s and the 2000s (Fig. S3). The offsets in C* units represent the sum of the content offsets in DIC, TA and phosphate, the last of which was approximated as the product of the factorial phosphate offset and the mean deep water phosphate content of the respective basin. Only in the two affected ocean basins (Indian Ocean 2000s vs 1990s and North Pacific 2010s vs 2000s), the absolute mean C* offset between the decades exceeds the standard deviation of the individual mean cruise offsets, indicating a robustness of the offset. Only in these basins and decades, we investigated the

crossover offsets of the three underlying variables DIC, TA and phosphate to determine data adjustments.

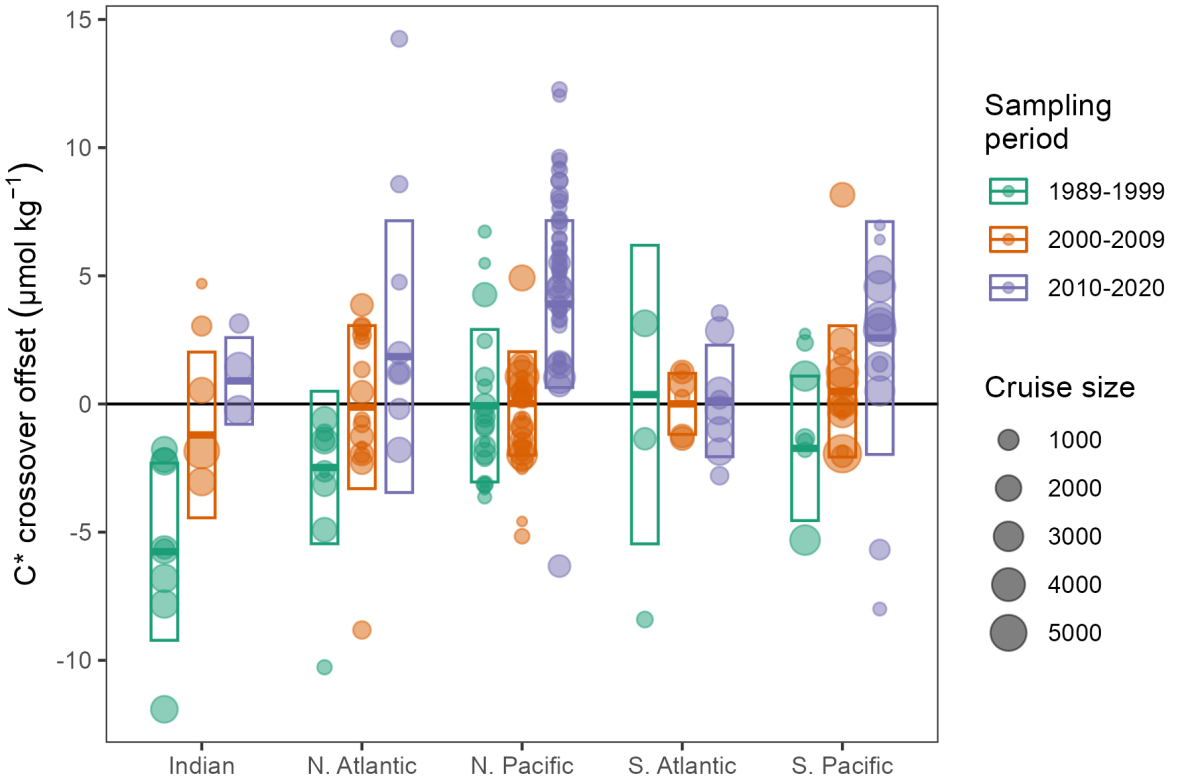

Fig. S3: Mean deep water cruise offsets in C* units against reference cruises from the 2000s. Colors distinguish cruises from each of our three sampling periods. Symbol size refers to the number of observations per cruise. The centre of the boxes indicate the mean offset across all cruises weighted by the number of observations per cruise, and the height represents the standard deviation across all offsets. The deep water crossover offsets shown here refer to the same depth thresholds also used by GLODAP to exclude data from the most variable parts of the ocean (Lauvset et al., 2021; Olsen et al., 2016), i.e. those sampled shallower than 1500 dbar in most regions.

Among the Indian Ocean data collected in the 1990s, more than 60% of the measurements were made in the framework of the WOCE sampling campaign with RV Knorr in 1994/95, identified as all Indian Ocean cruises with expocodes starting with 316N199. For these cruises, the offsets determined through the reanalysis of GLODAP crossover data are consistent in sign and magnitude with offset determined from measurements of certified reference materials for TA (Millero et al., 1998) and DIC (Johnson et al., 1998). In contrast to the general procedure applied to more recent cruises, the CRM offset determined for the RV Knorr cruises were not applied to the seawater measurements before the compilation of the data into GLODAP (Johnson et al., 2002).

According to the CRM measurement and in agreement with the mean decadal GLODAP crossover offset, we apply following bulk adjustments to all Indian Ocean RV Knorr cruises from the 1990s:

- TA: -3.5 µmol kg^{-1}
- DIC: +1.7 µmol kg^{-1}

The CRM based adjustments applied here were approved by the GLODAP reference group and applied in GLODAPv2.2022 (Lauvset et al., 2022).

According to the mean decadal GLODAP crossover offset, we further apply following bulk adjustments to all North Pacific cruises from the 2010s:

- TA: +2.05 µmol kg^{-1}
- DIC: -0.6 µmol kg^{-1}
- Phosphate: 1.007 (multiplicative adjustment)

It should be noted that our adjustments of the North Pacific data from the 2010s do not aim to improve the accuracy of these data, but to increase their consistency with the observations from the two previous sampling periods (1990s and 2000s), which were found to be internally more consistent (Fig. S3). Furthermore, all adjustments listed above are within the consistency targets and adjustments limits of GLODAP and would therefore not normally be adjusted during GLODAP's secondary quality control The offsets were only detected when analysing the crossover results from a decade-by-decade perspective as relevant to this study, and when converting the offsets from the individual parameters into C* units. It can thus not be concluded that the originally applied GLODAP adjustments are inappropriate.

In addition to the bulk adjustments listed above, we also tested a cruise-by-cruise adjustment of the data from the same periods, based on the mean offset of each cruise to cruises from the 2000s (Fig. S3). These tests revealed a largely consistent ΔC_{ant} reconstruction compared to the outcome with bulk adjustments (Fig. S9).

S1.3 Data gap-filling

The eMLR(C*) method requires that samples that are included in the analysis provide all required variables. Some cruises were initially not included after the flagging criteria were applied, because they lack measurements of only one of the nutrients (nitrate or phosphate) or TA for the calculation of C*. Our tests with synthetic data revealed that in some regions and decades the lack of the affected cruises is detrimental to the robustness of the ΔC_{ant} reconstructions, which was identified as an increase of the column inventory biases by more than a factor of two when comparing reconstructions with and without these data. The tropical Atlantic and the Southern Pacific were in particular affected by this lack of observations. To increase the robustness of our reconstructions through a better data coverage, we also include observations (Fig. 1 and Table S1) of nitrate, phosphate or TA that did not fulfil the strictest quality criteria (i.e. f-flag=2 and qc-flag=1). In cases where the flagging criteria were not met but data were provided through GLODAP, we used the available data. In cases where a parameter was not available at all, we used CANYON-B predictions (Bittig et al., 2018) for gap-filling, but only in cases where the required input parameters (including O_2) fulfilled our flagging criteria. The sufficient quality of all data sources used for the gap-filling (Table S1) was confirmed through additional quality assurance tests (see Table S1). The gap-filling procedure is reflected in our uncertainty assessment by including reconstructions with perturbed gap-filled data in our ensemble (Fig. S9).

Table S1: Gap-filling and quality assurance of observations that deviate from our standard flagging criteria (i.e., f-flag=2 and qc-flag=1), but were still included in the analysis to avoid large regional data gaps. Footnotes: (1)Wrongly assigned qc flags of 1 were identified in GLODAPv2.2021. This refers to DIC or TA data calculated from the fugacity of carbon dioxide (fCO_2). As fCO_2 was not secondary quality controlled, any derived parameter should carry a qc flag of 0, which was not always the case. This error was corrected for the purpose of this study and in GLODAPv2.2022 (Lauvset et al., 2022). (2)The offset of calculated TA data can plausibly be explained by any kind of TA contribution (e.g. from organic acids) that is not included in the acid-base system considered for the calculation. This "excess alkalinity" was previously estimated to be in the order of +4 µmol kg^{-1} in the open ocean (Fong and Dickson, 2019), which is in good agreement with the adjustment applied here.

Cruise expocodes	Gap filling procedure	Quality assurance
06MT19900123 316N19920502 316N19921006	Available TA data calculated from DIC and pCO_2 were used as provided by GLODAP.(1)	Additional GLODAP crossover with measured TA data from other cruises; Calculated TA data are on average 3 µmol kg^{-1} too low based on deep water crossover to directly measured TA, and were thus adjusted by this value(2)
31DS19940126	Measured nitrate data were used although GLODAP qc-flags do not meet our flagging criterion	As a sensitivity test we did run the eMLR method without nitrate as predictor variable (thereby including cruise 31DS19940126). The ΔC_{ant} reconstruction were found to be indistinguishable from those with the measured nitrate data
33MW19930704 33RO20030604 33RO20050111 33RO19980123	Missing phosphate data were filled with CANYON-B prediction	Additional GLODAP crossover with measured phosphate data from other cruises; Predicted phosphate data agree within ±1% to measured data for each of the four cruises
06AQ19980328	Missing TA data were filled with CANYON-B prediction	Additional GLODAP crossover with measured TA data from other cruises; The mean absolute crossover offset between the predicted and measured TA data is <0.5 µmol kg^{-1}

S2 Additional minor configuration changes of the eMLR(C*) method

In the following, we describe additional configuration changes of the eMLR(C*) method compared to the analysis by Gruber et al. (2019). These configuration changes were tested, but did not result in a relevant difference of the ΔC_{ant} reconstructions compared to our standard case and were thus not considered in our uncertainty budget (see supplement S4).

S2.1 Data thinning, subsetting and clustering

A random spatial subsampling procedure was introduced to thin the data from densely sampled regions, thus avoiding their disproportionate impact on the ΔC_{ant} reconstruction. The data thinning was achieved by grouping the observations within each neutral density slab on a 5°x5° horizontal grid. The total number of observations in each of the grid cells was counted. In the n-th quantile of grid cells with the highest number of observations, the observations were randomly subsetted to be identical to the highest number of observations within the remaining grid cells. This data thinning maintains the bulk of data and does not

increase the number of observations in poorly sampled regions, but it reduces the number of data points in highly sampled grid cells. It was found that up to a quantile threshold of n ≈ 0.3, the data thinning has no noticeable effect on the ΔC_{ant} reconstructions, indicating a robustness of the eMLR(C*) results to uneven sampling distribution. A moderate thinning with n = 0.05 was used for our analysis.

A bottom depth threshold of 500m was tested to exclude observations from continental shelves. The ΔC_{ant} reconstructions with and without the observations from the coastal shelf were very similar. The removal of shelf data was thus not further considered.

For our standard configuration of the eMLR(C*) method, the data were clustered vertically into the neutral density slabs previously defined by Gruber et al. (2019), i.e., slabs with boundaries at 26.00, 26.50, 26.75, 27.00, 27.25, 27.50, 27.75, 27.85, 27.95, 28.05, 28.10, 28.15, 28.20 kg m^{-3}, of which the two highest density boundaries were only used in the Atlantic Ocean. Neutral densities were calculated from salinity and temperature following Jackett and McDougall (1997). Halving the number of these density slabs by combining two adjacent slabs did not strongly impact the outcome. The general spatial ΔC_{ant} distribution was even maintained when no slab separation was applied. We thus deem the slab separation to be of secondary importance for our analysis and included only reconstruction based on the standard density slabs in our uncertainty assessment.

S2.2 MLR model selection criteria

Among the 2 x 120 MLR models fitted for each density slab and decade, the best models were selected. As a first step, MLR models with a combination of multicollinear predictors were removed. These models were identified as those with a variance inflation factor (VIF) higher than 500, which is an alternative procedure to the previous arbitrary decision to limit the maximum number of predictors to 5 out of 7 (Gruber et al., 2019). The selected VIF of 500 represents a rather weak threshold, as our test with synthetic data revealed that stricter removal criterion (e.g. VIF ≤ 100) increases the biases of the ΔC_{ant} column inventories. The rather weak sensitivity of the eMLR outcome to the VIF threshold indicates a general robustness of the eMLR(C*) method to multicollinearity of predictors.

Among the remaining MLR models, the 10 models with the lowest summed root mean squared error (RMSE) across both sampling periods were selected for the ΔC_{ant} prediction. The Akaike information criterion (AIC) was tested as an alternative model selection criteria to the RMSE. Both approaches result in essentially identical ΔC_{ant} reconstructions, indicating a robustness of the eMLR(C*) method toward overfitting the data.

We did perform ΔC_{ant} reconstructions after individually removing each of the predictor variables. It was found that any predictor can be removed without a noticeable impact on the ΔC_{ant} reconstruction, with the exception of the nutrient that was used for C* calculation. This indicates a certain redundancy among the complete set of possible predictor variables, which is consistent with the finding that the avoidance of predictor collinearity based on the VIF criterion has only a weak impact on the ΔC_{ant} reconstruction.

S3 Additional observation-based results

S3.1 Column inventory maps of β

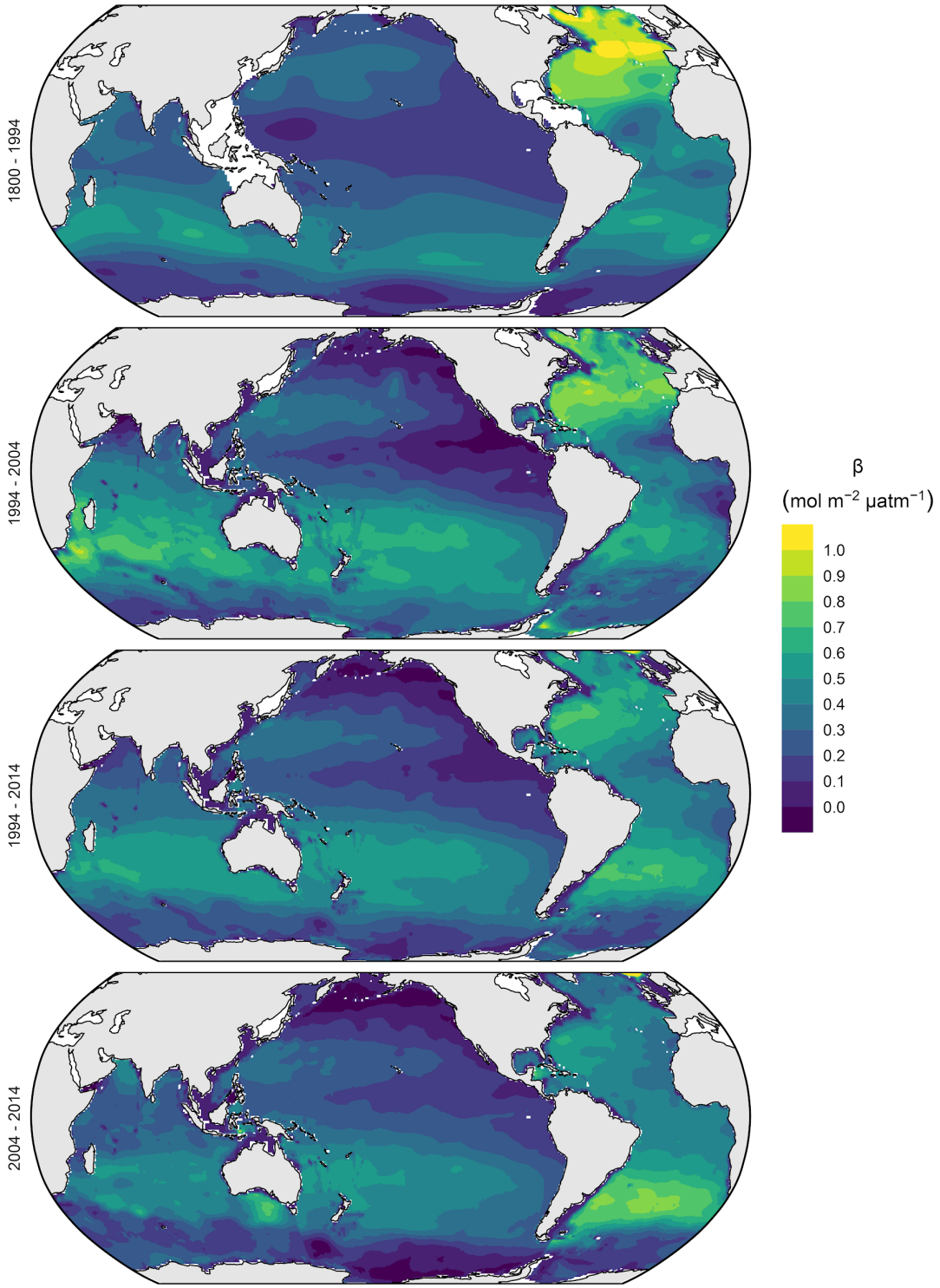

Fig. S4: Column inventory maps of $\beta = \Delta C_{ant} / \Delta pCO_{2,atm}$ for the preindustrial period from 1800–1994, as well as for the two decades and the 20-year period analysed in this study.

S3.2 Regional and global mean β column inventories

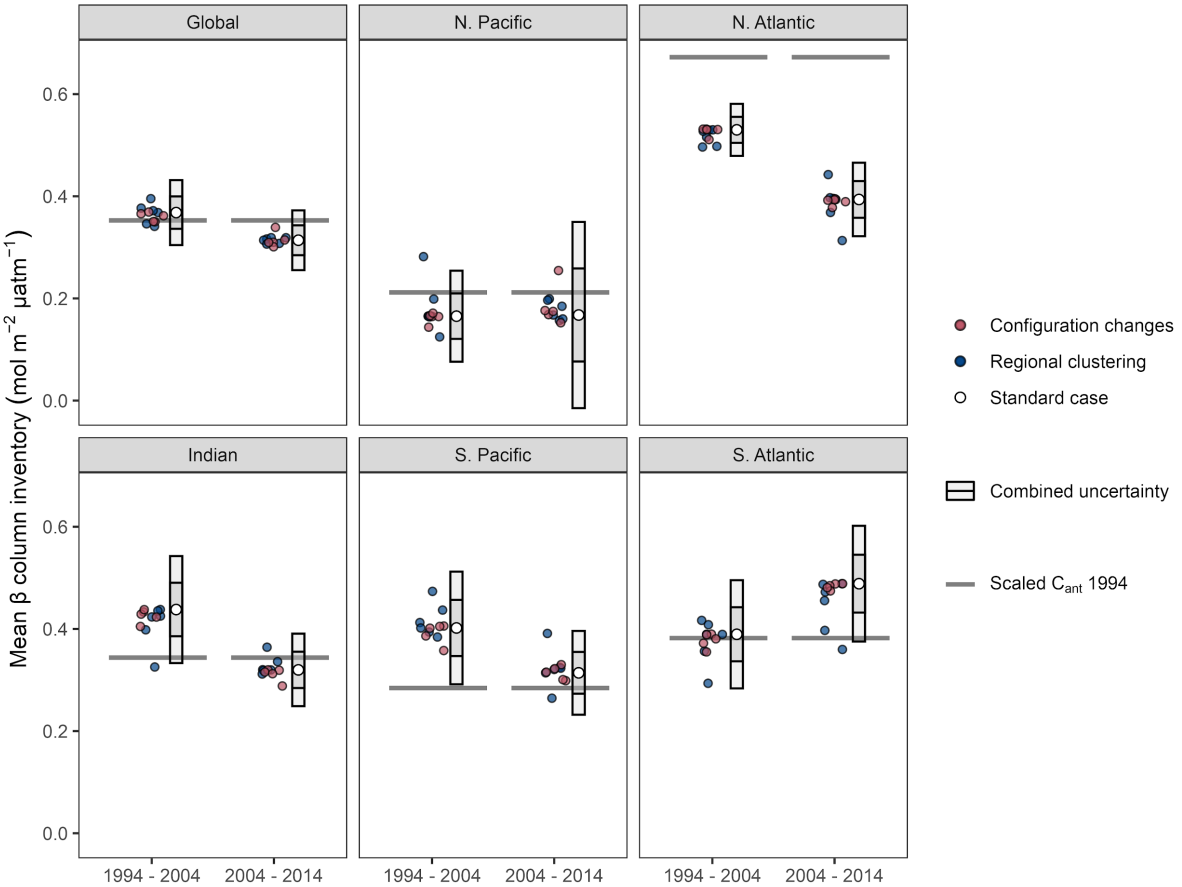

Fig. S5: Global and regional mean column inventories of β = ΔC_{ant} / $\Delta pCO_{2,atm}$ for the decades 1994–2004 and 2004–2014. White points represent the standard case and error bars the 1σ- and 2σ-uncertainty ranges. Other points represent ΔC_{ant} reconstructions considered for the uncertainty assessment (red: configuration changes; blue: regional clustering). Horizontal lines indicate β inventories based on the total C_{ant} storage in 1994 (Sabine et al., 2004).

S3.4 Reproduction of the study by Gruber et al. (2019)

In addition to our estimates for the two decades since 1994, we reconstructed ΔC_{ant} from 1994–2007 to test the consistency of our approach with the analysis by Gruber et al. (2019). For this purpose, we clustered the observations into the same sampling periods (1982–1999 and 2000–2014) used by Gruber et al. (2019), while maintaining all other configurations of the eMLR(C*) method as applied in this study. With this approach, we find indistinguishable global ΔC_{ant} inventories (33 ± 4 Pg C vs 34 ± 4 Pg C) and very similar spatial distribution of the column inventory changes from 1994–2007 (Fig. S6). This agreement underlines the robustness of our findings and similarity of the approaches when taking into account that we used different releases (v2 vs v2.2021) of GLODAP (Lauvset et al., 2021; Olsen et al., 2016) and the World Ocean Atlas (Locarnini et al., 2019; Zweng et al., 2019), introduced modification of the eMLR(C*) method and applied data adjustments. It should be noted that the analysis of Gruber et al. (2019) is based on unadjusted Indian Ocean data from the 1990s, but in their standard case, which combines the Indian Ocean and Pacific into one

spatial cluster (basin mask “2” in Fig. S1), the regional impact of the unadjusted data is less pronounced compared to a separate analysis of the Indian Ocean as performed in this study and the sensitivity cases 107 and 110 of Gruber et al. (2019). The less pronounced impact of the unadjusted data in the Indian Ocean in the earlier study could also partly be due to the manual removal of “stations with an excessive amount of scatter in the computed C* tracer” (Gruber et al., 2019).

The analysis for the 1994–2007 periods incorporates observations from 2000–2014 for the second sampling period, i.e., only data collected since 2015 are used for the first time in our analysis of the 2004–2014 decade. The fact that the increasing C_{ant} storage rates in the South Atlantic Ocean emerge already in the 1994–2007 reconstruction, while the North Atlantic Ocean still maintains a relatively strong, yet already weaking storage rate, is most likely due to the incorporation of a good fraction of the observations from the early 2010s in the analysis of the 1994–2007 period.

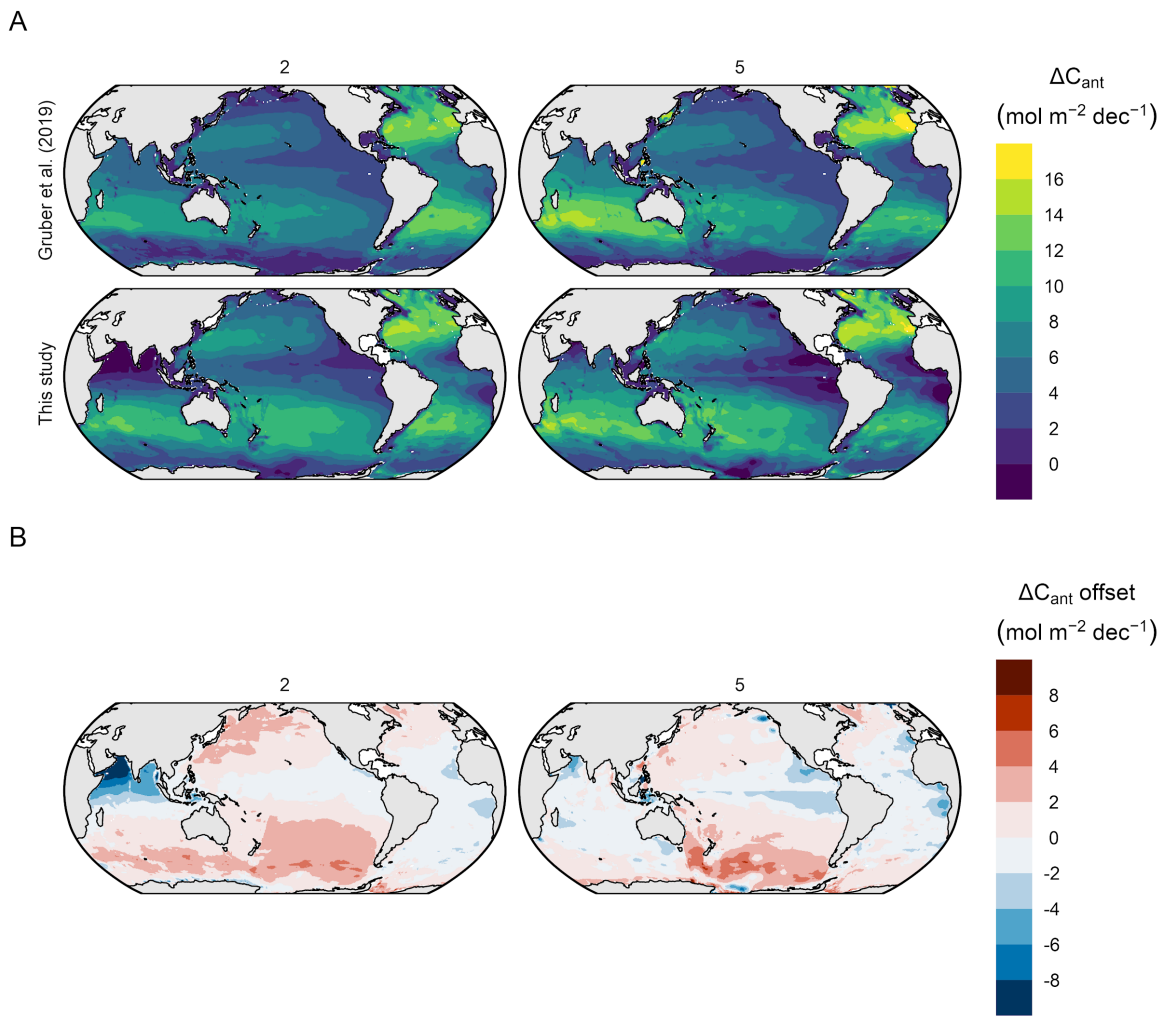

Fig. S6: Column inventory maps of (A) ΔC_{ant} for the period 1994-2007 as analysed by Gruber et al. (2019) and in this study (panel rows). Reconstructions are shown for the two regional clustering schemes “2” and “5” (Fig. S1) that were applied in both studies (panel columns). (B) ΔC_{ant} offset between Gruber et al. (2019) and this study.

S3.5 Zonal mean sections of ΔC_{ant}

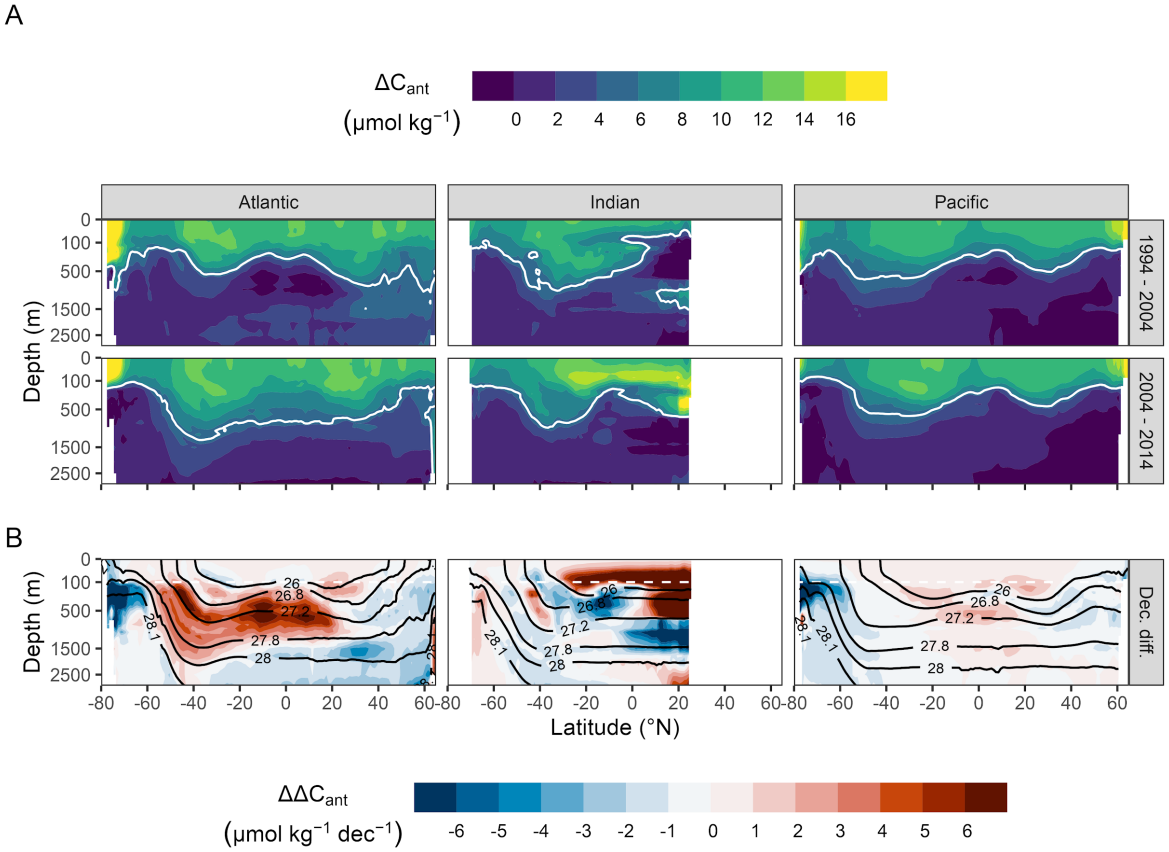

Fig. S7: Zonal mean sections of (A) ΔC_{ant} for each ocean basin (columns) and decade (rows). White contour lines highlight a ΔC_{ant} level of 5 μmol kg^{-1} dec^{-1}. (B) Decadal differences in the storage changes ($\Delta\Delta C_{ant}$). Black contour lines indicate isoneutral density levels, where the selected boundaries represent every second density slab used to cluster the data in the vertical dimension.

The strong decadal differences between the ΔC_{ant} zonal mean sections in the Northern Hemisphere of the Indian Ocean (Fig. S7B) are a consequence of the lack of observations in the Arabian Sea during the central sampling period (2000–2009) of our analysis. This data sparsity requires strong spatial extrapolation to reconstruct the C* distribution, which leads to higher uncertainties. The resulting bias structures according to our tests with synthetic data (Fig. S16) are almost mirrored in the Northern Hemisphere of the Indian Ocean for the 1994–2004 and 2004–2014 decade, because the data sparsity in the central sampling period affects both reconstructions inversely. In terms of the ΔC_{ant} column inventories, the positive (surface) and negative (1000–1500 m) extrapolation errors in the Northern Indian Ocean largely cancel out (Fig. S13). In terms of the mean ΔC_{ant} profiles (Fig. 4A) and whole-basin inventories (Figs. 4B and 5) for the Indian Ocean, the impact of the extrapolation uncertainty is negligible due to low volume of the affected water masses. Our 20yr reconstruction from 1994–2014 is also not affected by this issue, because it does not require data from the central sampling period (2000–2009).

S3.6 Residuals of MLR models

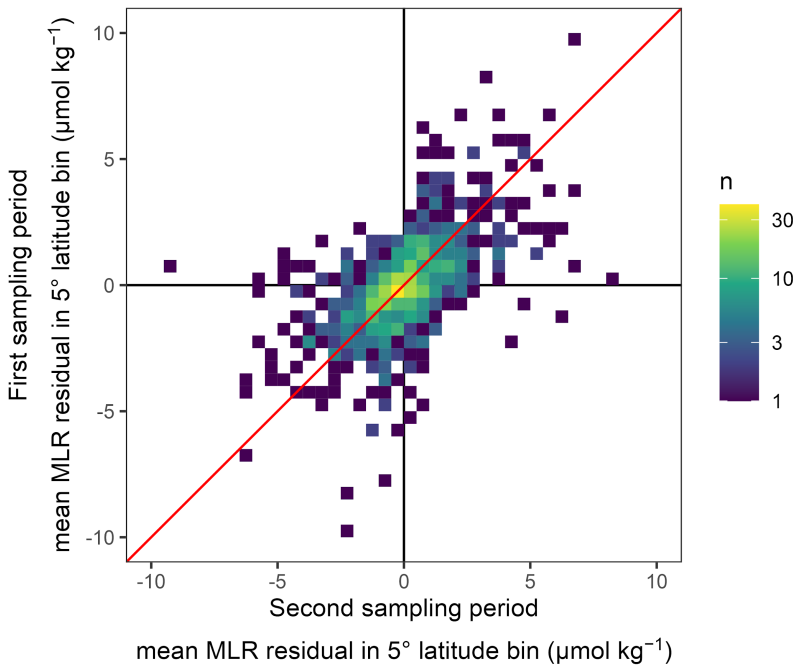

Fig. S8: Residuals of the MLR models averaged over 5° latitude bins within each density slab, shown as a heatmap of residuals from the first in comparison to the second sampling period. The correlation coefficient is 0.56.

S4 Determination of uncertainty based on configuration changes of the eMLR(C*) method

S4.1 Uncertainty quantification

Our primary uncertainty quantification is based on an ensemble of ΔC_{ant} reconstructions that differ with respect to the specific configuration of the eMLR(C*) method. For this purpose, we identified the most impactful configuration changes of the method that are still believed to provide an equally likely representation of the true ΔC_{ant} distribution as our standard case. The following description of our uncertainty quantification refers to the ΔC_{ant} reconstructions as the primary outcome of our analysis, but applies analogously to other derived estimates such as the mean penetration depth of ΔC_{ant}, β, or the ocean-borne fraction of CO_2 emissions.

One of the most important configuration choices of the eMLR(C*) method is the regional clustering of the data for the MLR fitting and mapping of ΔC_{ant}. In total, we applied six different basin mask definitions (Fig. S1), of which the basin mask "3" is used for our standard case reconstruction. The mean absolute difference (s_{reg}) between the ΔC_{ant} reconstructions obtained with basin mask "3" and the five alternative basin masks is considered as one component of our uncertainty budget.

The other configuration changes considered in our uncertainty estimate are:

1. Cruise-by-cruise data adjustments: Individual cruise adjustment values according to our crossover analysis (Fig. S3) were applied instead of a bulk adjustments (see supplement S1.2)
2. Modified gap-filling: Perturbations were applied to the gap-filled data reflecting the crossover offset between the gap-filled data and observations available from GLODAPv2.2021. Specifically, we perturbed CANYON-B predictions for TA with an offset of 1 μmol kg^{-1} and for phosphate data with a factorial offset of 1.01. Calculated TA data were perturbed with an offset of 3 μmol kg^{-1} (see supplement A1.3).
3. C*(N,TA) as target variable: Nitrate and TA rather than phosphate and TA were used for the calculation of C*.
4. Surface ΔC_{ant}: The surface ocean ΔC_{ant} was not estimated with the atmospheric equilibrium approach, but based on the observation-based surface ocean DIC product OceanSODA (Gregor and Gruber, 2021). To eliminate local and short-term variability in DIC from this product, a local linear regression for DIC as function of $pCO_{2,atm}$ was fitted for the period 1990–2020. Based on the slope of this regression, the surface ocean DIC increase was predicted between the reference years 1994, 2004 and 2014 according to the increase in $pCO_{2,atm}$.
5. WOA18 predictors: Nutrients and oxygen from World Ocean Atlas 2018 (Locarnini et al., 2019; Zweng et al., 2019) were used for the mapping of ΔC_{ant}, instead of the gridded climatologies based on GLODAPv2 (Lauvset et al., 2016).

For each of these five additional configuration choices, we calculated the difference between the ΔC_{ant} reconstructions obtained with standard configuration and the modified configuration ($s_{config,1\text{-}5}$), all of which were obtained using the basin mask "3".

For our global ΔC_{ant} inventories we consider an additional uncertainty component ($s_{scaling}$) arising from the upscaling of the directly mapped ΔC_{ant} inventories by +7% to account for storage changes in unmapped regions and the deep ocean. The uncertainty contribution is assumed to be half of the absolute scaling value, i.e. ±3.5% of the global ΔC_{ant} inventories. This assigned scaling uncertainty reflects the uncertainty in the underlying regional inventories and the potential for their non-steady growth.

The combined uncertainty was determined as the square root of the sum of squares (RSS) of the individual uncertainty components:

$$s_{combined} = \sqrt{s_{reg}^2 + \sum_{i=1}^{5} s_{config,i}^2 + s_{scaling}^2}$$

We consider the combined uncertainty $s_{combined}$ as standard uncertainty ($\pm 1\sigma$) of our reconstructions representing a 68% confidence interval. We derive the expanded uncertainty of our estimates through multiplication of $s_{combined}$ with a factor of 2. The obtained expanded uncertainty ($\pm 2\sigma$) represents a confidence interval of 95%. All results are reported with $\pm 1\sigma$ uncertainty ranges. A difference between two estimates is considered significant if the absolute difference is larger than the combined uncertainty, i.e., the RSS of the 1σ-uncertainties of both estimates.

The individual uncertainty components s_{reg} and $s_{config,1\text{-}5}$ are displayed at the 1σ-level for column inventories in Fig. S9 and for inventories in Fig. 6. Fig. 6 also includes $s_{scaling}$ for the global estimate. The combined uncertainty $s_{combined}$ at the $\pm 1\sigma$ level is displayed for column inventories in Fig. S10.

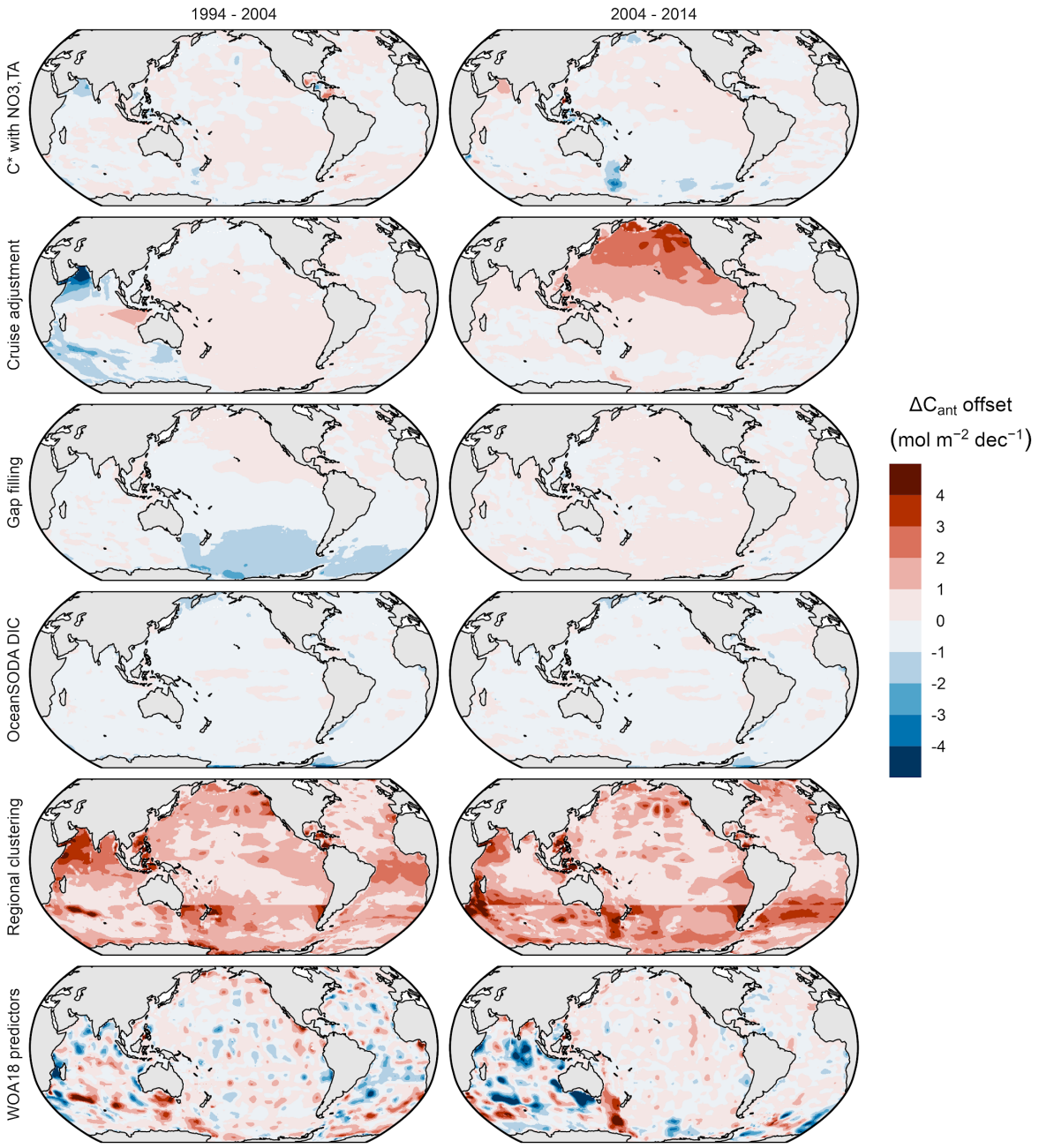

Fig. S9: Individual column inventory uncertainty contributions determined as offsets between our standard case reconstruction and six configuration choices of the eMLR(C*) method (panel rows) for both decades (panel columns). Negative values indicate that lower column inventories were obtained with the configuration changes. The regional clustering offsets are positive by definition, as they represent the mean absolute offsets across five alternative basin masks.

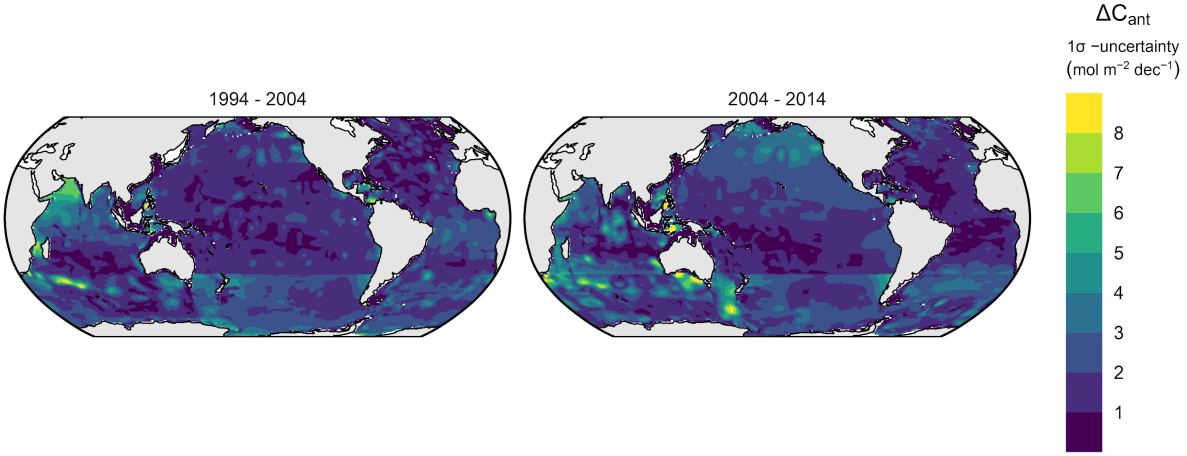

Fig. S10: Combined column inventory uncertainties at the 1σ-uncertainty level. Panel rows distinguish the two reconstructed decades. The combined uncertainties are determined as the square root of summed squared offsets (RSS) of the individual uncertainty components shown for observations in Fig. S9.

S4.2 Further sensitivity analysis

Following the same approach as for the primary uncertainty quantification described above (supplement S4.1), we assess the sensitivity of our ΔC_{ant} reconstructions to additional configuration choices of the eMLR(C*) method. These reconstructions are not believed to provide an equally likely representation of the true ΔC_{ant} distribution as our standard case, but are intended to illustrate the sensitivity to certain aspects of the method such as the data coverage or data consistency. The considered changes of the configuration are:

1. No data adjustment: All data are used as published in GLODAPv2.2021 (see supplement A1.2).
2. Reoccupation filter: Only data from sections that were reoccupied are used. The filtering criterions is that at least one record must be available within a density slab and 1°x1° horizontal grid box for each of two compared sampling periods.
3. C*(P) target variable: C* was calculated only with phosphate (neglecting TA).
4. DIC target variable: DIC was used as a target variable, i.e. without removing a nutrient or TA contribution and without adjusting to the reference year (t_{ref}).
5. No tref adjustment: Calculation of C* based on phosphate and TA as in the standard case, but without temporal adjustment to the reference year (t_{ref}).

The individual sensitivity components are displayed at the 1σ-level for column inventories in Fig. S11 and for inventories in Fig. S12.

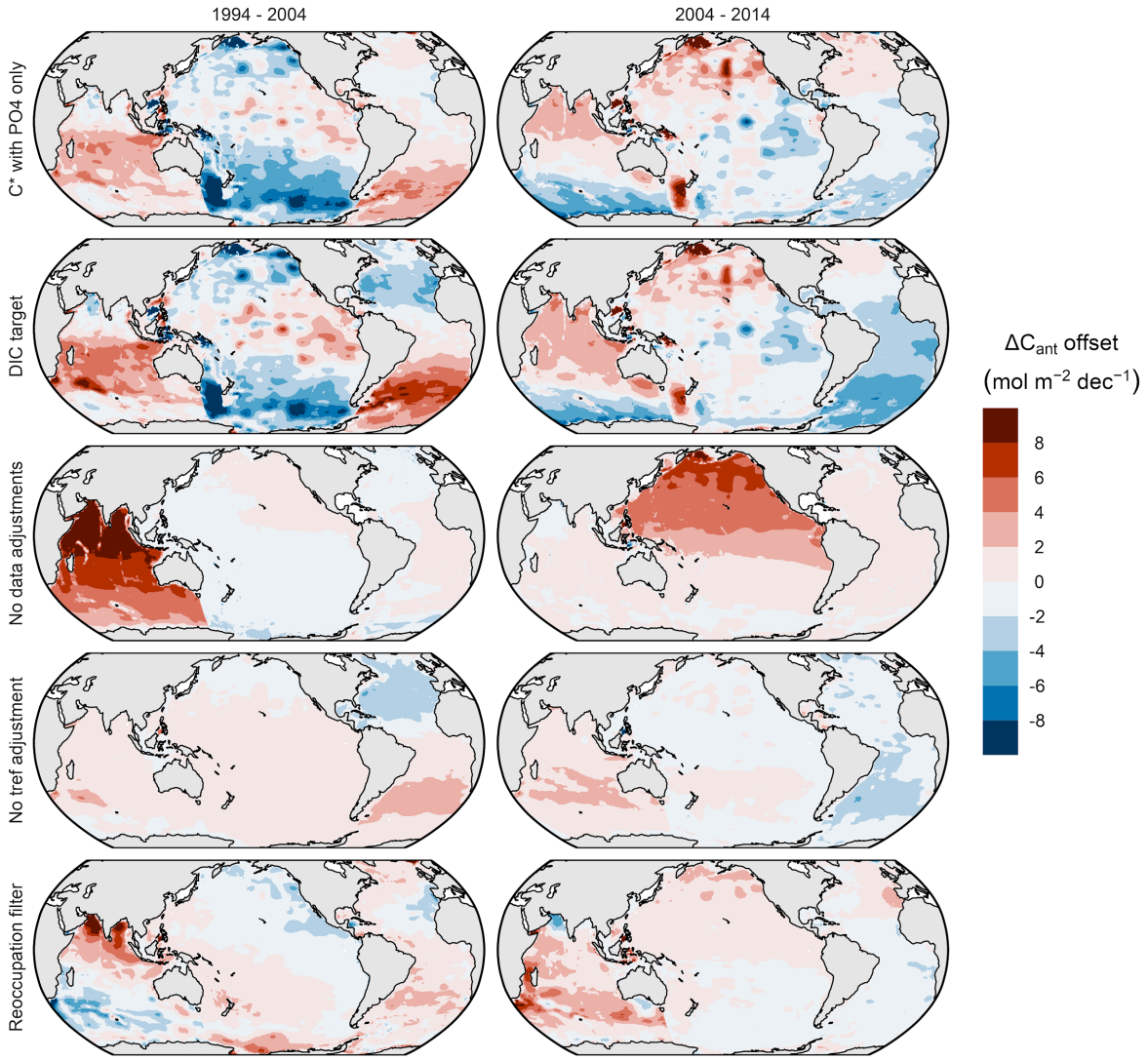

Fig. S11: Column inventory sensitivity to specific aspects of the eMLR(C*) method at the 1σ-uncertainty level determined as offsets between our standard case reconstruction and five sensitivity reconstructions (panel rows) shown for both decades (panel columns). Negative values indicate that lower column inventories were obtained with the sensitivity tests. Note that the sensitivity reconstructions are not included in the uncertainty budget as they are not considered an equally likely representation of the true ΔC_{ant} signal.

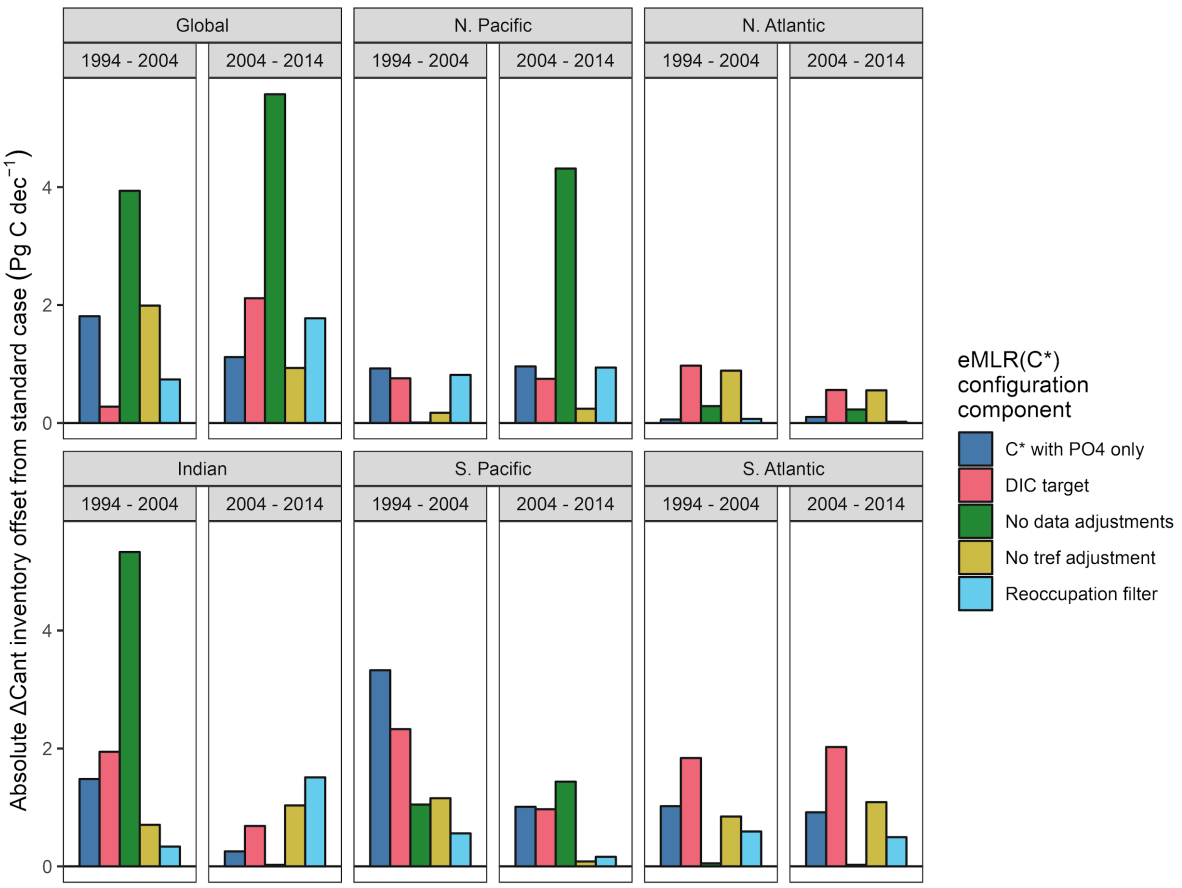

Fig. S12: Inventory sensitivity at the 1σ-uncertainty level determined as offsets between our standard case reconstruction and five sensitivity configurations of the eMLR(C*) method (colours) for each ocean region and both decades (panels). All offsets are shown as absolute values. Note that the sensitivity reconstructions are not included in the uncertainty budget as they are not considered an equally likely representation of the true ΔC_{ant} signal.

S5 Testing of the eMLR(C*) method with synthetic data

For the purpose of testing the eMLR(C*) method with respect to biases that cannot be retrieved from its application to observational data, we generated a synthetic data set which contains data that were subsetted from a GOBM according to the spatio-temporal coverage of real-world observations available through GLODAP. Applying the eMLR(C*) method to this synthetic data set allows us to compare the reconstructed ΔC_{ant} distribution to the model truth and thereby assess the quality of the reconstruction. The assessment with synthetic data was previously used for the development of the eMLR(C*) method and was described in detail by Clement and Gruber (2018).

S5.1 Generation of synthetic data from CESM model

The synthetic data set used in this study was generated from the Community Earth System Model (CESM), an ocean circulation hindcast model with embedded biogeochemistry (Doney et al., 2009). After a 180-year spin-up phase, two model runs A and D were split up and forced with the historic (Dlugokencky and Tans, 2019) and preindustrial atmospheric CO_2 concentration, respectively. Both runs were forced with historic surface-atmospheric data from JRA55-do (Tsujino et al., 2018) during the analysis period. The raw model output was horizontally regridded to a regular 1°x1° grid, while the original irregular 60 depth levels were maintained. The model output used in this study was also submitted and analysed in phase 2 of the REgional Carbon Cycle Assessment and Processes project (RECCAP2) and will be made available upon completion of this project (Poulter et al., 2022).

The synthetic data set was created by subsetting model run A (increasing atmospheric CO_2, variable climate). Therefore, the model output was linearly interpolated between depth levels to match the exact sampling depth in GLODAP. Annually averaged model truth fields of total C_{ant} were calculated as the difference in DIC between model runs A and D (preindustrial atmospheric CO_2, variable climate). ΔC_{ant} was calculated as the difference between total C_{ant} at the second (t_{ref2}) and first (t_{ref1}) reference year of each analysis decade. Climatological fields of the predictor variables were calculated as the annual average of the year 2007.

S5.2 Method evaluation results

Our tests with synthetic generated from the GOBM confirm that the eMLR(C*) method is capable of retrieving the global ΔC_{ant} patterns in the horizontal (Fig. S13) and vertical (Figs. S16 and S17A) dimension when applied to data that represent the spatio-temporal coverage of observations available for the past three decades. The absolute column inventory biases of our standard case reconstruction (Fig. S13B) are below 2 mol m^{-2} dec^{-1} for most parts of the ocean (87% of the total surface area), and only in a few regions increase up to 4 mol m^{-2} dec^{-1} (13%) or exceed the latter threshold (<0.5%). In contrast, the ΔC_{ant} column inventories in our model are larger than these thresholds of 2 and 4 mol m^{-2} dec^{-1} over more than 55 and 90% of the surface area of the ocean, respectively (Fig. S13A). Likewise, the biases of the standard case reconstruction in the zonal mean sections (Fig. S16B) are mostly within 2 µmol kg^{-1}, which is about half as much as the decadal changes in the observation-based ΔC_{ant} reconstructions (Figs. 3 and S7).

When comparing the ΔC_{ant} depth layer inventories of our standard case reconstructions to the model truth (Fig. S17B), we find that in most ocean basins and depth layers the offsets

are within the 2σ-uncertainty range determined from our ensemble of eMLR(C*) reconstructions. When comparing the reconstructed ΔC_{ant} inventories integrated over the top 3000 m to the model truth (Fig. S18), we find that out of the 12 reconstructed ΔC_{ant} inventories, 7 and 11 revealed a bias that is within the 1σ- and 2σ-uncertainty range (Fig. S18), which meets the expectation of 68% and 95% confidence intervals, respectively. Only the bias of our standard case inventory for the South Atlantic slightly exceeds the 2σ-uncertainty range for the 2004–2014 decade.

When interpreting the outcome of our tests with synthetic data, it should be taken into account that the CESM model that we used as a testbed reveals a lower decadal ΔC_{ant} variability than our observation-based reconstructions, as well as a generally low C_{ant} storage in the North Atlantic due to a weak AMOC in the model. It should further be noted that any potential model drift would affect the synthetic data generated from run A, but not the model truth ΔC_{ant} field which is calculated as a difference of two model runs (A and D). Thus, our bias estimate also includes a model drift component.

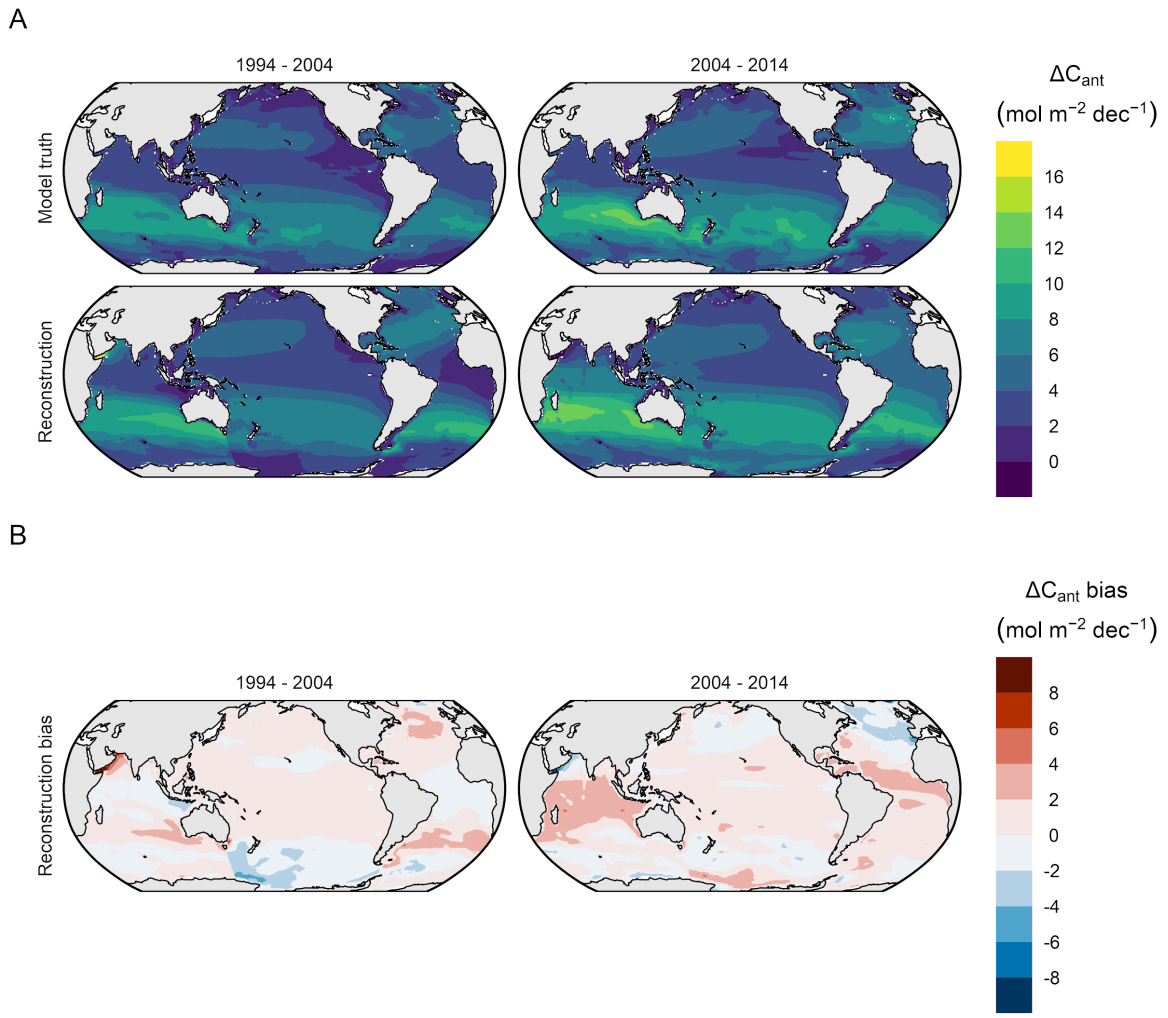

Fig. S13: Column inventory maps of changes in anthropogenic CO_2 (ΔC_{ant}) integrated over the upper 3000m, comparing the eMLR(C*)-based reconstructions with the model truth. (A) Absolute ΔC_{ant} for two decades from 1994 to 2014. (B) Bias in the eMLR(C*)-based reconstructions compared to the model truth as shown in (A).

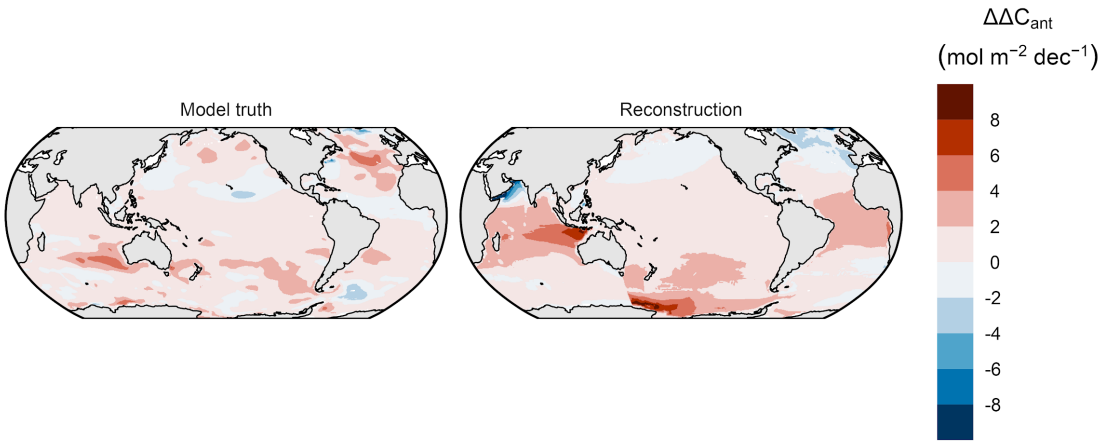

Fig. S14: Same as Fig. S13B, but contrasting the reconstructed decadal differences ($\Delta\Delta C_{ant}$) in the storage changes with the model truth, instead of showing the reconstruction bias for both decades.

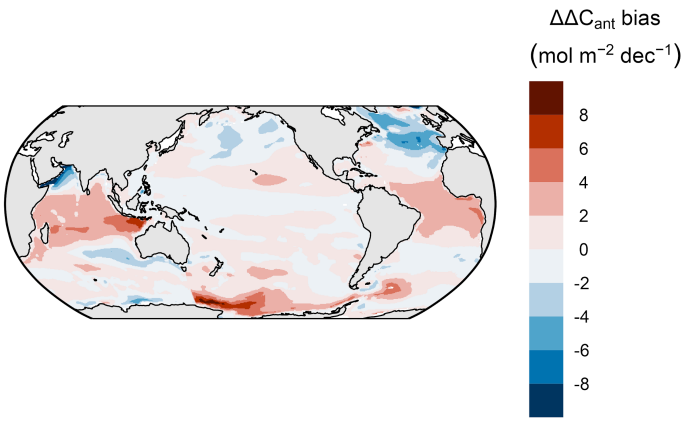

Fig. S15: Same data as Fig. S14 but showing the bias in the decadal differences ($\Delta\Delta C_{ant}$ bias) in the storage changes by subtracting the model truth from the reconstruction.

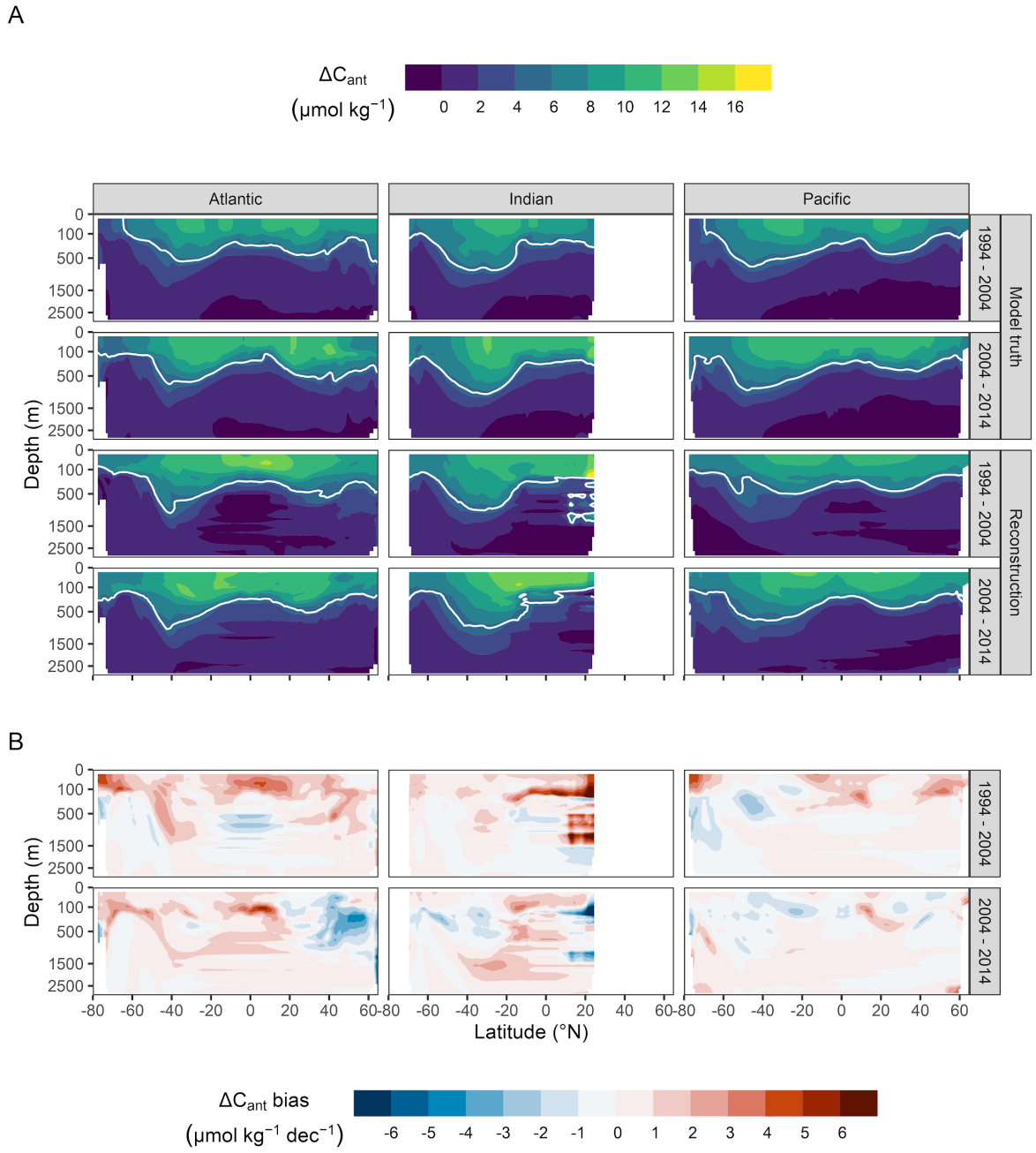

Fig. S16: Zonal mean sections of (A) ΔC_{ant} for each ocean basin (columns) and two decades (rows), comparing the eMLR(C*)-based reconstructions with the model truth. White contour lines indicate a ΔC_{ant} leval of 5 μmol kg^{-1} per decade. (B) Bias in the eMLR(C*)-based reconstructions compared to the model truth as shown in (A).

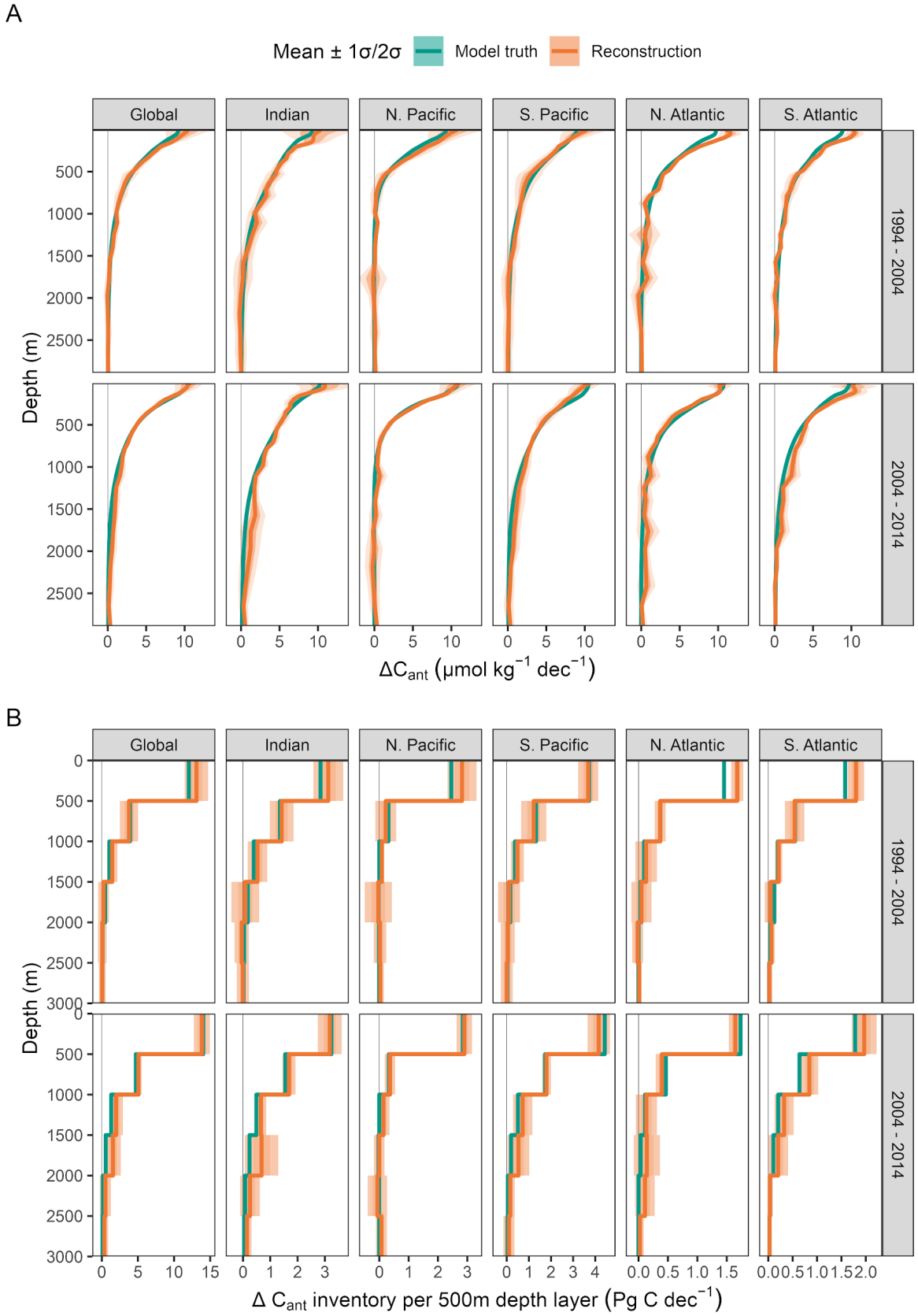

Fig. S17: (A) Mean profiles and (B) 500m depth layer inventories of the changes in anthropogenic carbon content (ΔC_{ant}) for each hemispheric basin and the global ocean (columns) as well as the two decades since 1994 (rows). Colours distinguish the eMLR(C*)-based reconstructions and the model

truth. Thick lines represent the standard case reconstruction and the model truth of ΔC_{ant}, while ribbons indicate the 1σ- and 2σ-uncertainty ranges of the reconstructions based on an ensemble of reconstructions. Note that the model truth estimates do not have an uncertainty ribbon.

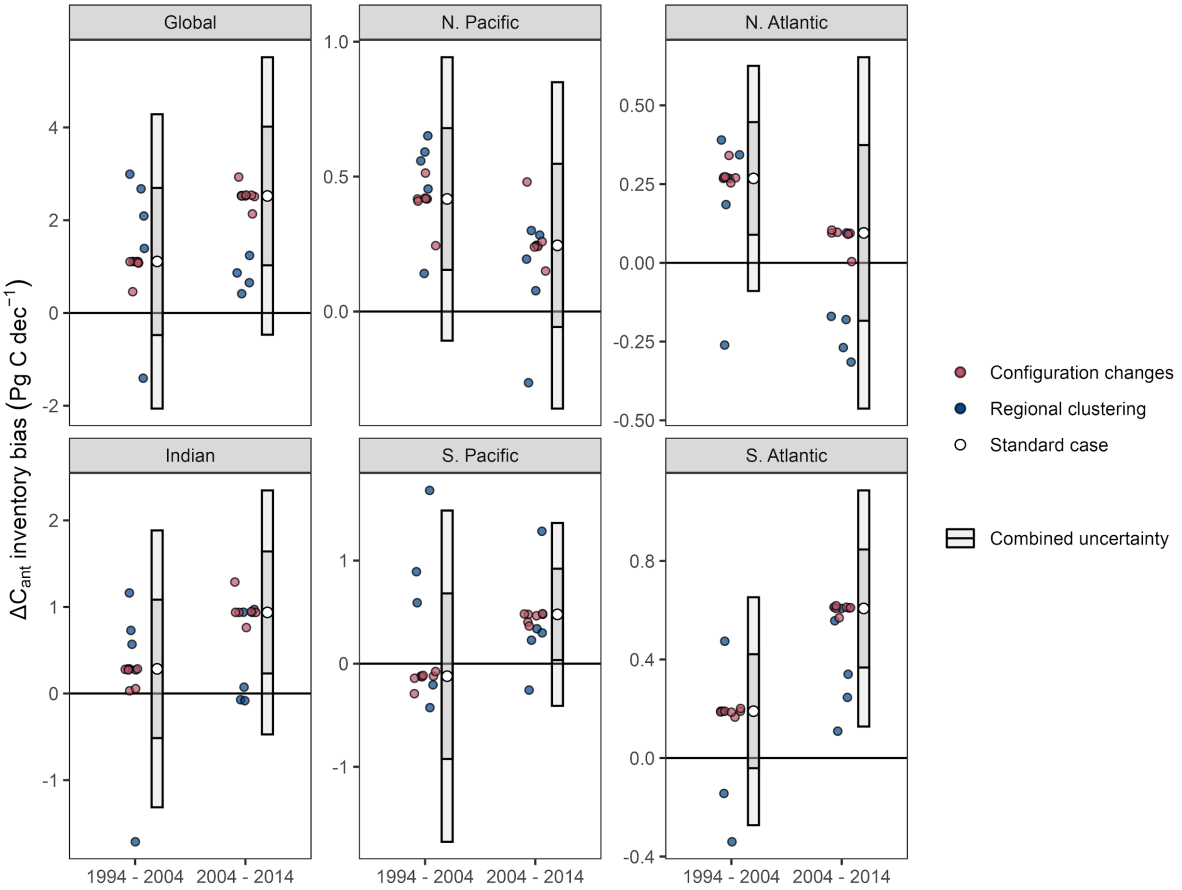

Fig. S18: Biases in the ΔC_{ant} inventories for each ocean basin and the global ocean, and the decades 1994–2004 and 2004–2014. White symbols represent the standard case of our ΔC_{ant} reconstructions and error bars the 1σ- and 2σ-uncertainty ranges. Coloured points represent ΔC_{ant} reconstructions considered in the uncertainty assessment (red: configuration changes of the eMLR(C*) method; blue: regional clustering).

S6 Comparison of regional ΔC_{ant} inventories to previous studies

In the following, we provide a detailed comparison of our ΔC_{ant} inventories for each hemisphere of the main ocean basins (Table 1) to previous regional estimates. The selected regional studies rely — like our reconstructions — on ocean interior biogeochemical observations, apply an MLR approach, and cover multiple time periods. All regional analyses compare individual reoccupied sections as a first step and subsequently extrapolate the ΔC_{ant} reconstruction from a single or multiple sections to the whole basin. This stands in contrast to our global eMLR(C*) approach, which uses all observations from one spatial cluster together in a single MLR fitting procedure. In general, it can thus be assumed that the global eMLR(C*) approach is less sensitive to measurement biases of individual cruises but also less sensitive to small scale ΔC_{ant} signals (Carter et al., 2019). For consistency with our reporting, we converted the uncertainty estimates of the regional studies to 1σ uncertainty ranges whenever possible, while potential differences in the exact spatial coverage are neglected.

In the North Atlantic Ocean, Woosley et al. (2016) found a significant increase in C_{ant} storage rates from 1.9 ± 0.4 Pg C dec^{-1} for the 1989–2003 period to 4.4 ± 0.9 Pg C dec^{-1} for 2003–2014. While the latter estimate is indistinguishable from our storage rate for the 2004–2014 decade (3.9 ± 0.4 Pg C dec^{-1}), their sink estimate for the first period is drastically lower than ours for the 1994–2004 decade (4.8 ± 0.2 Pg C dec^{-1}). This leads to opposite interpretations of the North Atlantic as a C_{ant} sink that is strongly increasing (Woosley et al., 2016) or moderately decreasing (this study) in strength. The changes reported by Woosley et al. (2016) rely on the comparison to a previous study by Wanninkhof et al. (2010) and are based on the reoccupation of a single north-south transect (A16) which covers the eastern basin of the North Atlantic Ocean. Thus, one likely cause for the different findings lies in their use of a single section in contrast to our use of data from all available cruises. Studies that compared ΔC_{ant} estimates for the Atlantic Ocean based on the analysis of single vs multiple reoccupied cruise lines indeed found that the inventories for whole hemispheric basins differ by around 30% (Gao et al., 2022; Woosley et al., 2016), which was attributed to insufficient observational coverage of east-west ΔC_{ant} gradients (Fig.1) by a single north-south oriented hydrographic section. Another reason why our inventories may differ from the regional analysis is the integration depth. While our study provides integrals over the top 3000m, Woosley et al. (2016) restricted their inventory calculation to water masses with ΔC_{ant} exceeding 3 µmol kg^{-1}, a threshold that is mostly located shallower than 2000m along the A16 section in the North Atlantic. Indeed, the depth layers that contribute to the decadal decrease of our inventories range from 1500 to 3000m (Fig. 3B). In contrast, our inventories over the top 1000m also show a tendency towards slightly higher C_{ant} storage changes in the more recent decade. Thus, whether we interpret the sink strength of the North Atlantic as increasing or decreasing depends among others on the chosen integration threshold.

For the South Atlantic Ocean, Woosley et al. (2016) reported a rather steady uptake rate (3.7 ± 0.8 and 3.2 ± 0.7 Pg C dec^{-1}) based on the analysis of a single reoccupied cruise section (A16S). In contrast, Gao et al. (2022) found that the rate of C_{ant} storage accelerated from 3.1 ± 0.2 Pg C dec^{-1} for the 1989–2005 period to 4.9 ± 0.3 Pg C dec^{-1} for the 2005–2013 period when extrapolating from the same A16S section to the whole South Atlantic basin. The most important difference between these two regional studies is again the choice of the vertical integration depth. While Woosley et al. (2016) restricted their

inventory calculation to ΔC_{ant} exceeding 3 μmol kg^{-1}, Gao et al. (2022) provided upon request integrated ΔC_{ant} over the top 3000 m (H. Gao and W.-J. Cai, pers. comm.). Our storage rates determined for the two decades of our analysis (3.9 ± 0.5 and 5.4 ± 0.6 Pg C dec^{-1}) agree with the regional estimates in the ranges of their uncertainty, but support the finding of an increasing rather than a constant or moderately decreasing basin wide storage rate. When interpreting the regional inventories in the Atlantic Ocean, it should be noted that the uncertainties provided by Woosley et al. (2016) are bulk uncertainties representing 20% of the absolute values, while those of Gao et al. (2022) are based on the latitudinal variability of column inventory estimates within 10° latitude bins. Neither uncertainty range is directly comparable to ours.

For the Pacific Ocean, the most recent regional study found that the basin-wide storage of C_{ant} over the top 1500 m accelerated from the first to the second decade of the 1995 to 2015 period (Carter et al., 2019). This increase was detected primarily in the Southern Hemisphere, where the ΔC_{ant} inventory increased from 5.4 ± 0.6 Pg C dec^{-1} (1995–2005) to 7.8 ± 0.6 Pg C dec^{-1} (2005–2015). In contrast, the Northern Hemisphere revealed a rather steady sink strength during these two periods (3.4 ± 0.5 and 4.0 ± 0.5 Pg C dec^{-1}). Within the Southern Hemisphere, the accelerated C_{ant} storage in the recent decade was found primarily on the equatorward side of the Southern Hemisphere Subtropical Gyre. This pattern is consistent with the slightly higher zonal mean content of ΔC_{ant} (around +2 μmol kg^{-1} dec^{-1}) that we find for our second decade (2004–2014) in the upper 1000m between the equator and 30°S (Fig. 3). Likewise, our decadal ΔC_{ant} inventories over the top 3000m in the South (8.6 ± 1.2 and 7.4 ± 1.0 Pg C dec^{-1}) and North Pacific (2.9 ± 0.8 to 3.2 ± 1.8 Pg C dec^{-1}) are similar to those of Carter et al. (2019). However, we do find an insignificant slow-down rather than an acceleration of the C_{ant} storage changes in the South Pacific, due to our higher storage changes during the first decade. This is partly due to our integration across small negative decadal differences in ΔC_{ant} located between 1500–3000m (Fig. 2B), a depth range which was not considered by Carter et al. (2019). In addition, there are notable differences in the observations incorporated in our analysis. In this study, we do not use the P16 cruise from 1991 due to missing TA data, but we do use calculated TA data from the South East Pacific in the 1990s (Fig. 1 and Table S1). The calculated TA data were adjusted by +3 μmol kg^{-1} according to crossover analysis with directly measured TA data. This positive adjustment of TA data from the 1990s sampling period increases our South Pacific ΔC_{ant} inventory for the 1994–2004 decade by about 1 Pg C (Fig. S11). The most important differences, however, is our consideration of TA for the calculation of C*, whereas Carter et al. (2019) derived C* from DIC by accounting for the effect of organic matter production and remineralization through changes in the oxygen content, but neglected TA changes due to the formation or dissolution of calcium carbonate minerals. If we remove TA from our C* calculation as well, this reduces the ΔC_{ant} column inventories (Fig. S11) and leads to an inventory that is about 3 Pg C dec^{-1} lower in the South Pacific for the 1994–2004 decade. However, according to our reassessment of the GLODAP crossover (Fig. S3) we do not have clear indications that this difference might primarily be due to data inconsistencies. We thus conclude that it might capture a real signal in the calcium carbonate cycle.

For the Indian Ocean, no multi-decadal regional studies are available for comparison to our ΔC_{ant} inventories (7.2 ± 0.9 and 5.7 ± 0.6 Pg C). Still, our inventories agree with the expected steady-state storage change (Fig. 5) based on the total C_{ant} inventory determined for the mid-1990s (Sabine et al., 2004, 1999). An intensified C_{ant} storage was previously described

for the decade around 2000, albeit based on a single reoccupied east-west section at around 20° and without deriving a whole basin ΔC_{ant} inventory (Murata et al., 2010). This is in agreement with our elevated reconstructed ΔC_{ant} inventories for our first decade 1994 – 2004.

We conclude from this comparison that the patterns and trends in our ΔC_{ant} reconstructions agree with those determined in regional studies, and that differences can — where they exist — be attributed to differences in the chosen integration depth, differences in the definition of the target variable C*, and sometimes most likely also to the uncertainty associated with the computation of a whole basin inventory from a single reoccupied transect (Woosley et al., 2016; Gao et al., 2022).

References of supplementary material

Bittig, H. C., Steinhoff, T., Claustre, H., Fiedler, B., Williams, N. L., Sauzède, R., Körtzinger, A., and Gattuso, J.-P.: An Alternative to Static Climatologies: Robust Estimation of Open Ocean CO2 Variables and Nutrient Concentrations From T, S, and O2 Data Using Bayesian Neural Networks, Front. Mar. Sci., 5, https://doi.org/10.3389/fmars.2018.00328, 2018.

Carter, B. R., Feely, R. A., Wanninkhof, R., Kouketsu, S., Sonnerup, R. E., Pardo, P. C., Sabine, C. L., Johnson, G. C., Sloyan, B. M., Murata, A., Mecking, S., Tilbrook, B., Speer, K., Talley, L. D., Millero, F. J., Wijffels, S. E., Macdonald, A. M., Gruber, N., and Bullister, J. L.: Pacific Anthropogenic Carbon Between 1991 and 2017, Glob. Biogeochem. Cycles, 2018GB006154, https://doi.org/10.1029/2018GB006154, 2019.

Clement, D. and Gruber, N.: The eMLR(C*) Method to Determine Decadal Changes in the Global Ocean Storage of Anthropogenic CO_2, Glob. Biogeochem. Cycles, 32, 654–679, https://doi.org/10.1002/2017GB005819, 2018.

Dlugokencky, E. and Tans, P.: Trends in atmospheric carbon dioxide, National Oceanic & Atmospheric Administration, Earth System Research Laboratory (NOAA/ESRL), 2019.

Doney, S. C., Lima, I., Feely, R. A., Glover, D. M., Lindsay, K., Mahowald, N., Moore, J. K., and Wanninkhof, R.: Mechanisms governing interannual variability in upper-ocean inorganic carbon system and air–sea CO2 fluxes: Physical climate and atmospheric dust, Deep Sea Res. Part II Top. Stud. Oceanogr., 56, 640–655, https://doi.org/10.1016/j.dsr2.2008.12.006, 2009.

Fong, M. B. and Dickson, A. G.: Insights from GO-SHIP hydrography data into the thermodynamic consistency of CO2 system measurements in seawater, Mar. Chem., 211, 52–63, https://doi.org/10.1016/j.marchem.2019.03.006, 2019.

Gao, H., Cai, W.-J., Jin, M., Dong, C., and Timmerman, A. H. V.: Ocean Ventilation Controls the Contrasting Anthropogenic CO2 Uptake Rates Between the Western and Eastern South Atlantic Ocean Basins, Glob. Biogeochem. Cycles, 36, e2021GB007265, https://doi.org/10.1029/2021GB007265, 2022.

Garcia, H. E., Boyer, T., Baranova, O. K., Locarnini, R., Mishonov, A., Grodsky, A., Paver, C., Weathers, K., Smolyar, I., Reagan, J., Seidov, D., and Zweng, M. M.: World Ocean Atlas 2018: Product Documentation. A. Mishonov, Technical Editor., 2019.

Gregor, L. and Gruber, N.: OceanSODA-ETHZ: a global gridded data set of the surface ocean carbonate system for seasonal to decadal studies of ocean acidification, Earth Syst. Sci. Data, 13, 777–808, https://doi.org/10.5194/essd-13-777-2021, 2021.

Gruber, N., Clement, D., Carter, B. R., Feely, R. A., van Heuven, S., Hoppema, M., Ishii, M., Key, R. M., Kozyr, A., Lauvset, S. K., Lo Monaco, C., Mathis, J. T., Murata, A., Olsen, A., Perez, F. F., Sabine, C. L., Tanhua, T., and Wanninkhof, R.: The oceanic sink for anthropogenic CO2 from 1994 to 2007, Science, 363, 1193–1199, https://doi.org/10.1126/science.aau5153, 2019.

Jackett, D. R. and McDougall, T. J.: A Neutral Density Variable for the World's Oceans, J. Phys. Oceanogr., 27, 27, 1997.

Johnson, K. M., Dickson, A. G., Eischeid, G., Goyet, C., Guenther, P., Key, R. M., Millero, F. J., Purkerson, D., Sabine, C. L., Schottle, R. G., Wallace, D. W. R., Wilke, R. J., and Winn, C. D.: Coulometric total carbon dioxide analysis for marine studies: assessment of the quality of total inorganic carbon measurements made during the US Indian Ocean CO2 Survey 1994–1996, Mar. Chem., 63, 21–37, https://doi.org/10.1016/S0304-4203(98)00048-6, 1998.

Johnson, K. M., Dickson, A. G., Eischeid, G., Goyet, C., Guenther, P. R., Key, R. M., Lee, K., Lewis, E. R., Millero, F. J., Purkerson, D. G., Sabine, C. L., Schottle, R. G., Wallace, D. W. R., Wilke, R. J., and Winn, C. D.: Carbon Dioxide, Hydrographic and Chemical Data Obtained During the Nine R/V Knorr Cruises Comprising the Indian Ocean CO2 Survey (WOCE Sections I8SI9S, I9N, I8NI5E, I3, I5WI4, I7N, I1, I10, and I2, and 12; December 1, I994-January 22, 1996), https://doi.org/10.3334/CDIAC/OTG.NDP080, 2002.

Key, R. M., Kozyr, A., Sabine, C. L., Lee, K., Wanninkhof, R., Bullister, J. L., Feely, R. A., Millero, F. J., Mordy, C., and Peng, T.-H.: A global ocean carbon climatology: Results from Global Data Analysis Project (GLODAP), Glob. Biogeochem. Cycles, 18, https://doi.org/10.1029/2004GB002247, 2004.

Lauvset, S. K., Key, R. M., Olsen, A., van Heuven, S., Velo, A., Lin, X., Schirnick, C., Kozyr, A., Tanhua, T., Hoppema, M., Jutterström, S., Steinfeldt, R., Jeansson, E., Ishii, M., Perez, F. F., Suzuki, T., and Watelet, S.: A new global interior ocean mapped climatology: the 1◦ × 1◦ GLODAP version 2, 16, 2016.

Lauvset, S. K., Lange, N., Tanhua, T., Bittig, H. C., Olsen, A., Kozyr, A., Álvarez, M., Becker, S., Brown, P. J., Carter, B. R., Cotrim da Cunha, L., Feely, R. A., van Heuven, S., Hoppema, M., Ishii, M., Jeansson, E., Jutterström, S., Jones, S. D., Karlsen, M. K., Lo Monaco, C., Michaelis, P., Murata, A., Pérez, F. F., Pfeil, B., Schirnick, C., Steinfeldt, R., Suzuki, T., Tilbrook, B., Velo, A., Wanninkhof, R., Woosley, R. J., and Key, R. M.: An updated version of the global interior ocean biogeochemical data product, GLODAPv2.2021, Earth Syst. Sci. Data, 13, 5565–5589, https://doi.org/10.5194/essd-13-5565-2021, 2021.

Lauvset, S. K., Lange, N., Tanhua, T., Bittig, H. C., Olsen, A., Kozyr, A., Alin, S., Álvarez, M., Azetsu-Scott, K., Barbero, L., Becker, S., Brown, P. J., Carter, B. R., da Cunha, L. C., Feely, R. A., Hoppema, M., Humphreys, M. P., Ishii, M., Jeansson, E., Jiang, L.-Q., Jones, S. D., Lo Monaco, C., Murata, A., Müller, J. D., Pérez, F. F., Pfeil, B., Schirnick, C., Steinfeldt, R., Suzuki, T., Tilbrook, B., Ulfsbo, A., Velo, A., Woosley, R. J., and Key, R. M.: GLODAPv2.2022: the latest version of the global interior ocean biogeochemical data product, Earth Syst. Sci. Data, 14, 5543–5572, https://doi.org/10.5194/essd-14-5543-2022, 2022.

Locarnini, R., Mishonov, A., Baranova, O., Boyer, T., Zweng, M., Garcia, H., Reagan, J., Seidov, D., Weathers, K., Paver, C., Smolyar, I., and Locarnini, R.: World Ocean Atlas 2018, Volume 1: Temperature, 2019.

Millero, F. J., Dickson, A. G., Eischeid, G., Goyet, C., Guenther, P., Johnson, K. M., Key, R. M., Lee, K., Purkerson, D., Sabine, C. L., Schottle, R. G., Wallace, D. W. R., Lewis, E., and Winn, C. D.: Assessment of the quality of the shipboard measurements of total alkalinity on the WOCE Hydrographic Program Indian Ocean CO2 survey cruises 1994–1996, Mar. Chem., 63, 9–20, https://doi.org/10.1016/S0304-4203(98)00043-7, 1998.

Murata, A., Kumamoto, Y., Sasaki, K., Watanabe, S., and Fukasawa, M.: Decadal increases in anthropogenic CO2 along 20°S in the South Indian Ocean, J. Geophys. Res. Oceans, 115, https://doi.org/10.1029/2010JC006250, 2010.

Olsen, A., Key, R. M., van Heuven, S., Lauvset, S. K., Velo, A., Lin, X., Schirnick, C., Kozyr, A., Tanhua, T., Hoppema, M., Jutterström, S., Steinfeldt, R., Jeansson, E., Ishii, M., Pérez, F. F., and Suzuki, T.: The Global Ocean Data Analysis Project version 2 (GLODAPv2) – an internallyconsistent data product for the world ocean, Earth Syst. Sci. Data, 8, 297–323, https://doi.org/10.5194/essd-8-297-2016, 2016.

Poulter, B., Bastos, A., Canadell, J., Ciais, P., Gruber, N., Hauck, J., Jackson, R., Ishii, M., Müller, Jens Daniel, J., Patra, P., and Tian, H.: Inventorying Earth's Land and Ocean Greenhouse Gases, Eos, 103, https://doi.org/10.1029/2022eo179084, 2022.

Sabine, C. L., Key, R. M., Johnson, K. M., Millero, F. J., Poisson, A., Sarmiento, J. L., Wallace, D. W. R., and Winn, C. D.: Anthropogenic CO2 inventory of the Indian Ocean, Glob. Biogeochem. Cycles, 13, 179–198, https://doi.org/10.1029/1998GB900022, 1999.

Sabine, C. L., Feely, R. A., Gruber, N., Key, R. M., Lee, K., Bullister, J. L., Wanninkhof, R., Wong, C. S., Wallace, D. W. R., Tilbrook, B., Millero, F. J., Peng, T.-H., Kozyr, A., Ono, T., and Rios, A. F.: The Oceanic Sink for Anthropogenic CO2, Science, 305, 367–371, https://doi.org/10.1126/science.1097403, 2004.

Tsujino, H., Urakawa, S., Nakano, H., Small, R. J., Kim, W. M., Yeager, S. G., Danabasoglu, G., Suzuki, T., Bamber, J. L., Bentsen, M., Böning, C. W., Bozec, A., Chassignet, E. P., Curchitser, E., Boeira Dias, F., Durack, P. J., Griffies, S. M., Harada, Y., Ilicak, M., Josey, S. A., Kobayashi, C., Kobayashi, S., Komuro, Y., Large, W. G., Le Sommer, J., Marsland, S. J., Masina, S., Scheinert, M.,

Tomita, H., Valdivieso, M., and Yamazaki, D.: JRA-55 based surface dataset for driving ocean–sea-ice models (JRA55-do), Ocean Model., 130, 79–139, https://doi.org/10.1016/j.ocemod.2018.07.002, 2018.

Wanninkhof, R., Doney, S. C., Bullister, J. L., Levine, N. M., Warner, M., and Gruber, N.: Detecting anthropogenic CO2 changes in the interior Atlantic Ocean between 1989 and 2005, J. Geophys. Res. Oceans, 115, https://doi.org/10.1029/2010JC006251, 2010.

Woosley, R. J., Millero, F. J., and Wanninkhof, R.: Rapid anthropogenic changes in CO2 and pH in the Atlantic Ocean: 2003–2014, Glob. Biogeochem. Cycles, 30, 70–90, https://doi.org/10.1002/2015GB005248, 2016.

Zweng, M. M., Reagan, J., Seidov, D., Boyer, T., Locarnini, R., Garcia, H., Mishonov, A., Baranova, O. K., Paver, C., and Smolyar, I.: WORLD OCEAN ATLAS 2018 Volume 2: Salinity, 2019.